UC Riverside
UC Riverside Electronic Theses and Dissertations

Title
Enhancement of Titanium-Based Biomedical Microelectromechanical Systems

Permalink
https://escholarship.org/uc/item/6vc718xb

Author
Woo, Bryan Wai Kee

Publication Date
2019

Copyright Information
This work is made available under the terms of a Creative Commons Attribution License, availalbe at https://creativecommons.org/licenses/by/4.0/

Peer reviewed|Thesis/dissertation

eScholarship.org Powered by the California Digital Library
University of California

UNIVERSITY OF CALIFORNIA
RIVERSIDE

Enhancement of Titanium-Based Biomedical Microelectromechanical Systems

A Dissertation submitted in partial satisfaction
of the requirements for the degree of

Doctor of Philosophy

in

Mechanical Engineering

by

Bryan Wai Kee Woo

March 2019

Dissertation Committee:
Dr. Masaru P. Rao, Chairperson
Dr. Suveen N. Mathaudhu
Dr. Sandeep Kumar

Copyright by
Bryan Wai Kee Woo
2019

The Dissertation of Bryan Wai Kee Woo is approved:

____

____

____

Committee Chairperson

University of California, Riverside

ACKNOWLEDGEMENTS

I would like to thank my advisor, Dr. Masaru Rao, for his continual guidance, encouragement, and insight which has allowed me to make mistakes, learn from them, and become a better researcher. I am grateful for his dedication, leadership, and ambition towards fostering independent thinkers and improving the scientific field.

To the other members of the Biomedical Microdevices Laboratory, both prior and current, thank you for your help and support throughout the years. Your understanding and sympathy aided me in enduring the failures and frustrations associated with research, and your happiness made the breakthroughs much, much sweeter. I would especially like to thank Shannon Gott, Omid Khandan, Ryan Peck, Harish Dixit, Duncan Ashby, Samantha Corber, and Justin Mueller. Despite the power outages, flooding, toxic gas alarms, long drives, crazy work hours, and innumerable days where everything seemed to go wrong, your camaraderie and teamwork on cleanroom trips and in lab were invaluable. I hope that I have positively impacted your lives as much as you have mine.

My research would have taken much longer and not been nearly as successful without the incredibly knowledgeable and friendly staff at UC Santa Barbara’s Nanofabrication Facility, UC Riverside’s Center for Nanoscale Science and Engineering, UC Riverside’s Center for Advanced Microscopy and Microanalysis, and UC Riverside’s Machine shop. In particular, I would really like to thank Don Freeborn, Bill Mitchell, Mark Heiden, Dong Yan, Mathias Rommelfanger, Matthew McCormick, and Steve Rightnar for their patience, advice, and help.

I would also like to take some time to thank our collaborators in Dr. Mathaudhu's, Dr. Balandin's, and Dr. Liu's research groups. I have met many great people through these joint efforts and especially want to acknowledge Adane Geremew, Christian Roach, Heather Salvador, Kendrick Mensink, and Thuy Luu. Although we initially started working together in the name of science, I am glad that I was granted the opportunity to get to know all of you and am happy to call you friends. It was a pleasure meeting and working with you these past several years, and I want you to know that I am thankful for your friendship and support, and wish you all the best in your future endeavors.

Although not directly related to my research, I would also like to thank Paul Talavera, Louis Sandoval, Juana Guerrero, Robert Godoy, and the rest of the staff in the Mechanical Engineering Department office at UC Riverside. They worked tirelessly behind the scenes on the administrative side of things and made my graduate school experience much smoother than it would have been otherwise.

I would like to conclude my acknowledgements by thanking my family, my fiancée and future family, my friends, and my UCR Pokemon Go family. Looking back, I am overwhelmed with gratitude for all the love, support, help, food, and prayers that you sent my way.

As I stand on the cusp between this stage of my life and the next, I want to let all of you know that I am grateful to you for being part of my journey. Thank you.

DEDICATION

I dedicate this work to past, present, and future mankind.

“If I have seen further, it is by standing upon the shoulders of giants.” -Sir Isaac Newton

ABSTRACT OF THE DISSERTATION

Enhancement of Titanium-Based Biomedical
Microelectromechanical Systems

by

Bryan Wai Kee Woo

Doctor of Philosophy, Graduate Program in Mechanical Engineering
University of California, Riverside, March 2019
Dr. Masaru P. Rao, Chairperson

As a large shift in demographic age occurs, there is a growing desire for advancements in biomedical technology. This has helped spur growth in the microelectromechanical systems (MEMS) field which has potential for the realization of devices with increased safety, efficacy, and functionality. Although material selection has largely been limited to silicon, advancements in titanium (Ti) micromachining now provide opportunities for the creation of Ti-based MEMS devices. Motivated by these breakthroughs, we discuss our recent contributions for further advancing the Ti MEMS field through: 1) Optimization of small-scale feature fabrication in titanium, and 2) the integration of high-pressure torsion (HPT) processing and Ti deep reactive ion etching (Ti DRIE) for the realization of fenestrated microneedles with enhanced material properties.

Our research on the optimization of small-scale feature fabrication in titanium was motivated by a desire to help address stent restenosis and thrombosis. A growing body of literature suggests that rapid re-endothelialization of implanted stent devices may

provide a means of addressing these issues. Moreover, recent evidence suggests surface topography may provide a means of modulating cell behavior, thereby facilitating stent re-endothelialization. To optimize our Ti DRIE process, we varied chamber pressure, chlorine flowrate, and oxygen flowrate to determine their effects upon the resulting structures. In doing so, we identified critical parameters for sidewall passivation and successfully created rationally-designed surface patterning features as small as 150 nm which represents a five-fold or greater improvement compared to other processes in literature.

Our second research endeavor regarding the integration of HPT processing and Ti DRIE was motivated by the desire to enhance the material properties of Ti without changing its composition. HPT processing was used to refine the grain size of Ti substrates and x-ray diffraction, indentation testing, and microscopy were used to characterize the changes in microstructure and mechanical properties. Significant improvements were observed, and we successfully utilized Ti DRIE to fabricate fenestrated microneedles out of the enhanced material. Collectively, these results represent significant advancements in the Ti MEMS field and illustrate key steps towards the realization of Ti-based MEMS devices with enhanced functionality and customizable properties.

TABLE OF CONTENTS

COPYRIGHT……………………………………………………………………………..ii

SIGNATURE APPROVAL……………………………………………………………...iii

ACKNOWLEDGEMENTS……………………………………………………………....iv

DEDICATION……………………………………………………………………………vi

ABSTRACT OF THE DISSERTATION……………………………………………..vii

LIST OF FIGURES……………………………………………………………………..xiii

LIST OF TABLES………………………………………………………………………xvi

1 INTRODUCTION…………………………………………………………..…….1

1.1 Origins of Nanotechnology and Microelectromechanical Systems…...………2

1.2 The Rise of Biomedical Microdevices……………………………...……………4

1.3 Scope of this Dissertation…………………………………………………..5

2 CORONARY HEART DISEASE…………………………………………………...6

2.1 Disease Statistics…………………………………………………………………7

2.2 Coronary Heart Disease Treatment………………………………………..10

2.3 Stent Restenosis…………………………………………………………...13

2.4 Stent Thrombosis………………………………………………………………16

2.5 Stent Materials and the Case for Titanium…………………………………..19

2.5.1 316L stainless steel…………………………………………...19

2.5.2 Chromium alloys…………………………………………………...20

2.5.3 Nitinol…………………………………………………………...20

2.5.4 Magnesium-based alloys……………………………………...21

2.5.5 Polymers……………………………………………………………...22

2.5.6 Titanium……………………………………………………………23

3 OPTIMIZATION OF SMALL-SCALE FEATURE FABRICATION IN TITANIUM……………………………………………………………………26

3.1 Introduction……………………………………………………………………..27

3.1.1 Regulating endothelial cell shape and phenotype………………….28

3.1.2 Regulating macrophage cell shape and phenotype………………...31

3.1.3 Fabrication of small-scale features in titanium…………………….33

3.2 Materials and Methods………………………………………………………….37

3.2.1 Si imprint master fabrication…………...…………………………37

3.2.2 Ti gratings fabrication……………………………………………...38

3.2.3 Focused ion beam milling…………………………………………43

3.2.4 Surface profilometry………………………………………………43

3.2.5 Scanning electron microscopy……………………………………..44

3.2.6 ImageJ software analysis…………………………………………..45

3.3 Results……………………………………………………………………………..46

3.3.1 Effects of chamber pressure………………………………………..46

3.3.2 Effects of chlorine flowrate………………………………………..51

3.3.3 Effects of oxygen flowrate…………………………………………56

3.4 Discussion…………………………………………………………………………60

3.4.1 Underlying mechanisms of Ti DRIE………………………………60

3.4.2 Optimization of Ti DRIE for ultrahigh resolution features………..62

3.4.3 Comparison to other Ti DRIE processes…………………………..64

4 AGE RELATED MACULAR DEGENERATION……………………………...66

4.1 Disease Statistics…………………………………………………………..67

4.2 Types of Age-Related Macular Degeneration……………………………….68

4.3 Intravitreal Injections………………………………………………………...73

5 HIGH-PRESSURE TORSION-PROCESSED TITANIUM MICRONEEDLES.75

5.1 Introduction…………………………………………………………………..76

5.1.1 Microneedles……………………………………………………….76

5.1.2 High-pressure torsion processing………………..…………………80

5.2 Materials and Methods……………………………………………………….81

5.2.1 Material preparation………………………………………………..81

5.2.2 High-pressure torsion processing of titanium..…………………….82

5.2.3 Grinding and polishing…………………………………………….84

5.2.4 X-ray diffraction…………………………………………………...86

5.2.5 Indentation Testing………………………………………………...86

5.2.6 Kroll's Etching……………………………………………………..87

5.2.7 Focused ion beam milling………………………………………….88

5.2.8 Transmission electron microscopy………………………………...88

5.2.9 ImageJ software analysis…………………………………………..89

5.2.10 Ti-based fenestrated microneedle fabrication…………………….89

5.2.11 Scanning electron microscopy……………………………………92

5.3 Results………………………………………………………………………..93

5.3.1 Phase identification………………………………………………...93

5.3.2 Vickers hardness……………………………………………………...96

5.3.3 Grain size refinement……………………………………………98

5.3.4 Feasibility testing………………………………………………100

5.4 Discussion…………………………………………………………..103

5.4.1 Underlying mechanisms of high-pressure torsion processing……103

5.4.2 Comparison to other high-pressure torsion processes……………104

5.4.3 Ti DRIE adjustments for high-pressure torsion-processed titanium……………………………………………………...105

6 CONCLUSIONS………………………………………………………….107

6.1 Conclusions……………………………………………………………108

6.1.1 Optimization of small-scale feature fabrication in titanium……...108

6.1.2 High-pressure torsion-processed titanium microneedles…………109

6.2 Recommendations for Future Work………………………………...109

6.2.1 Optimization of small-scale feature fabrication in titanium……...110

6.2.2 High-pressure torsion-processed titanium microneedles…………111

BIBLIOGRAPHY…………………………………………………………………113

APPENDIX……………………………………………………………………..126

Appendix A—Si Imprint Master Fabrication…………………………..126

Appendix B—Ti Surface Grating Fabrication………………………….133

Appendix C—Ti Gratings Characterization……………………………143

Appendix D—Microneedle Fabrication………………………………..149

Appendix E—Supplemental Data………………………………………160

LIST OF FIGURES

Figure 2-1. Infographic depicting the heart disease death rates in the United States of America in adults aged 35 and older from 2014 to 2016, by county……………………...8

Figure 2-2. Infographic depicting the total cost of care per capita for Medicare beneficiaries diagnosed with heart disease in the United States of America in 2015, by county…………………………………………………………………………………...9

Figure 2-3. Image depicting blood flow through A) a normal artery and B) an artery affected by atherosclerosis……………………………………………………………12

Figure 2-4. Angiograms depicting A) in-stent restenosis in the left anterior descending coronary artery and B) the same left anterior descending coronary artery after a second stent was deployed within the initial one…………………………………………...15

Figure 2-5. Angiograms depicting A) arterial narrowing before stent implantation, B) arterial site after stent implantation and C) arterial site blockage, 1 day later, due to stent thrombosis…………………………………………………………………………..18

Figure 3-1. Images depicting endothelial cells cultured on Ti (top) and Si (bottom) patterned (left) and unpatterned (right) substrates………………………………………30

Figure 3-2. Micrograph depicting 200 nm linewidth gratings (400 nm pitch) etched using the TIDE process…………………………………………………………………………36

Figure 3-3. Process flow depicting the major steps involved in the fabrication of the Si imprint master……………………………………………………………………………40

Figure 3-4. Process flow depicting the major steps involved in the fabrication of the Ti gratings……………………………………………………………………………….…...41

Figure 3-5. Diagram that depicts A) the grating width and pitch equal to twice the grating width, and B) the layout of the Ti sample with individual grating sections and blank area for control……………………………………………………………………………...42

Figure 3-6. SEM micrographs of 200 nm linewidth grating cross-sections (top row) and floors of adjacent wide trenches (bottom row) depicting the effects of chamber pressure at a) 0.50; b) 1.00; and c) 1.50 Pa……………………………………………………..49

Figure 3-7. Effects of chamber pressure on a) Ti and SiO_2 mask etch rates within the 200 nm linewidth gratings; b) rms floor roughness in the trenches adjacent to the grating sections; and c) extent of sidewall bowing………………………………………………50

Figure 3-8. SEM micrographs of 200 nm linewidth grating cross-sections (top row) and floors of adjacent wide trenches (bottom row) depicting the effects of chlorine flowrate at a) 20; b) 40; and c) 60 sccm…………………………………………………………...54

Figure 3-9. Effects of chlorine flowrate on a) Ti and SiO_2 mask etch rates within the 200 nm linewidth gratings; b) rms floor roughness in the trenches adjacent to the grating sections; and c) extent of sidewall bowing……………………………………………55

Figure 3-10. SEM micrographs of 200 nm linewidth grating cross-sections (top row) and floors of adjacent wide trenches (bottom row) depicting the effects of oxygen flowrate at a) 2; b) 4; and c) 6 sccm……………………………………………………………….58

Figure 3-11. Effects of oxygen flowrate on a) Ti and SiO_2 mask etch rates within the 200 nm linewidth gratings; b) rms floor roughness in the trenches adjacent to the grating sections; and c) extent of sidewall bowing……………………………………………59

Figure 3-12. SEM micrograph of 150 nm linewidth grating cross-section (300 nm pitch) etched with the ultrahigh resolution Ti DRIE process parameters………………………65

Figure 4-1. Color fundus photograph from an individual with dry AMD………………70

Figure 4-2. Color fundus photograph from a 92-year old patient with AMD and macular geographic atrophy located near the center of the eye, and peripheral retinal degeneration…………………………………………………………………………...71

Figure 4-3. Color fundus photograph of an individual with wet AMD…………………72

Figure 5-1. Diagram of the fenestrated microneedle design which consists of a 50 μm wide, 500 μm long needle shank with a 2 by 2 mm handle……………………………...79

Figure 5-2. Images depicting a) a general diagram of the HPT process; and b) a Ti disc before and after HPT processing……………………………………………………83

Figure 5-3. A diagram depicting the major steps involved with the Ti-based MN fabrication process……………………………………………………………………91

Figure 5-4. Results from x-ray diffraction and Highscore Plus analysis depicting a) normalized x-ray diffraction plots of unprocessed, commercially pure, grade 1 and grade 2 Ti and commercially pure, grade 1 and grade 2 Ti that was processed with HPT at 4 turns and a pressure of 1 GPa; and b) stick diagram standards for the omega, alpha, and beta phases of Ti, respectively…………………………………………………………...95

Figure 5-5. Plot depicting average Vickers hardness measurements from indenter testing on grade 1 and grade 2 unprocessed Ti samples and grade 1 and grade 2 Ti samples processed with HPT using 4 turns and 1 GPa of pressure……………………………….97

Figure 5-6. SEM and TEM micrographs depicting the microstructure of a) unprocessed grade 1 Ti, b) grade 1 Ti processed with HPT using 4 turns and 1 GPa of pressure, c) unprocessed grade 2 Ti, and d) grade 2 Ti processed with HPT using 4 turns and 1 GPa of pressure……………………………………………………………………………………..99

Figure 5-7. SEM micrograph depicting the needle shank of a fenestrated MN that is etched in a commercially pure, grade 1 Ti substrate that was processed with HPT using 4 turns and 1 GPa of pressure……………………………………………………………101

Figure 5-8. SEM micrographs depicting Ti DRIE process development for fabrication of a fenestrated, HPT-processed Ti MN using increased oxygen flowrate to promote sidewall passivation…………………………………………………………………….102

Figure E-1. SEM micrographs of 200 nm linewidth grating cross-sections depicting the effects of chamber pressure at a) 0.75; and b) 1.25 Pa…………………………………160

Figure E-2. SEM micrographs of 200 nm linewidth grating cross-sections depicting the effects of chlorine flowrate at a) 30; and b) 50 sccm…………………………………...161

Figure E-3. SEM micrographs of 200 nm linewidth grating cross-sections depicting the effects of oxygen flowrate at a) 3; and b) 5 sccm………………………………………162

Figure E-4. Plot depicting the Vickers hardness values of all the studied materials......163

LIST OF TABLES

Table 2-1. Mechanical properties of some common stent materials……………………..25

Table 5-1. Different steps and associated setting parameters for polishing Ti discs on the autopolisher tool……………………………………………………………………….85

1 Introduction

1.1 Origins of Nanotechnology and Microelectromechanical Systems

Although several major milestones had been reached prior, Richard Feynman's talk in 1959 entitled, "There's Plenty of Room at the Bottom" is commonly referred to as the initial starting point of nanotechnology and microelectromechanical systems. Modern microelectromechanical systems (MEMS) technology is built upon concepts and infrastructure that were developed in the semiconductor industry with the rise of integrated circuit boards made from silicon (Si). Breakthroughs over the past several decades have brought about rapid advancements in this technology including complex materials and techniques. Although many complex procedures and techniques are now utilized to fabricate MEMS devices, in general there are three broad encompassing fabrication categories: surface micromachining, micromolding, and bulk micromachining (Madou 2002; Bustillo et al. 1998; Papautsky et al. 2014; Lin 2008).

Surface micromachining involves selective deposition and removal of thin film materials, typically on the order of tens of nanometers, through techniques such as sputtering and dry or wet etching. These processes usually incorporate multiple structural and sacrificial layers which allow for the creation of three-dimensional features with complex geometries. However, the use of this multilayering technique also leads to its critical limitations. As each additional layer is added, sacrificial or not, the probability of issues arising from surface mismatch, contamination, adhesion, and residual film stress increases. This ultimately limits surface micromachining in terms of feature height and aspect-ratio.

Micromolding involves the creation of devices and/or features, typically on the nano- or micrometer scale, with stamping or molding techniques. These processes start with the creation of a mold or stamp "master" through surface micromachining or bulk micromachining. Once the "master" has been created, it can be used repeatedly in subsequent fabrication efforts such as polydimethylsiloxane (PDMS) casting or thermal imprint lithography. Micromolding is typically considered a faster and more cost-effective manufacturing method than surface micromachining or bulk micromachining, but the creation of the "master" can be difficult to achieve, and there are limitations regarding the selection of materials that can be cast or imprinted with this method.

Bulk micromachining involves selective patterning and removal of material from a bulk substrate. These processes utilize a protective mask layer consisting of photoresist or a deposited material that is commonly patterned through techniques such as photolithography, imprint lithography, or electron beam lithography. The mask inhibits material removal, which enables pattern transference from the mask layer into the underlying substrate through typical etching techniques. Dry etching usually involves some type of plasma etching such as isotropic reactive ion etching (RIE) or anisotropic deep reactive ion etching (DRIE), while wet etching typically involves a chemically reactive, isotropic etchant. Due to the top-down approach of removing material from a substrate, large feature heights and high-aspect ratios can be realized through bulk micromachining. This technique is commonly combined with surface micromachining or micromolding to realize microdevices that have additional miniaturization or design

functionalities. However, incorporating multiple techniques into a cohesive procedure may require careful planning and significant process development.

1.2 The Rise of Biomedical Microdevices

One of the largest areas of growth with the rise of MEMS has been the biomedical field. As the world population ages and life expectancies rise, the demand for better biomedical microdevices continues to increase. Biomedical MEMS, bioMEMS, biomedical microdevices, or lab-on-a-chip systems, as they are also commonly known, have significant potential for advancing modern healthcare. Miniaturization and the development of new biomedical microdevices offers many positive benefits such as greater sensitivity and detection capabilities, improved precision, faster diagnostics, less invasive procedures, and additional manufacturing scalability which could lower costs and aid in usability, availability, and widespread commercialization (Saliterman 2005).

In order to continue making advancements in the biomedical microdevice field, it is important to review the current state of the art technologies and to gain a good understanding of the bigger picture encompassing both the engineering and biomedical perspectives. This is especially relevant when the final utilization and adoption of biomedical microdevices into clinical and commercial use will be determined by their ability to be used effectively, reliably, and safely.

1.3 Scope of this Dissertation

The work outlined in this dissertation aims to expand human knowledge regarding the titanium MEMS field through optimization of small-scale feature fabrication and enhanced material strength. Chapter 2 of this work describes coronary heart disease and focuses on angioplasty and stenting, including the serious issues of stent restenosis and thrombosis. This provides background information for Chapter 3, which discusses rationally-designed surface patterning and optimization of small-scale feature fabrication in titanium. Chapter 4 details age-related macular degeneration including challenges associated with intravitreal injections. This leads to Chapter 5, which covers fenestrated microneedles and efforts to enhance the material strength of titanium through high-pressure torsion. Finally, Chapter 6 concludes this dissertation and suggests some avenues for further study.

2 CORONARY HEART DISEASE

2.1 Disease Statistics

According to the Centers for Disease Control and Prevention (CDC) and the World Health Organization (WHO), coronary heart disease (CHD) is the leading cause of global mortality (Gillespie et al. 2013; Mackay et al. 2004). In the United States, CHD is responsible for approximately 1 in every 4 deaths each year, with over 1 million annual coronary events and an estimated 630,000 annual mortalities (Benjamin et al. 2018; CDC, NCHS 2016). Globally, it is estimated that the annual death toll due to CHD in developed countries has reached 7.2 million people, and that number is only expected to increase with time (Mackay et al. 2004).

CHD also places a significant economic burden on developed countries. In 1998, it was estimated that CHD cost the United States' health-care system $126.6 billion (Russell et al. 1998). More recently, estimates for medical costs associated with treating CHD were in excess of $188 billion for the 2017 year (American Heart Association 2017; CDC, NCHS 2016). Based upon these metrics, the cost of CHD on the U.S. healthcare system will increase to over $366 billion by 2035 (American Heart Association 2017). Infographics from the CDC depicting the seriousness of CHD in the United States of America can be seen in Figures 2-1 and 2-2 (CDC 2017). CHD has been and will continue to be a significant factor in human mortality rates and fiscal policies. It is therefore important to better understand this disease and continue to research ways to improve treatment options.

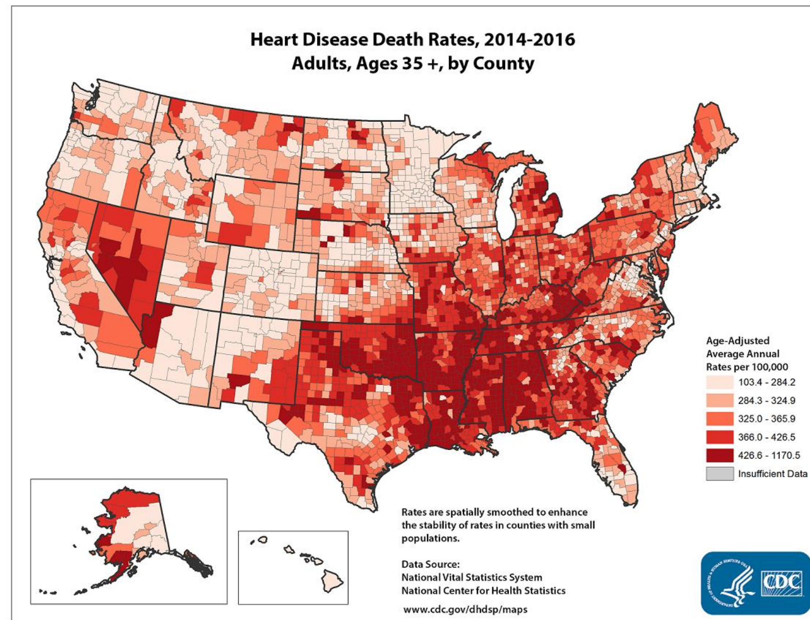

Figure 2-1. Infographic depicting the heart disease death rates in the United States of America in adults aged 35 and older from 2014 to 2016, by county. This map was created using the Interactive Atlas of Heart Disease and Stroke, a website developed by the Centers for Disease Control and Prevention, Division for Heart Disease and Stroke Prevention (CDC 2017).

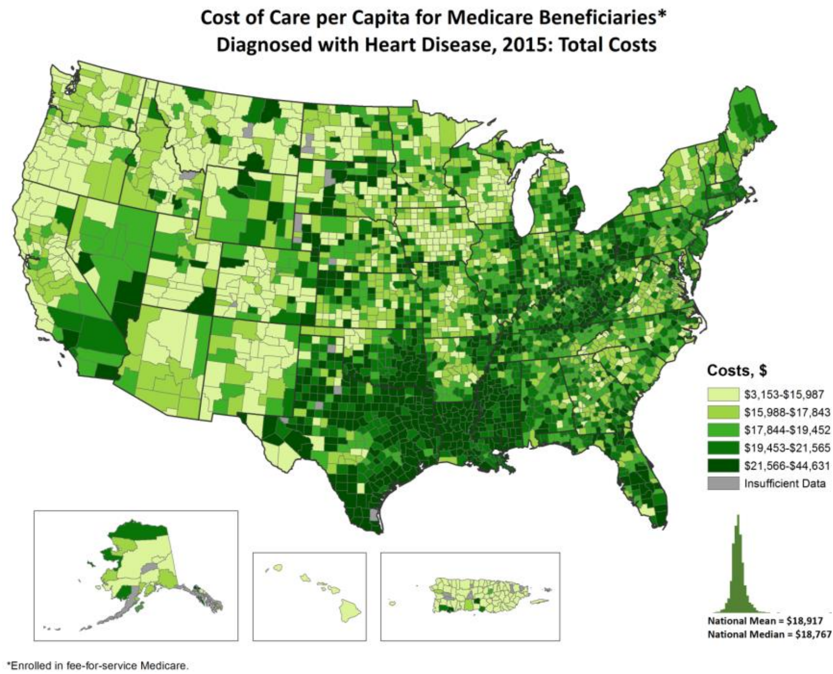

Figure 2-2. Infographic depicting the total cost of care per capita for Medicare beneficiaries diagnosed with heart disease in the United States of America in 2015, by county. This map was created using the Interactive Atlas of Heart Disease and Stroke, a website developed by the Centers for Disease Control and Prevention, Division for Heart Disease and Stroke Prevention (CDC 2017).

2.2 Coronary Heart Disease Treatment

CHD is characterized by an accumulation of low-density lipoprotein (also known as plaque) below the endothelium layer in coronary arteries leading to the heart muscle. As plaque deposits continue to accrue, this creates a condition known as "atherosclerosis," which leads to "stenosis," a restriction and/or blockage of normal blood flow to the heart muscle as the coronary artery becomes narrower. Stenosis can lead to serious consequences including angina, myocardial infarction, and death. Figure 2-3 provides a visual comparison of a normal coronary artery versus one that is affected by atherosclerosis, respectively (NHLBI 2019).

There is currently no cure for coronary heart disease, but the main treatment options include: medication to minimize CHD escalation; coronary artery bypass grafting to form new pathways around atherosclerotic areas; and percutaneous coronary intervention, also known as angioplasty and stenting, to re-open coronary arteries experiencing stenosis.

Angioplasty and stenting has become the current standard therapeutic treatment option for coronary heart disease. During this procedure, a balloon catheter is used to dilate the restricted area, and a stent is deployed to act as a scaffold to help keep the atherosclerotic site open. The two types of stents that are commonly used in these procedures are bare metal stents (BMS) and drug eluting stents (DES). BMS typically consist of a fine metal mesh, and work well as scaffolding for arteries suffering from atherosclerosis. However, BMS have high susceptibility to restenosis due to damage caused to the endothelium layer during the dilation and stent deployment steps and have

some risk of stent thrombosis due to the implanted device (Jaffe et al. 2007; Joner et al. 2006; Holmes et al. 2007; Mohan et al. 2010). Second generation stents, also known as DES, incorporate encapsulated anti-proliferative drugs that inhibit vascular smooth muscle tissue growth. Although the inclusion of these drugs serves to help circumvent the issue of restenosis, DES are susceptible to stent thrombosis, which often has more severe complications (Jaffe et al. 2007; Joner et al. 2006; Holmes et al. 2007; Mohan et al. 2010).

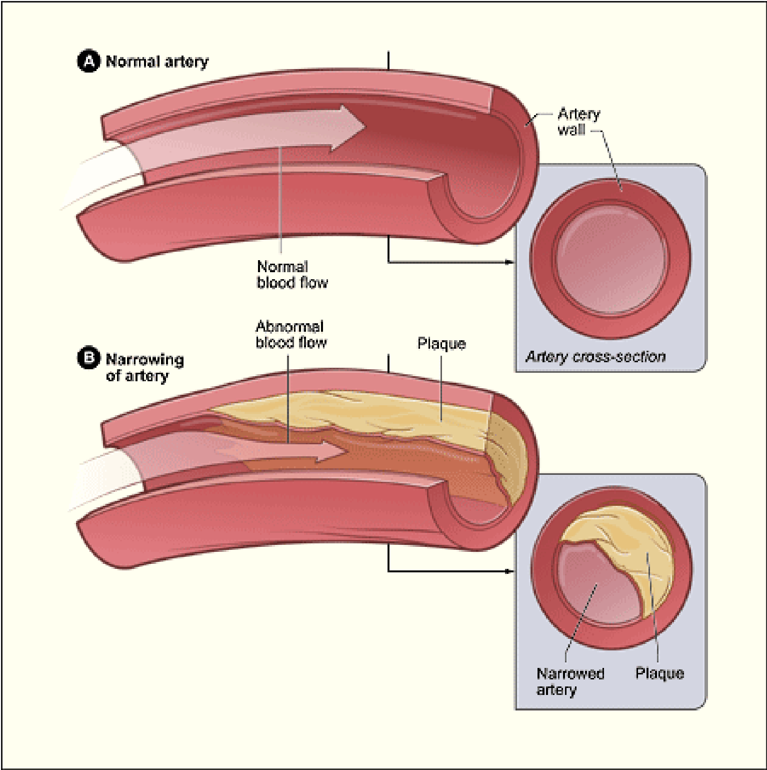

Figure 2-3. Image depicting blood flow through A) a normal artery and B) an artery affected by atherosclerosis. Image taken from the National Heart, Lung, and Blood Institute (NHLBI 2019).

2.3 Stent Restenosis

Restenosis is the recurrence of abnormal narrowing of an artery around a stent device. This restriction or blockage of normal blood flow typically leads to slowly worsening anginal symptoms. Figure 2-4 depicts an arterial site experiencing stent restenosis, and the same site after another stent was successfully deployed within the first one (Yang et al. 2012).

Although it is still not fully understood, many studies have attempted to investigate factors that contribute to stent restenosis (Byrne et al. 2015; Verschuren 2013; Puranik et al. 2013). The most significant factors seem to include neointimal hyperplasia, stent recoil, contact allergy, and stent fracture.

Neointimal hyperplasia is the proliferation and migration of vascular smooth muscle cells in response to damage or trauma caused by balloon catheter expansion and/or stent deployment. Several studies have concluded that neointimal hyperplasia is one of the largest contributors to stent restenosis (Martinez et al. 2011; Sun et al. 2014). Moreover, occurrence rates of neointimal hyperplasia seem be exacerbated in the presence of stents with thicker struts (Pache et al. 2003; O'Brien et al. 2009).

Although thicker stent struts have been linked with restenosis, thinner struts have been linked with stent recoil. Stent recoil occurs when the stent design or mechanical properties of the stent material are insufficient to resist elastic recoil after device deployment. This recoil prevents the stent scaffolding from providing adequate rigidity which allows tissue and plaque to remodel the stent structure. As a result, the stent offers little resistance to further plaque buildup and artery restenosis.

Contact allergy occurs when a patient has hypersensitivity to ions that are exposed in the stent surface or that leach out of the stent material. Ions that have been documented as causing hypersensitivity include nickel, chromate, molybdenum, some types of polymers, and more.

Stent fracture occurs when there is complete or partial separation of the stent device. Studies suggest stent fracture occurs due to mechanical fatigue failure caused by repeated loading and unloading with normal arterial vasomotion, overlapping stents, calcified and tortuous lesions, angulation, and aggressive post-dilatation (Omar et al. 2016). Aside from being a serious potential complication by itself, stent fracture has also been recognized as one of the more common issues associated with DES.

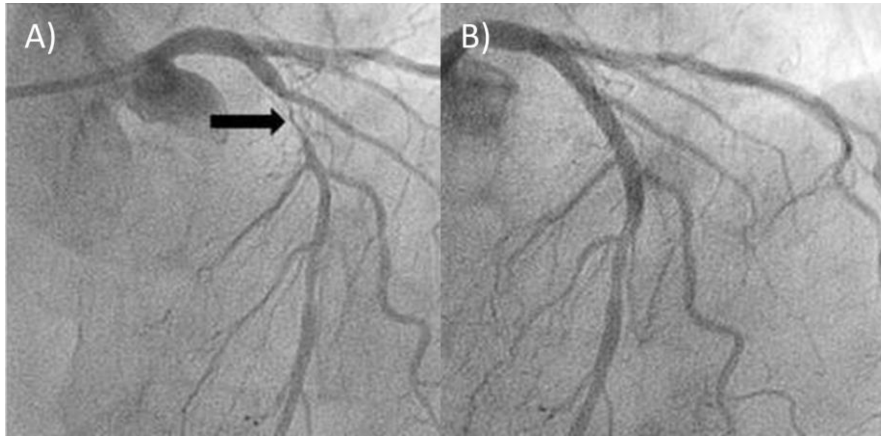

Figure 2-4. Angiograms depicting A) in-stent restenosis in the left anterior descending coronary artery and B) the same left anterior descending coronary artery after a second stent was deployed within the initial one. Image taken from Yonsei Medical Journal (Yang et al. 2012).

2.4 Stent Thrombosis

Stent thrombosis occurs when a blood clot forms inside of a deployed stent device. This clotting creates a restriction or blockage of normal blood flow and typically leads to sudden mortality or large non-fatal myocardial infarction. Figure 2-5 depicts an arterial site that is experiencing stent thrombosis (Gupta et al. 2004).

Despite the severe consequences of stent thrombosis, its underlying causes are still not fully understood. Like restenosis, many research groups have sought to investigate the factors that contribute to stent thrombosis (Collet et al. 2016; Holmes et al. 2007; Nakazawa et al. 2008; Lüscher et al. 2007; Byrne et al. 2015; Mori et al. 2016). The prominent factors identified thus far seem to include stent malapposition, neoatherosclerosis, major stent underexpansion, coronary evaginations, uncovered struts, and neointimal hyperplasia.

Malapposition occurs when there is insufficient wall contact between the stent struts and the arterial wall which leads to stent movement within the artery. As a result, the stent device may not be able to adequately address the arterial scaffolding needs and the stent struts may not undergo proper re-endothelialization, thus remaining exposed targets for fibrin and thrombus.

Neoatherosclerosis occurs when lipid-laden plaque lesions rupture, allowing the plaque to enter the artery and causing plaque and thrombus to accumulate around the stent device.

Major stent underexpansion, as the name implies, occurs when the stent is not fully deployed. This can happen due to a number of reasons such as calcified plaque,

undersized stent for vessel size, insufficient balloon pressure, stent recoil, etc. Stent underexpansion is also significant because it can lead to other restonotic and thrombotic factors such as uncovered struts and malapposition.

Coronary evagination occurs when the artery vessel experiences bulges in the luminal contour as a result of stent deployment. This arterial change can lead to flow disturbances and therefore facilitate accumulation of fibrin and thrombus.

Uncovered stent struts occur when there are delays in re-endothelialization and the uncovered struts remain exposed targets for fibrin and thrombus accumulation.

Neointimal hyperplasia, as previously described, is the proliferation of vascular smooth muscle cells.

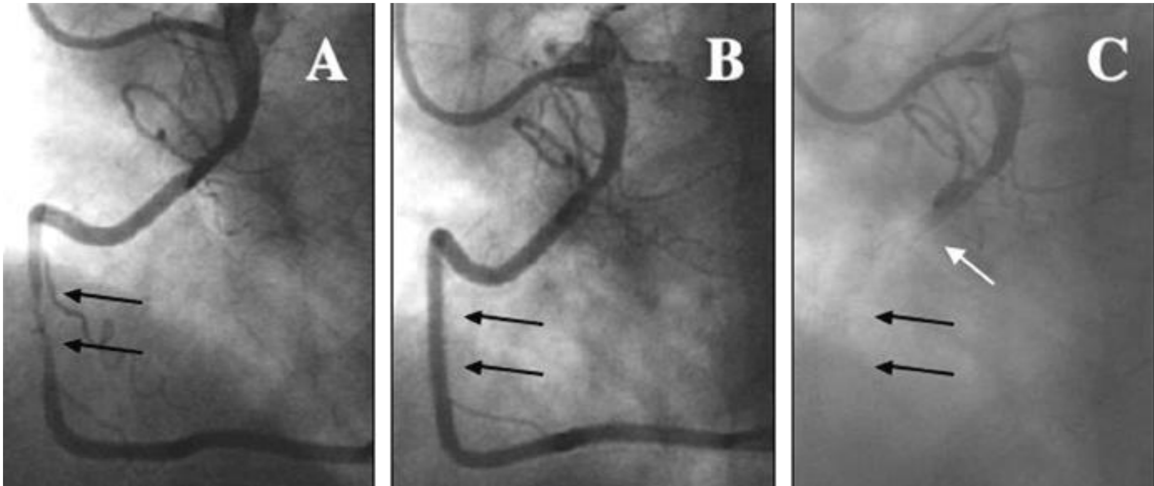

Figure 2-5. Angiograms depicting A) arterial narrowing before stent implantation, B) arterial site after stent implantation and C) arterial site blockage, 1 day later, due to stent thrombosis. Images taken from The Journal of Invasive Cardiology (Gupta et al. 2004).

2.5 Stent Materials and the Case for Titanium

The development of stents involves many complex factors, but biomaterial consideration may be one of the most important. The stent material is very significant due to its influence upon stent design, deployment, and biocompatibility. This section is dedicated to analyzing some common materials used in current stent technology. Table 2-1 depicts a summary of some of the mechanical properties of these materials.

2.5.1 316L stainless steel

Many macroscopic biomedical devices made from 316L stainless steel have a history of being safe, reliable, and relatively low-cost. It is no surprise, then, that 316L stainless steel became the benchmark material for many smaller devices including cardiovascular stents. 316L stainless steel exhibits excellent biocompatibility and adequate mechanical properties (see Table 2-1), but suboptimal corrosion resistance (Poncin et al. 2003). Stents made from stainless steel also have low density which limits visibility if fluoroscopic materials are used.

One of the largest challenges with the use of 316L stainless steel in stents is the issue of corrosion (Gotman 1997). 316L stainless steel contains nickel, chromium, and molybdenum which can leach out of the material as the stent corrodes. These ions are known to potentially trigger adverse immune and inflammatory responses and can lead to serious health conditions such as restenosis. Coatings and changes in material composition are promising ways to minimize occurrences of the aforementioned issues, but additional testing and development is necessary.

2.5.2 Chromium alloys

Chromium alloys including cobalt-chromium (Co-Cr) and platinum-chromium (Pt-Cr) are replacing 316L stainless steel as the mainstream material for current stents. Co-Cr and Pt-Cr alloys have many properties that support this transition including higher material strength, higher density, higher elasticity, good corrosion resistance, and good biocompatibility (Jorge et al. 2015). As a result, Co-Cr and Pt-Cr stents have better maneuverability for navigating difficult artery tortuosity, better radiopacity for increased imaging accuracy, and can be made with better strut dimensions for decreasing the risk of restenosis. Pt-Cr has the same advantages at Co-Cr and has slightly higher density, which results in better radiopacity during imaging (Jorge et al. 2015). However, this improvement comes at a steep cost since platinum is significantly more expensive than cobalt.

Despite these advantages, Co-Cr and Pt-Cr stents perform worse than 316L stainless steel stents with regards to stent recoil. Several studies have concluded that Co-Cr and Pt-Cr stents undergo more stent recoil than others, with some reported percentages in excess of 15% (Abhyankar et al. 2012; Ota et al. 2014). This is a serious drawback as stent recoil is one of the contributing factors to restenosis and can lead to factors that contribute to stent thrombosis such as stent underexpansion and malapposition.

2.5.3 Nitinol

Nitinol is a nickel titanium alloy known for its super elasticity which gives it many potential advantages over other materials regarding stent devices. Nitinol stents

have shape memory and can be self-expanding, therefore potentially minimizing the risk of under- or overexpansion of the device (Mcgrath et al. 2014). Moreover, the super elasticity of the material provides Nitinol stents with the ability to vary their expansion capacity which helps them to adapt to non-uniform artery diameters and enables them to better deal with vasomotion. Finally, the inclusion of titanium provides Nitinol with good corrosion resistance and biocompatibility.

Despite these advantages, Nitinol still suffers from several limitations. Nitinol contains nickel which is known to cause hypersensitivity issues, and there are reported loading or crimping issues during packaging that can cause issues with stent buckling, loss of mechanical stability, malapposition, and coronary evagination (Nagaraja et al. 2018). One other significant drawback of Nitinol stents is poor radiopacity. Heavy corrosion has been reported with some typical marker materials, and their inclusion could lead to accelerated leaching of nickel and deteriorating device properties (Stoeckel et al. 2003).

2.5.4 Magnesium-based alloys

Magnesium-based alloys are an upcoming material that is still being researched for potential use in biomedical microdevice applications such as stents. Creating stents out of magnesium-based alloys could be a major breakthrough due to their potential to be completely bioresorbable (Chen et al. 2014). This could eliminate long-term foreign body host responses in patients while also allowing for full vasomotion restoration without the need for follow-up surgery to recover or remove a stent device. Furthermore, magnesium-

based alloys exhibit excellent biocompatibility, especially since magnesium is already present in the human body, and they have mechanical properties that make them resistant to stent fracture and stent recoil (Mao et al. 2017). As previously mentioned, however, magnesium-based alloys are still being researched, and there are some significant hurdles that still require addressing.

Magnesium-based alloys experience very fast material corrosion which has been known to cause loss of mechanical stability within 2-4 months (Witte 2015; Oppeel 2015). This is sooner than angioplasty and stenting procedures typically need to last, which is ~6 months to 2 years. Finally, as these magnesium-based alloys degrade, they release hydrogen gas which forms localized bubbles and a localized overload of degradation elements. The physiological consequences of these localized bubbles and degradation elements are still unknown and will require additional research to ensure adequate safety.

2.5.5 Polymers

Polymeric stent technology has experienced rapid advancement in recent years. Polymeric stents, like magnesium-based alloyed stents, can be fully resorbable which could potentially eliminate long term foreign body host responses and fully restore vasomotion (Ang, Huang, et al. 2017). Due to the base polymer material, polymeric stents can load more encapsulated anti-proliferative drugs and experience slower degradation rates than magnesium-based alloys (Huang et al. 2017). These properties,

combined with the potential for quick, cost-effective manufacturing, helped contribute to the FDA approval and use of commercial polymeric stents.

The initial results from commercial use of these polymeric stents, however, have revealed the need for additional development. Polymeric stents exhibit poor mechanical properties which means that the polymeric stent struts must be significantly thicker, sometimes more than twice as thick as metallic stent struts, to exhibit the same amount of material strength (Ang, Bulluck, et al. 2017). This additional thickness creates an increased risk of stent fracture in non-uniform arteries and makes it more challenging for polymeric stents to navigate artery tortuosity and to deploy. Additional issues associated with polymeric stents include low density which causes poor radiopacity, localized inflammation at the deployment site, and the fact that some polymers are heat sensitive which can cause issues with sterilization (Huang et al. 2017).

2.5.6 Titanium

Titanium is a promising candidate for stents and other biomedical MEMS devices due to its ductility, fatigue resistance, and high fracture toughness which reduces the risk of catastrophic fracture-based failure when compared to other common MEMS materials such as Si (Sidambe 2014). Titanium also has good mechanical properties including high modulus, material strength, and thermal stability which suggest enhanced performance over common polymeric materials including polydimethyldisiloxane and polymethylmethacrylate. Moreover, titanium forms a native oxide layer on its surface which provides excellent biocompatibility and corrosion resistance and makes it more

favorable for harsh environments including *in-vivo* applications than other metallic MEMS materials such as copper, iron, etc. (Oldani et al. 2012). These properties, combined with its relatively low cost, compatibility with common radiography marker materials, and track record of safety and reliability in larger applications, suggest that titanium is an ideal candidate for biomedical MEMS such as stents.

Some drawbacks appear upon closer analyses of titanium's mechanical properties. Titanium has less material strength and stiffness than the benchmark 316L stainless steel material which leads to concerns regarding the safety and efficacy of a titanium-based devices. Titanium could be alloyed with other materials to overcome this shortcoming, but there are reports of hypersensitivity to its common alloying constituents (Oldani et al. 2012). In addition, alloying titanium could significantly hinder microfabrication efforts due to the chemistry involved and the potential for undesirable effects such as redeposition and micromasking. As a result, titanium is ultimately better for biomedical microdevice applications in its pure form, rather than in an alloy, but its suboptimal material strength and stiffness require addressing.

Material	Density (g/cm^3)	Elastic Modulus (GPa)	Yield Strength (MPa)	UTS (MPa)
316L Stainless Steel	7.95	193	340	~670
L605 Cobalt-Chromium	9.1	243	380-780	820-1200
33Pt Platinum-Chromium	9.9	203	480	834
Martensitic Nitinol	6.45	40	200-300	1200
Superelastic Nitinol	6.45	90		1400
Mg-3Al-1Z Magnesium	1.8	45	162	225
AZ31 Magnesium	1.77	44.8		260
PLLA Polymer	1.4	3.6		65
PLGA Polymer	1.3	4		70
CP Gr 1 Ti	4.5	105	170	240

Table 2-1. Mechanical properties of some common stent materials. Data gathered from (Poncin et al. 2003; Ang, Huang, et al 2017.; Ang, Bulluck, et al. 2017; Chen et al. 2014).

3 OPTIMIZATION OF SMALL-SCALE FEATURE FABRICATION IN TITANIUM

3.1 Introduction

Although the recent surge in implantable biomedical devices has brought about great advancements in the healthcare industry, many devices still suffer from lingering issues and side effects. As previously mentioned, stent technology has experienced significant advancements from the initial stainless steel BMS with the development and inclusion of new drugs, designs, and materials. However, stent restenosis and thrombosis continue to remain lingering challenges to stent efficacy and longevity, and there are still significant concerns associated with dual anti-platelet therapy (Levine 2017). Neointimal hyperplasia has been identified as one of the most significant factors contributing to both stent restenosis and thrombosis but is still not fully understood nor resolved satisfactorily.

Dr. Julio Palmaz has become a famous, yet controversial figure in the field of stenting. He is credited with the creation of the first balloon-expandable stent design upon which many current stents are made, but published results that inconclusively suggested metallic grooves help to promote faster endothelialization (Palmaz et al. 1999). Dr. Palmaz's results have become very controversial due to the significance of his claim. Endothelialization of implantable medical devices such as stents has potential to address neointimal hyperplasia and therefore decrease chances of complications such as stent restenosis and thrombosis. Although controversial, the results from Palmaz et al. inspired numerous follow-up studies that have sought to investigate ways to regulate cell behavior through topographical cues (Biela et al. 2009; Buttiglieri et al. 2003; Choudhary et al. 2006; Bettinger et al. 2008; Padmanabhan et al. 2014).

3.1.1 Regulating endothelial cell shape and phenotype

As reported elsewhere, rational design of surface topography may provide a new means for regulating endothelial cell behavior to facilitate healing, thereby decreasing concerns regarding the safety, efficacy, and longevity of implantable stent devices. Dr. Palmaz's claims regarding faster endothelialization on metallic grooves and positive results from numerous follow-up studies on substrates with surface modifications motivated our laboratory to investigate this discovery utilizing our Ti MEMS platform.

One study carefully created substrate patterning to elongate the cells in the direction of the grooves and therefore mimic the natural morphology of endothelial cells *in-vivo,* which are known to elongate in the direction of blood flow. The results showed an increase in endothelial cell migration and morphology similar to native endothelium on patterned Ti substrates and found a positive correlation between endothelial cell density and decreasing pattern sizes. This was further corroborated by the formation of a confluent endothelial cell layer across an entire Ti substrate that was patterned with smaller feature sizes (Lu et al. 2008).

More recently, our laboratory also published results from an *in-vitro* study investigating endothelial cell density, adhesion, and phenotype as a function of substrate material and grating width. They found improved endothelial cell density, adhesion, and pro-healing phenotype on patterned versus smooth Ti and Si substrates with significantly better response results on the Ti ones (Vandrangi et al. 2013). This can be seen in Figure 3-1 which depicts changes in endothelial cell behavior depending on substrate type (Vandrangi et al. 2013). These results support Dr. Palmaz's claim that endothelial and

smooth muscle cell behavior can be regulated through the presence of rationally-designed surface patterning, and metallic substrates, in this case Ti, elicit a better endothelial cell response.

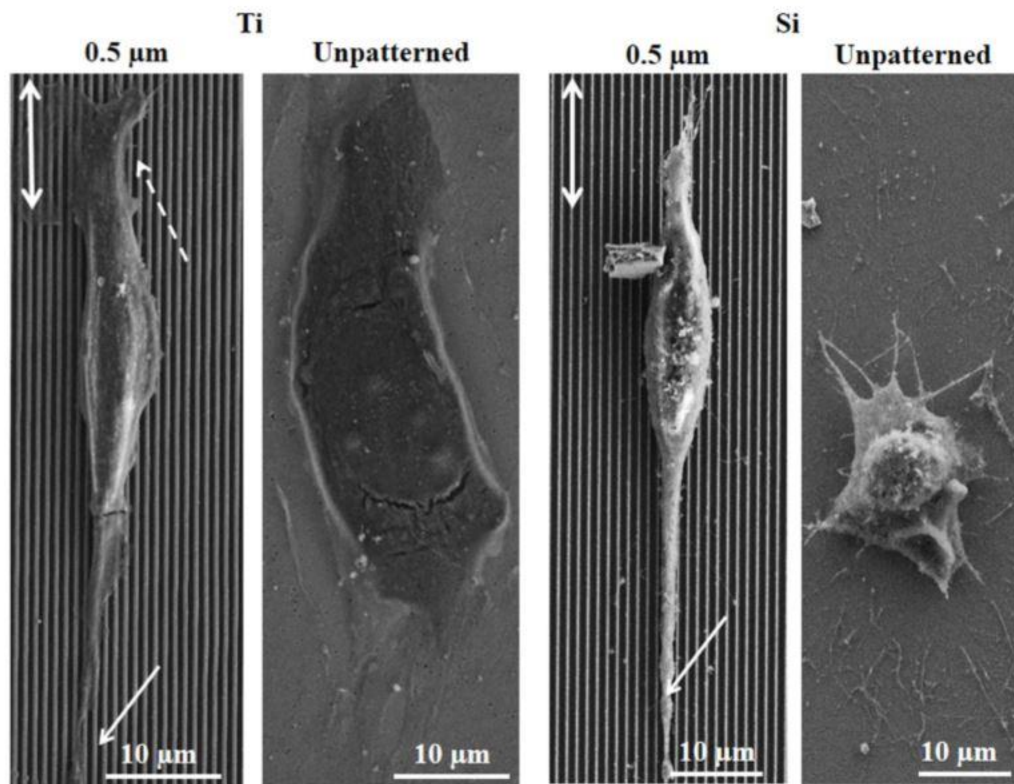

Figure 3-1. Images depicting endothelial cells cultured on Ti- (left) and Si- (right) patterned and unpatterned substrates. Image taken from PLoS ONE (Vandrangi et al. 2014).

3.1.2 Regulating macrophage cell shape and phenotype

Endothelial cells are important for minimizing vascular smooth muscle cell growth, but systemic factors, such as macrophage behavior, should also be considered for a more holistic understanding of the host response to implantable biomedical devices. Macrophages are thought to be a key part of determining how a host body reacts to an implanted biomedical microdevice since they help to regulate immune, inflammatory, and wound healing processes (Anderson et al. 2008). To study macrophage behavior, it is important to recall that macrophages shift towards different phenotypes depending upon their microenvironment. For instance, macrophages that are responding to inflammatory signals such as lipopolysaccharide will secrete pro-inflammatory cytokines such as tumor necrosis factor-α and express inducible nitric oxide synthase. In contrast, macrophages in a wound-healing situation will facilitate tissue repair by producing anti-inflammatory mediators such as interleukin 10 and arginase-1 (Martinez et al. 2014; Wynn et al. 2013). This suggests understanding how a biomaterial regulates macrophage phenotypes is advantageous for selecting and designing biomaterials for implantable devices such as stents.

Recent research results now support the theory that material geometry, or size and shape, may be more influential than biomaterial chemistry for regulating the behavior of infiltrating immune cells (Sridharan et al. 2015; Ma et al. 2014). Evidence suggests that surface roughness and surfaces containing micro-scale features can enhance the adhesion of macrophages and their ability to secrete inflammatory cytokines(Moura et al. 2014; Tan et al. 2006). In one study, macrophages were studied on TiO_2 surfaces of varying

levels of roughness. The results showed positive polarization towards pro-healing phenotype on moderate levels of roughness, but inflammatory activation on surfaces that exhibited greater roughness levels (Ma et al. 2014). In contrast, research investigating macrophage adhesion and behavioral response on electrospun fibers found that that the presence of nanofibers is disadvantageous for macrophage adhesion, inflammatory response, and host response when compared to the presence of micro-scale fibers (Saino et al. 2011; Garg et al. 2013). These results cumulatively suggest surface modifications influence macrophage behavior *in-vitro* and may help to regulate host response *in-vivo*, but there may be size limits to these beneficial features.

Investigating further, it was recently demonstrated that a macrophage's cell shape is involved in regulating the polarization state of its phenotype. In one study, macrophages that were forced to elongate on fibronectin micropatterned lines were found to exhibit an increase in expression of pro-healing markers (Mcwhorter et al. 2013). Additional studies within the stem cell field seem to support this evidence. Several studies have suggested that physical features on the culture substrate regulate differentiation by manipulating changes in adhesion signaling and cytoskeletal organization (Lee et al. 2013; Engler et al. 2006; Yim et al. 2010). Combined, this suggests that macrophage cell shape and adhesion may be influenced by surface topography, which in turn could potentially be used to modulate macrophage behavior.

To advance this knowledge, we investigated the effect of rationally-designed surface patterning on macrophage cell elongation and phenotype polarization. Using our novel titanium deep reactive ion etching technique, we fabricated titanium substrates with

micro- and nano-patterned gratings with varied widths. The micro- and nanopatterned gratings influenced macrophage cell elongation, with peak elongation behavior corresponding to gratings of 400-500 nm widths. Similarly, recorded cytokine secretion levels also appear to peak on Ti gratings of intermediate widths. Finally, culturing macrophage cells on surface patterned substrates did not incite inflammatory activation, but actually appeared to encourage the macrophages towards an anti-inflammatory, pro-healing phenotype (Luu et al. 2015). These positive results suggest that the inclusion of rationally-designed surface gratings can potentially influence macrophage behavior, and thus influence wound healing and the host body's response to implantable device biomaterials.

Despite the success of our macrophage study, recurring masking issues were encountered during the fabrication processes which resulted in a substantial loss of time and resources. Herein, we report our recent efforts to improve Ti DRIE for the reliable and efficient realization of small-scale features. In doing so, we investigate Ti plasma etching parameters and showcase an optimized parameter set with significant potential to improve to our Ti-based MEMS platform.

3.1.3 Fabrication of small-scale features in titanium

The "Bosch Process," originally developed for microfabrication in silicon substrates, is widely regarded as the origin of modern plasma etching. Although the Bosch Process technology and methodology were developed and patented in 1993, more than a decade passed before a Ti equivalent was created and distributed for widespread

use. The paper entitled “High-aspect-ratio bulk micromachining of titanium” by Aimi et al. details the metal anisotropic reactive ion etching with oxidation (MARIO) process which was the first to successfully etch bulk titanium substrates using alternating chlorine etch and oxygen passivation steps (Aimi et al. 2004). During the etch step, chlorine ions adsorb to exposed Ti and form volatile by-products which then desorb from the surface, thereby removing material. During the passivation step, oxygen aids in the formation of a protective passivation layer on the newly etched features which serves to limit further isotropic etching. The MARIO process pioneered deep anisotropic etching of titanium with high-aspect ratio features, but it was limited by relatively slow etch rates (0.5 μm/min) and the isotropic nature of the etch cycle limited the minimum feature size to ~1 μm or greater. Nevertheless, the MARIO process provided the foundation for further development of titanium dry etching.

An improved Ti dry etch process was published by Parker et al. in a paper entitled “Inductively Coupled Plasma Etching of Bulk Titanium for MEMS Applications” (Parker et al. 2005). Instead of a cyclic process, the titanium inductively coupled plasma deep etch (TIDE) process supports a continuous chlorine- and argon-based plasma etch that not only eliminates the sidewall “scalloping” that is characteristic of the MARIO process, but also exhibits improvements in etching. The TIDE process has a higher etch rate (~ 2 μm/min), comparable mask selectivity (~40:1 Ti/TiO_2), and is able to realize smaller minimum feature sizes (~750 nm) in bulk Ti substrates.

Since then, a number of other Ti DRIE processes have been published by others (Zhao et al. 2009; Tillocher et al. 2014), but none have reported reliable minimum feature

sizes below 750 nm. For example, Figure 3-2 illustrates the results from etching 200 nm linewidth gratings with the standard TIDE parameters. The standard TIDE parameters result in an over-aggressive etch which led to severe undercutting and feature loss.

Based upon the results of previous works, we hypothesized that it would be possible to optimize the Ti etching parameters to increase the consistency and reliability of Ti DRIE for small-scale feature fabrication in the deep sub-micrometer scale. To test this hypothesis, we created micro- and nano-patterned Ti substrates using varying chamber pressures, chlorine flowrates, and oxygen flowrates. These parameters were selected as the most relevant for investigation due to our experience with the development of the TIDE process. The subsequent Ti substrates were characterized, and the mask selectivity, undercutting/sidewall bowing, surface roughness, and etch rates were recorded for analysis.

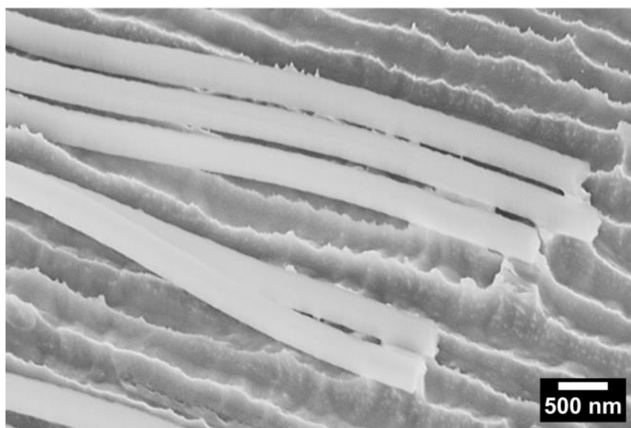

Figure 3-2. Micrograph depicting 200 nm linewidth gratings (400 nm pitch) etched using the TIDE process. Severe undercutting and feature loss are evident which suggests normal TIDE parameters are overly aggressive for defining high-aspect ratio features on the deep submicrometer scale. Image taken from ACS Applied Materials & Interfaces (Woo et al. 2017).

3.2 Materials and Methods

This section is devoted to providing a general overview of the main fabrication and characterization processes associated with our “Ultrahigh Resolution Titanium Deep Reactive Ion Etching” study (Woo et al. 2017). Included in each sub-section is a brief explanation that describes its function and importance within the overall study. Detailed steps for these fabrication and characterization processes can be found in Appendices A through C.

3.2.1 Si imprint master fabrication

A 4” Si wafer was thoroughly cleaned, and a thin anti-reflective coating was spun onto the polished surface. Then, a coating of UV210-0.3 resist was spun onto the anti-reflective layer. Next, the grating pattern was transferred from a quartz mask into the resist layer through exposure using a stepper tool (ASML PAS 5500/300). The resist was then developed with AZ 300 MIF, and the excess anti-reflective coating was subsequently removed by etching with O_2 plasma in a programmable, chlorine-based system (Plasmatherm RIE #5). Next, the grating pattern was etched into the underlying Si substrate using an ICP RIE tool (Plasmatherm 770 SLR), and the residual resist was removed using a 3:1 mixture of sulfuric acid to hydrogen peroxide (Piranha). Finally, each Si “master” was coated with a layer of perflourodecyltricholorsilane (FDTS) in a MVD tool (Applied Microstructures) to aid in the imprinting process. Figure 3-3 depicts the major steps involved with this fabrication process.

The small-scale feature sizes necessary to study topographical cues for regulating cell behavior demanded complex patterning capabilities that are beyond normal photolithography patterning methods. To overcome this barrier, we turned to thermal nanoimprint lithography (TNIL), which enables smaller feature resolution by transferring patterns physically rather than optically. A stepper was used to pattern each imprint master because TNIL requires a master that has patterning on the same scale as the desired features. However, it was not logical to use the stepper to pattern each Ti foil directly due to its sensitivity to sample roughness and planarity and the laborious process involved with stepper sample preparation.

The same Si masters used in our macrophage cell study (Luu et al. 2015) were used in our Ti DRIE optimization grating study because they already incorporated the features and sizes that we wanted to investigate. This not only saved time and resources, but also had the added benefit of proven results.

3.2.2 Ti gratings fabrication

Commercially pure, grade 1 Ti foil with a thickness of 200 μm was thoroughly cleaned, and a 200 nm thick hard mask layer of SiO_2 was deposited onto the surface (Unaxis VLR). Next, MRI 7020 resist was spun onto the SiO_2 layer and TNIL (Nanonex NX2000) was used to pattern it. The grating pattern was then transferred into the SiO_2 hard mask using plasma etching (Panasonic E620-R&D). Following this, the Ti foil was mounted to a Si substrate using double-sided thermally conductive tape, and the individual grating samples were obtained by cutting through the Ti foil/tape/Si substrate

stack with a dicing saw (ADT 7100). Finally, individual grating substrate samples were then mounted to new Si carrier wafers using 5P-Ultra pump oil (Santovac), and the grating pattern was transferred from the hard mask into the underlying Ti substrate (Panasonic E620 R&D). A diagram depicting the major steps in the fabrication procedure can be seen in Figure 3-4.

A baseline recipe was established to reduce the aggressiveness of the etch and provide a standard for comparison. The baseline parameters consist of: 0.5 Pa chamber pressure, 400 W ICP source power, 100 W substrate power, 40 sccm Cl_2, 4 sccm O_2, and 10 °C lower electrode temperature. Additional substrates were etched to test the effects of chamber pressure, chlorine flowrate, and oxygen flowrate. During these tests, one parameter was varied around the baseline value while all other parameters were held constant. The etch time was also held constant at 1 minute to minimize the influence of depth-dependent etching effects such as aspect-ratio dependent etching resulting from transport limitations within deep narrow trenches (Rao et al. 2004).

Each multi-patterned grating substrate contained 15 individual patterned regions and one unpatterned region to serve as a control. The grating pattern width was varied from 150 nm to 50 μm, and the pitch was designed to be equal to twice the grating width. These details can be seen in Figure 3-5.

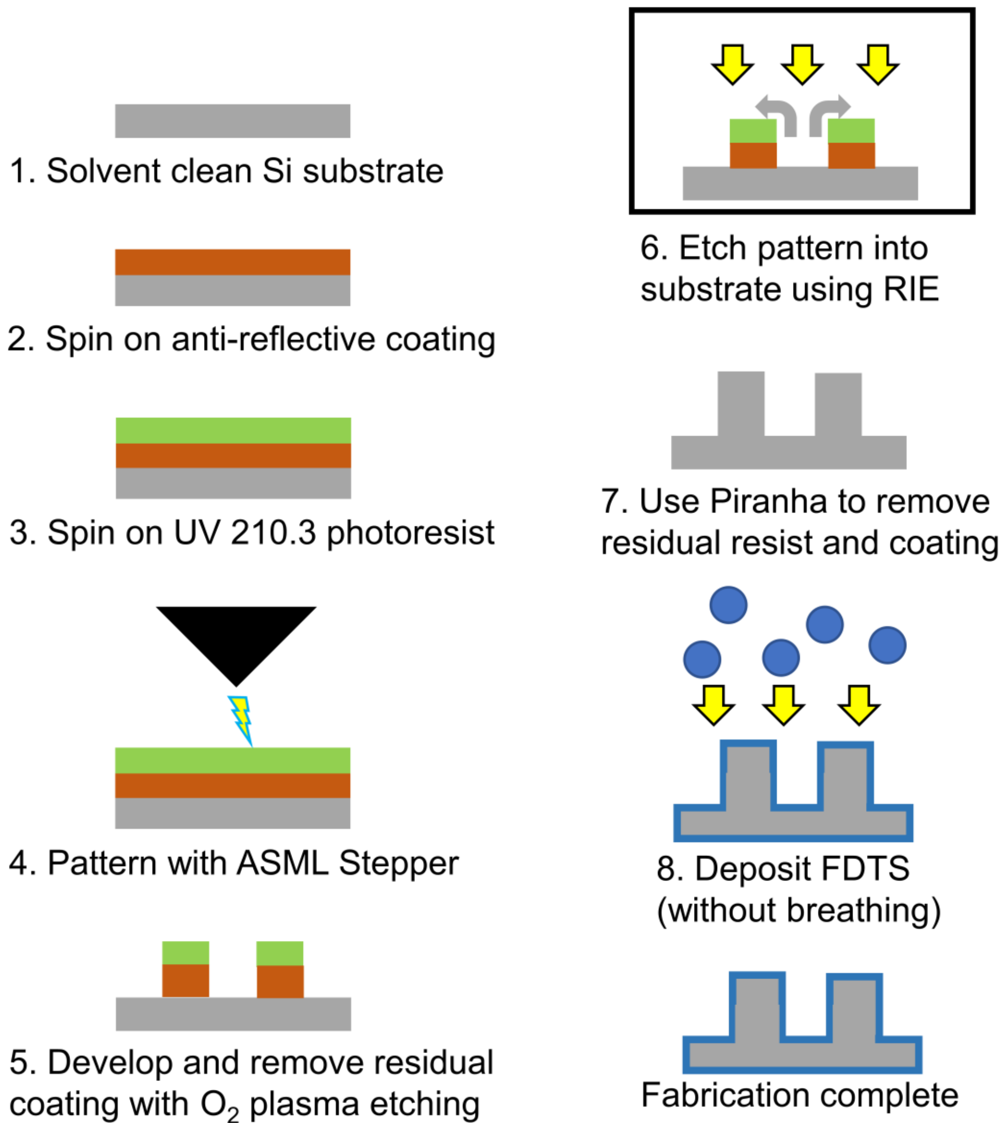

Figure 3-3. Process flow depicting the major steps involved in the fabrication of the Si imprint master. Gray layers represent silicon, burgundy layers represent anti-reflective coating, green layers represent UV 210-0.3 photoresist, and blue represents FDTS.

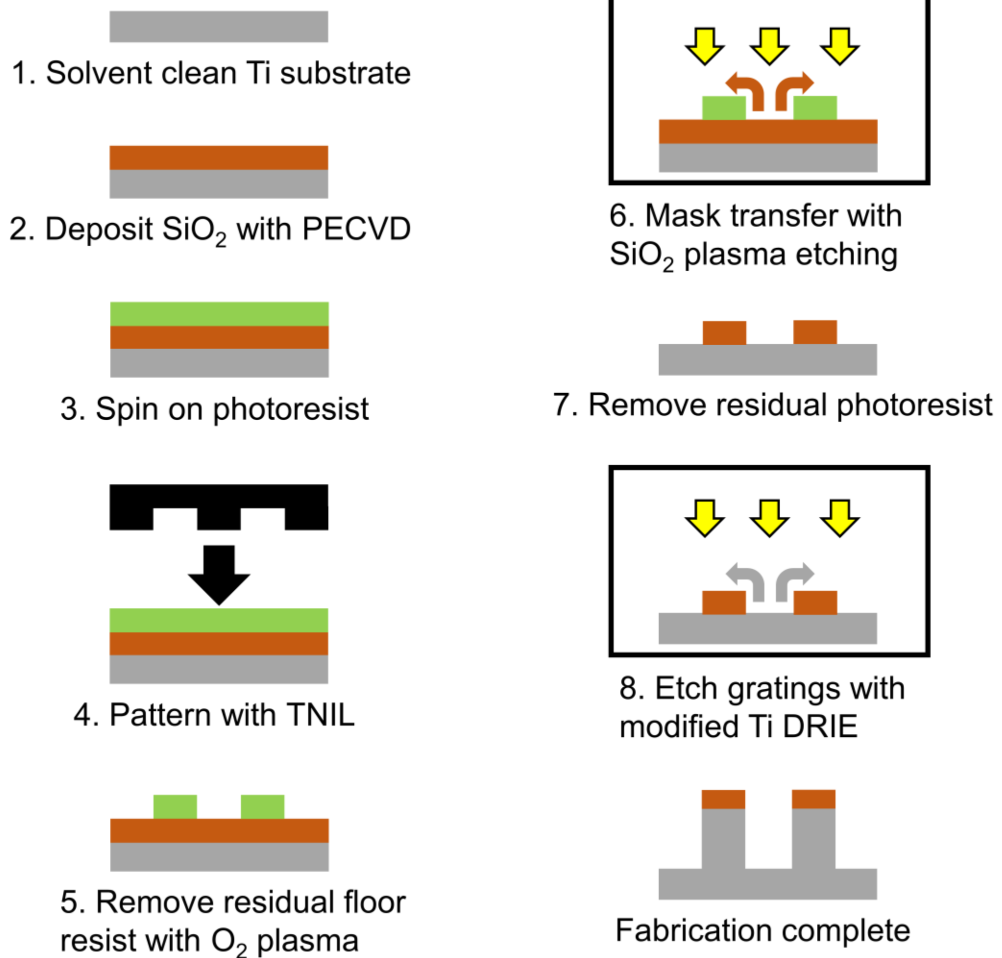

Figure 3-4. Process flow depicting the major steps involved in the fabrication of the Ti gratings. Gray layers represent titanium, burgundy layers represent SiO_2, and green layers represent Az nLoF 2070 photoresist.

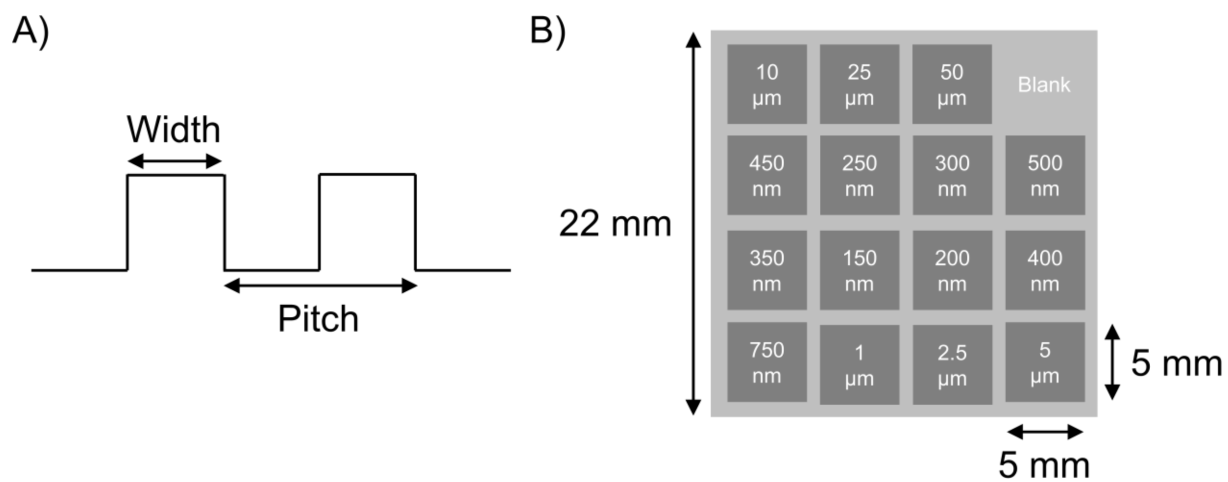

Figure 3-5. Diagram that depicts A) the grating width and pitch equal to twice the grating width, and B) the layout of the Ti sample with individual grating sections and blank area for control. Figure based upon one from ACS Applied Materials & Interfaces (Luu et al. 2015).

3.2.3 Focused ion beam milling

Focused ion beam (FIB) milling was used to remove material to create "windows" that enabled characterization and analysis of the cross-sectional areas. First carbon paint was used to mount a Ti grating sample to a sample stub. The chamber of the FIB tool (Quanta 3D FIB/SEM) was then vented, the sample stub was inserted, and the chamber was pumped down. Once the proper vacuum was reached, the stage was raised to the proper working distance, and the accelerating voltage was increased. The brightness, contrast, wobble, stigmator, focus, and magnification were then adjusted to form an accurate image of the scanned area. Next, stage control was used to navigate the surface, and a suitable site was found within the 200 nm grating section. The stage was then tilted to align perpendicular to the FIB needles, and a small strip of carbon was deposited across the gratings. Once the protective carbon was in place, the carbon source was removed, and the FIB needle was inserted. Material was then removed to create the "window" for examining the cross-section. Multiple passes were used to minimize re-deposition and create a finer finish for analysis. These "windows" into the cross-section areas were later analyzed using scanning electron microscopy (Leo Supra 55) and ImageJ software.

3.2.4 Surface profilometry

Surface profilometry was used to scan etched regions and gather surface roughness data for analysis. First, the backside of a sample's Si mounting chip was cleaned to ensure that the sample laid flat, and then the sample was loaded into the

surface profilometer cabinet (Veeco Dektak 8). The tower and stylus were then lowered to the null position, and the sample positioning was adjusted to ensure that the subsequent scan would properly measure within the etched regions. Thirteen scans were run at various locations on each sample to ensure consistency and accuracy. The scanning parameters consisted of: scan length of 300 μm, scan duration of 10 seconds, 5 mg stylus force, 65 kA measurement range, standard scan type, and a Hills & Valleys Profile. Once each scan was complete, the scan profiles were exported to Microsoft Excel for quantitative characterization and comparison.

3.2.5 Scanning electron microscopy

Scanning electron microscopy (SEM) was used to gather micrographs for visual comparison and quantitative measurements using ImageJ. First a grating sample was secured to the sample stage using the built-in clips. Then the scanning electron microscope (LEO Supra 55) chamber was vented, the sample stage was loaded into the chamber, and the chamber was pumped down. Once the proper vacuum level was reached, the stage was raised, the electron beam was initiated, and the accelerating voltage was increased to 5 kV. The brightness, contrast, wobble, stigmator, focus, and magnification were then adjusted to bring the sample into focus for further navigation. The final parameters for obtaining micrographs were dependent upon what was being imaged.

To obtain images for studying surface roughness, the sample was navigated to the etched areas next to the grating section. The SEM parameters for the surface roughness

micrographs included: 5 kV accelerating voltage, 12.0 mm working distance, 3750 x magnification, line integration scanning, and SE2 detection mode. A relatively low magnification was used to obtain the surface roughness images since the corresponding features were easily recognized at this magnification and a larger survey area was desired to better represent the sample surface.

Gathering images of the grating cross-sections was difficult due to the challenge of finding the FIB "windows" among the grating areas. Once a milled site was found, stage tilt was used to gain a better vantage of the cross-section, and the focus had to be readjusted prior to imaging. The SEM parameters for the cross-sectional area micrographs included: 5 kV accelerating voltage, 12.6 mm working distance, 60000 x magnification, line integration scanning, and inlens detection mode. The same amount of stage tilt was used for each of these micrographs depicting cross-sections in order to ensure that the images and subsequent results were accurate.

3.2.6 ImageJ software analysis

ImageJ software (National Institutes of Health) was used to semi-quantitatively analyze the cross-sectional area micrographs obtained through scanning electron microscopy. The micrographs of the FIB milled "windows" were imported into ImageJ, and the scale was calibrated from each micrograph's scale bar. At least five measurements were taken of the remaining SiO_2 mask thickness, grating etch depth, grating width, and grating spacing for each image. This data was then used to generate plots depicting the relationships between etch rates, mask selectivity, sidewall bowing,

and the selected parameter variation. A five-point scale was used to describe the sidewall bowing with 0 representing no bowing (near vertical sidewalls) and 5 representing bowing sufficient to cause complete undercutting and feature loss. This procedure was followed for each etch parameter variation to better enable analytical comparisons between samples.

3.3 Results

This section is devoted to presenting the results from the “Ultrahigh Resolution Titanium Deep Reactive Ion Etching” study. To better differentiate between the individual parameters that were studied and to help organize the analytical trends, this section has been split into three sub-sections with one devoted to each parameter that was changed.

3.3.1 Effects of chamber pressure

Chamber pressure was varied from 0.50 to 1.50 Pa in 0.25 Pa increments. Figure 3-6 depicts the low-, middle, and high- end of the chamber pressure range (i.e. 0.50, 1.00 and 1.50 Pa, respectively). The SEM micrographs show a significant increase in etch depth as chamber pressure is increased, but this is also associated with increased undercutting which is depicted in the width of the gratings. The gratings etched with 0.50 Pa of chamber pressure are thicker than those etched with 1.00 Pa, and significantly thicker than those etched with 1.50 Pa (a, b, and c, respectively) The etched area

micrographs (those in the second row of Figure 3-6) also suggest a positive trend of increasing roughness within the grains as chamber pressure was increased.

Figure 3-7a quantifies the changes in Ti etch rate with different chamber pressure parameters. The Ti etch rate was observed to increase from 809 nm/min at 0.50 Pa to 1215 nm/min at 1.50 Pa which aligns with the visual assessment of the SEM micrographs in Figure 3-6. Figure 3-7a also quantifies the SiO_2 mask etch rate which was shown to be largely consistent at ~50 nm/min across the chamber pressure range that was studied. This results in an increasing Ti/SiO_2 mask selectivity of 15.2 at 0.50 Pa to 23.3 at 1.50 Pa due to the increasing Ti etch rate.

Figure 3-7b quantifies the average rms surface roughness as a function of chamber pressure using the surface profilometry data of the etched areas near the gratings. A general trend of increasing roughness was found with increasing chamber pressure. Quantitatively, the data shows a range of 14 nm rms surface roughness at 0.50 Pa to 33 nm rms surface roughness at 1.50 Pa. This corroborates the visual assessment of the SEM micrographs in Figure 3-6. Since the surface profilometry data typically included data across multiple grains, the reported rms surface roughness data not only reflected roughness within the grains, but also roughness caused by preferential etching of the grain boundaries. Figure 3-7c depicts the semi-quantitative evaluation of sidewall bowing as a result of variations in chamber pressure. The results suggest that increasing chamber pressure leads to increases in sidewall bowing which corroborates the visual assessment made with the SEM micrographs in Figure 3-6.

The general trends discussed herein regarding the effects of chamber pressure on etch profile largely reflect those reported earlier in the TIDE paper (Parker et al. 2005). Ti etch rates were seen to increase with increasing chamber pressure which may be indicative of increased chemical etching as a result of increased reactive species density and/or scattering. This is further corroborated by the trend of increased sidewall bowing or undercutting with increasing chamber pressure, as noted in both studies, since scattering would be expected to disrupt the anisotropic directionality of the etch. Moreover, as previously mentioned, the mask etch rate in this study was largely consistent across the spectrum of chamber pressure variations. This consistency reinforces the theories about the reactive species density and/or scattering since SiO_2 (used this study) and TiO_2 (used in the TIDE study) are both known to be more dependent upon physical rather than chemical processes and would therefore be less susceptible to changes in chamber pressures. Although the Ti etch rates in this study are lower than those reported earlier, this difference is to be expected since the Cl_2 flowrate used in the baseline condition was decreased to reduce the aggressiveness of the etch. This discrepancy in Ti etch rate may also be attributed to the reduction in feature size since aspect ratio dependent etching effects become more prominent as additional miniaturization is utilized.

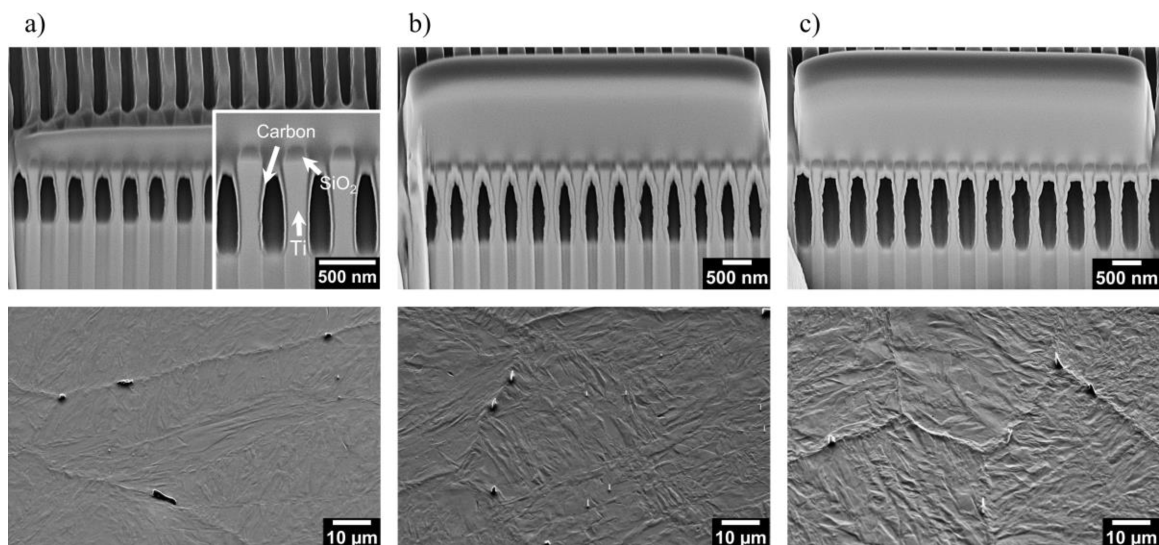

Figure 3-6. SEM micrographs of 200 nm linewidth grating cross-sections (top row) and floors of adjacent wide trenches (bottom row) depicting the effects of chamber pressure at a) 0.50; b) 1.00; and c) 1.50 Pa. All etches were 1 minute, and the remaining Ti DRIE parameters were held constant at the baseline conditions. The bright layer on each grating is a FIB-deposited carbon film that was used to protect against sputtering-induced faceting during the milling process. The inset in a) identifies the different elements in the grating micrographs. The vertical contrast variations beneath the trench floors are "curtain effect" artifacts produced by differential sputtering during FIB milling. Image taken from ACS Applied Materials & Interfaces (Woo et al. 2017).

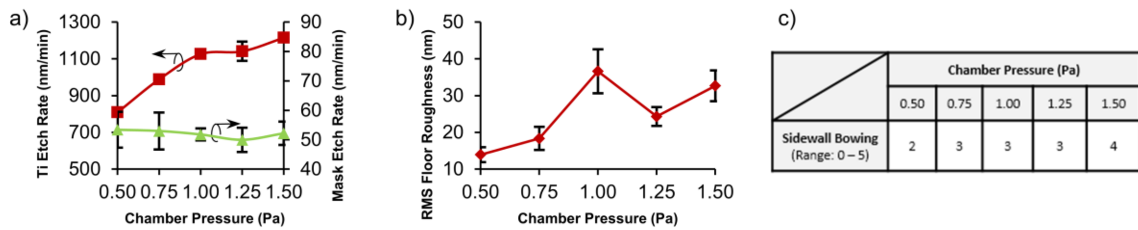

	Chamber Pressure (Pa)				
	0.50	0.75	1.00	1.25	1.50
Sidewall Bowing (Range: 0 – 5)	2	3	3	3	4

Figure 3-7. Effects of chamber pressure on a) Ti and SiO_2 mask etch rates within the 200 nm linewidth gratings; b) rms floor roughness in the trenches adjacent to the grating sections; and c) extent of sidewall bowing. Sidewall bowing was assessed using a semiquantitative score ranging from zero to five, with zero representing no bowing and five representing full undercutting and feature loss due to severe sidewall bowing. Data = mean ± standard deviation ($n \geq 5$). Error bars are not visible in some cases because of the ordinate axis scale. Figure taken from ACS Applied Materials & Interfaces (Woo et al. 2017).

3.3.2 Effects of chlorine flowrate

Chlorine flowrate was varied from 20 to 60 sccm in 10 sccm increments to study how reactive species availability would influence the resulting etch profile. Figure 3-8 depicts the low-, middle, and high- end of the chlorine flowrate range (i.e. 20, 40 and 60 sccm, respectively). These SEM micrographs reveal that chlorine flowrate does influence the etch profile, but to a much lesser degree than changes in chamber pressure. For instance, the Ti etch depths are observed to increase with increasing chlorine flowrate, but the difference is not nearly as significant as was seen in Figure 3-6 with chamber pressure variations. Moreover, the Ti etch depths appear to be plateauing which suggests that the reactive species availability has a limit beyond which no further changes (with regards to Ti etch rate) occur. The etch profiles also suggest that chlorine flowrate has reduced effects on both undercutting and surface roughness when compared to chamber pressure. Slight micromasking was observed at lower chlorine flowrates, but most if not all, was localized at the grain boundaries.

Figure 3-9a quantifies the Ti etch rate within the gratings with respect to chlorine flowrate. The Ti etch rate was 650 nm/min at 20 sccm, 810 nm/min at 40 sccm, and remained relatively unchanged past that point. This supports the visual assessment depicted in Figure 3-8 with reduced Ti etch rates compared to chamber pressure effects and largely consistent etch depths past 40 sccm of Cl_2. In addition to Ti etch rates, Figure 3-9a also displays the effects of chlorine flowrate on SiO_2 mask etch rates. Unlike chamber pressure, the chlorine flowrate seems to be an influential factor in the SiO_2 etch rate with an increase of 50 nm/min at 20 sccm to 67 nm/min at 60 sccm. This trend

creates a Ti:SiO_2 mask selectivity of 12.9 at 20 sccm that increases to 15.2 at 40 sccm and declines to 12.7 at 60 sccm.

Figure 3-9b displays the results of the surface profilometry tests within the etched areas next to the grating sections with regards to chlorine flowrate. The average rms surface roughness was found to be 16 nm at 20 sccm followed by a slight decrease to 15 nm rms surface roughness at 30 sccm and remained consistent with increasing chlorine flowrates. These results support the visual assessment made with Figure 3-8 with the presence of grain boundary micromasking at 20 sccm and its absence with increasing chlorine flowrates. Furthermore, the quantitative data and SEM micrographs support the notion that chlorine flowrate does not affect the average rms surface roughness as much as chamber pressure. Figure 3-9c displays semi-quantitative analysis of chlorine flowrate's influence on sidewall bowing or undercutting. The evaluation suggests that increasing chlorine flowrate leads to minor increases in sidewall undercutting, but chamber pressure is the dominant determining factor.

The results reported herein regarding the effects of chlorine flowrate on the etch profile is largely consistent with previous observations from the TIDE paper (Parker et al. 2005). Both studies show an increase in Ti etch rate with increasing chlorine flowrate which, unsurprisingly, indicates that reactive species density influences the amount of chemical etching that occurs. This is further corroborated by the slight increase in sidewall etching as the chlorine flowrate was increased. However, the mask etch rate trend differs between the two studies. The SiO_2 mask etch rate increased with higher chlorine flowrates while Parker et al. reported little to no change with their TiO_2 mask

etch rates. This discrepancy suggests that the SiO_2 mask used in this study is more susceptible to chlorine than the TiO_2 mask used in the TIDE paper and has further implications regarding mask material(s) which will not be discussed in this work.

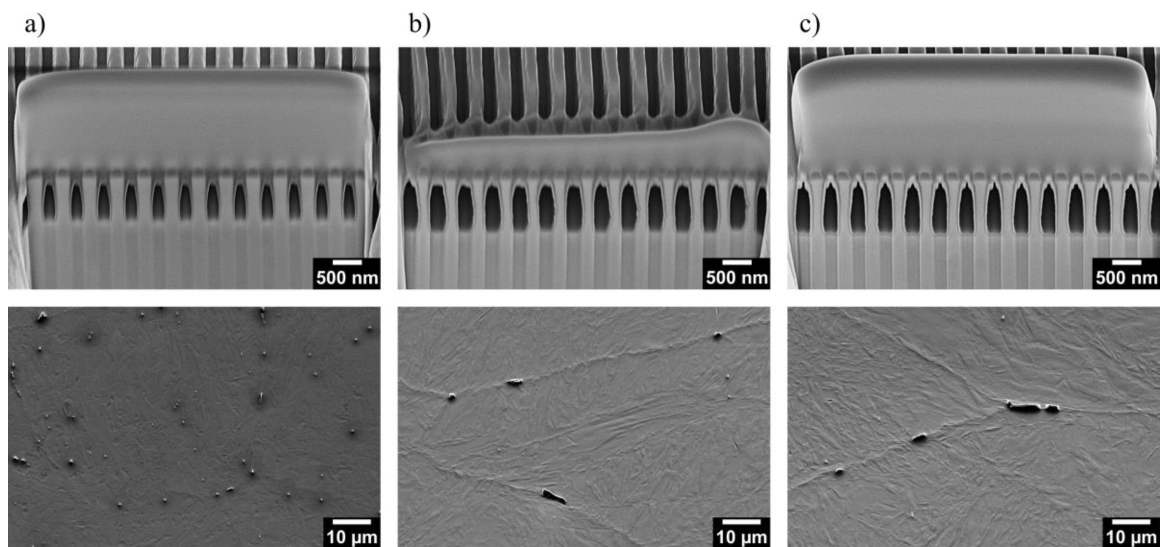

Figure 3-8. SEM micrographs of 200 nm linewidth grating cross-sections (top row) and floors of adjacent wide trenches (bottom row) depicting the effects of chlorine flowrate at a) 20; b) 40; and c) 60 sccm. All etches were 1 minute, and the remaining Ti DRIE parameters were held constant at the baseline conditions. Image taken from ACS Applied Materials & Interfaces (Woo et al. 2017).

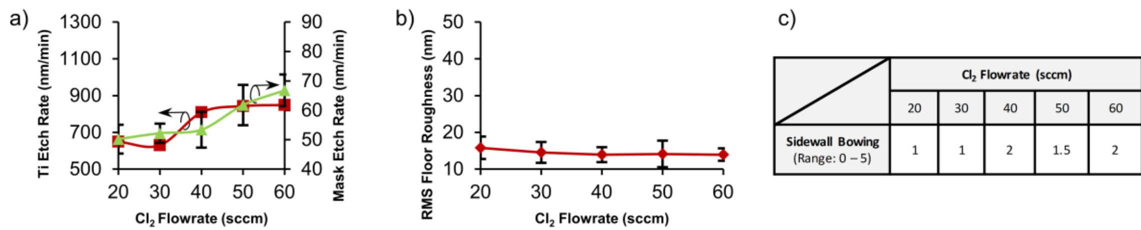

Figure 3-9. Effects of chlorine flowrate on a) Ti and SiO_2 mask etch rates within the 200 nm linewidth gratings; b) rms floor roughness in the trenches adjacent to the grating sections; and c) extent of sidewall bowing. Data = mean ± standard deviation ($n \geq 5$). Error bars are not visible in some cases because of the ordinate axis scale. Figure taken from ACS Applied Materials & Interfaces (Woo et al. 2017).

3.3.3 Effects of oxygen flowrate

Oxygen flowrate was varied from 2 to 6 sccm in 1 sccm increments. Figure 3-10 depicts the low-, middle, and high- end of the oxygen flowrate range (i.e. 2, 4 and 6 sccm, respectively). The SEM micrographs show a positive correlation between increased Ti etch depth within the gratings and increased oxygen flowrate. However, increasing the oxygen flowrate seems to affect the etch profile in the opposite way from increasing chamber pressure or chlorine flowrate. The sidewall bowing or undercutting is observed to decrease as the oxygen flowrate is increased, and the formation of a positive taper at the higher oxygen flowrates was observed. Moreover, the second row of micrographs in Figure 3-10 suggests that increasing oxygen may lead to an increase in surface roughness and additional micromasking, again contrasting with increasing chlorine flowrates.

Figure 3-11a depicts the measured Ti and SiO_2 mask etch rates as a function of oxygen flowrate. The Ti etch rate was 655 nm/min at 2 sccm and then increased to 877 nm/min at 5 sccm before decreasing to 825 nm/min at 6 sccm. This supports the visual assessment made with Figure 3-10 since the grating etch depths are larger in the second column, but slightly less so in the third. The SiO_2 mask etch rate was 83 nm/min at 2 sccm, dropped to 53 nm/min at 4 sccm, and then experienced a slight decline further to 47 nm/min before plateauing at higher oxygen flowrates. This trend is inverse to the chamber pressure and chlorine flowrate behaviors, and leads to Ti:SiO_2 mask selectivity values of 7.9 at 2 sccm, an increase to 18.7 at 5 sccm, and then a slight decrease to 17.6 at 6 sccm.

Figure 3-11b quantifies the surface profilometry data regarding the relationship between surface roughness in the etched areas near the grating sections and oxygen flowrate. The average rms surface roughness was measured to be relatively constant at 14 nm across most of the oxygen flowrates that were studied with a significant jump up to 24 nm rms surface roughness when the oxygen flowrate was increased to 6 sccm. This behavior is largely in line with what is seen in the SEM micrographs since the image corresponding to 6 sccm of oxygen has significantly more micromasking present. Figure 3-11c depicts the results of the semi-quantitative assessment made regarding sidewall bowing or undercutting as a result of varying oxygen flowrates. The results suggest an inverse relationship with increasing oxygen flowrate causing simultaneous decreases in sidewall bowing, and an eventual positive sidewall taper with 6 sccm as previously noted.

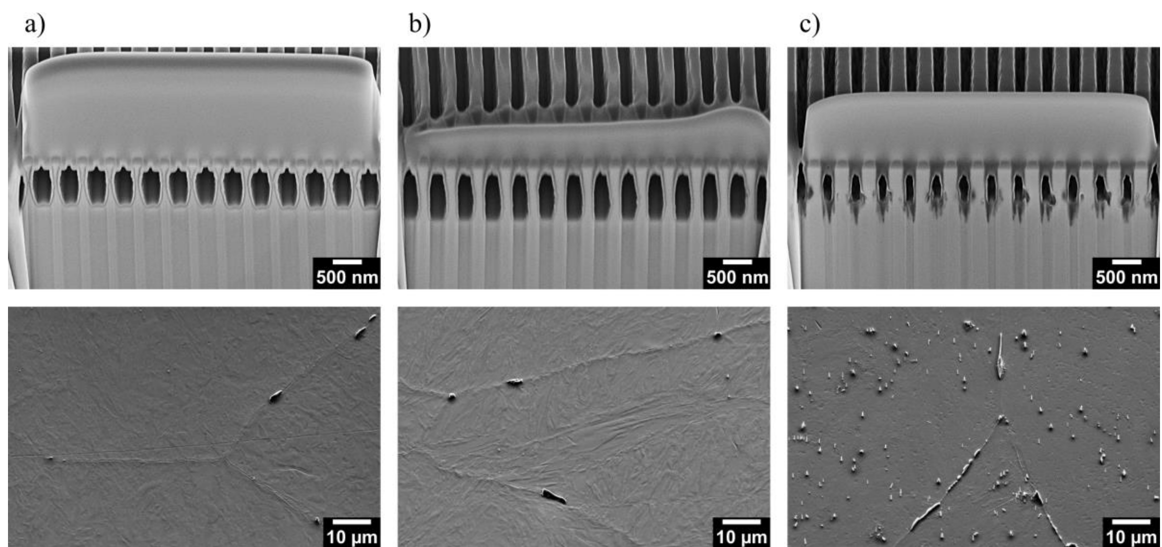

Figure 3-10. SEM micrographs of 200 nm linewidth grating cross-sections (top row) and floors of adjacent wide trenches (bottom row) depicting the effects of oxygen flowrate at a) 2; b) 4; and c) 6 sccm. All etches were 1 minute, and the remaining Ti DRIE parameters were held constant at the baseline conditions. Image taken from ACS Applied Materials & Interfaces (Woo et al. 2017).

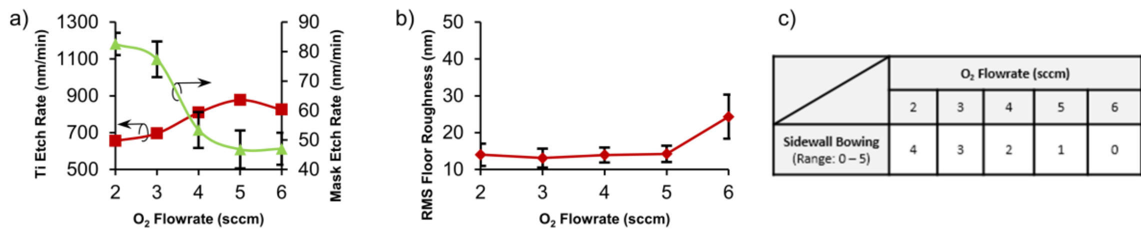

Figure 3-11. Effects of oxygen flowrate on a) Ti and SiO_2 mask etch rates within the 200 nm linewidth gratings; b) rms floor roughness in the trenches adjacent to the grating sections; and c) extent of sidewall bowing. Data = mean ± standard deviation (n ≥ 5). Error bars are not visible in some cases because of the ordinate axis scale. Figure taken from ACS Applied Materials & Interfaces (Woo et al. 2017).

3.4 Discussion

This section is devoted to discussing the results from the "Ultrahigh Resolution Titanium Deep Reactive Ion Etching" study (Woo et al. 2017). It has been split into three subsections which focus on analyzing the underlying mechanisms of Ti DRIE, exploring the observed results to determine what parameter set was optimal for ultrahigh resolution features, and comparing the results of this study to other Ti DRIE processes and results reported by others in literature.

3.4.1 Underlying mechanisms of Ti DRIE

Our understanding of the underlying mechanisms of Ti DRIE are based upon the observations previously reported in the TIDE paper (Parker et al. 2005). It is generally presumed that the molecular Cl_2 undergoes ionization or dissociation into atomic Cl which then adsorb onto exposed Ti, forming volatile byproducts such as $TiCl_4$. Moreover, etch directionality is attributed to the minimization of ion scattering which results in less sidewall bombardment and therefore less lateral etching. Although further investigation into the isotropic etching mechanism is beyond the scope of this study, it is unlikely that the successful realization of the high-aspect ratio features reported herein can be attributed solely to ion directionality. We speculate that an ion-inhibiting DRIE mechanism, similar to previously reported observations from deep etching of Si in F/O_2-based plasmas (Jansen et al. 2009), may be present as well. More specifically, we suspect that lateral etching is minimized by a thin passivating film on the grating sidewalls, while vertical etching is facilitated by preferential ion bombardment of the floors, which may

(a) remove the passivating film or inhibit its formation; (b) enhance chemical etching of the floor by damaging the surface and facilitating reactant species adsorption and dissociation; and/or (c) facilitate the removal of minor reaction products with otherwise limited volatility under the given etch conditions (D'Agostino et al. 1992; Jansen et al. 2009).

Drawing again from observations in literature, we further speculate that the formation of the passivating film could form by any number of means such as (a) oxidation of the exposed Ti; (b) oxidation and re-deposition of non-volatile Ti etch reaction products; and/or (c) erosion or re-deposition of mask material or species derived there-from (Jansen et al. 2009). It is also possible that sidewall passivation may be caused by the deposition and oxidation of reaction products produced by the simultaneous etching of the Si carrier wafer. Evidence for this theory can be found in the study by Tillocher et al. (Tillocher et al. 2014), which showed significant micromasking in Cl_2-based Ti DRIE of chip-scale samples mounted on larger Si carrier wafers. The authors suggested that this may have been caused by the incomplete removal of a SiOCl-based passivation film produced by the oxidation and re-deposition of SiClx reaction products on the sample floors. Although not discussed directly, such mechanisms could be the underlying factors influencing the high anisotropy observed within this study.

Understanding the ion-inhibiting Ti DRIE mechanism may be important for increasing feature aspect ratios and further device miniaturization. Although this warrants further investigation in future studies, the etch profiles and behavior in this study provide preliminary evidence for a basic understanding of the ion-inhibiting DRIE mechanism.

The general trend of increased sidewall bowing with increasing chamber pressure could be explained by removal of the passivating film on the sidewalls due to ion scattering. Similarly, increased sidewall bowing with increasing chlorine flowrates could be a result of greater reactive species density which resulted in greater chemical etching of the passivation layer. Moreover, the smaller amount of sidewall bowing associated with the chlorine flowrate compared to the sidewall bowing with the chamber pressure study indicates that the removal mechanism of the passivation film may be more physical rather than chemical in nature. Finally, the reduction in sidewall bowing and eventual positive sidewall tapering profile with increased oxygen flowrates suggests that oxygen plays a significant role in the formation and thickness of the sidewall passivating film. This is further corroborated by the presence of micromasking in the etched areas near the gratings at higher oxygen flowrates since the ion bombardment on the floors in this study may be unable to fully remove or inhibit formation of the passivating film on the sample floors.

3.4.2 Optimization of Ti DRIE for ultrahigh resolution features

The purpose of this study was to vary chamber pressure, chlorine flowrates, and oxygen flowrates to better understand their effects on Ti DRIE and to subsequently determine the optimal parameter set for ultrahigh resolution features. To this end, the results of the parameter variations were carefully recorded, and the trends were analyzed to maximize etch directionality while maintaining good Ti etch rates and acceptable mask selectivity. Increasing chamber pressure was observed to increase sidewall bowing or

undercutting, so it was minimized to reduce ion scattering and lateral etching of the grating sidewalls. Similarly, increasing chlorine flowrates were observed to increase sidewall bowing or undercutting, so a lower flowrate was selected to reduce reactive species density in an attempt to decrease lateral etching of the sidewalls. Finally, increasing oxygen flowrates were observed to positively influence grating sidewall protection, possibly through the formation of a passivating film, but higher flowrates were also associated with the presence of undesirable micromasking. As a result, the oxygen flowrate value was selected to maximize sidewall protection while preventing the transition to positive tapering profile and micromasking with overpassivation.

Figure 3-12 depicts the application of these optimized parameters toward the fabrication of gratings with deep submicrometer widths of 150 nm. The SEM micrograph depicts surface gratings with high-aspect ratio features (4.0), near vertical sidewalls (~88°), good Ti etch rate (587 nm/min), and an acceptable Ti:SiO_2 mask selectivity (11.1). Furthermore, Figure 3-12 shows that the SiO_2 mask still has sufficient thickness (~150 nm) for additional etching which suggests that there is potential for even greater etch depths with a similar etch profile and higher aspect ratios. The measured average widths and spacings of the Ti gratings were 148 ± 3.5 and 146.5 ± 4.9 nm, respectively. These values are very close to the imprinted resist masks prior to SiO_2 etching which were measured to be 144.8 ± 4.9 and 160 ± 5.1 nm, respectively. The good agreement between these values demonstrates the high-fidelity of the pattern transfer through the ultrahigh resolution Ti DRIE process and suggests even smaller features could be realized with the same process if a patterning method with higher resolution, such as electron

beam lithography, was utilized. It is important to note, however, that the process developed herein would likely need to be further optimized to realize similar etch profiles for other geometries since ion scattering and aspect ratio dependent etch effects can be strongly influenced by feature patterning.

3.4.3 Comparison to other Ti DRIE processes

As previously mentioned, Figure 3-12 shows ultrahigh resolution Ti DRIE can be used to facilitate the realization of features as small as 150 nm with near vertical sidewalls in bulk Ti substrates. This represents a significant resolution improvement over other Ti DRIE processes reported to date, with a fivefold improvement over the TIDE process (Parker et al. 2005), and a sevenfold improvement over the MARIO process (Aimi et al. 2004). Moreover, the 150 nm features also represent a 29-fold or greater minimum feature size resolution improvement when compared to more recent results reported by other Ti DRIE processes (Zhao et al. 2009; Tillocher et al. 2014), although high-resolution feature realization was not the explicit goal of said studies. Another recent effort used Ti reactive ion etching to realize submicrometer features in bulk Ti substrates (Domanski et al. 2012), but significant positive tapering occurred which limited the etch depth and prevented realization of high-aspect ratio features with near vertical sidewalls, which are primary requisites for many devices and applications on this scale.

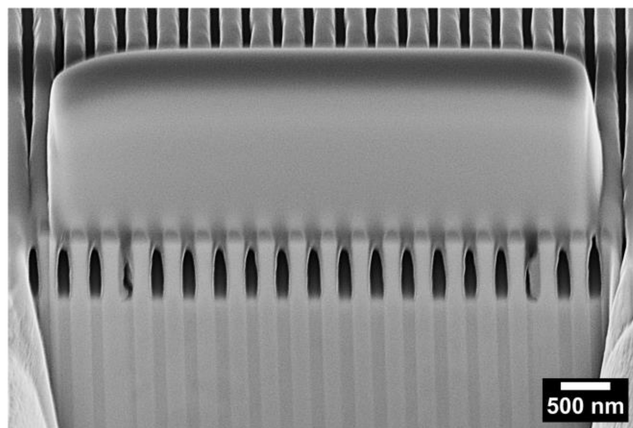

Figure 3-12. SEM micrograph of 150 nm linewidth grating cross-section (300 nm pitch) etched with the ultrahigh resolution Ti DRIE process parameters. The ultrahigh resolution Ti DRIE parameters consist of 0.50 Pa chamber pressure, 400 W source power, 100 W substrate power, 20 sccm chlorine, 4 sccm oxygen, and 10 °C lower electrode temperature. The etch time was 1 minute. Image taken from ACS Applied Materials & Interfaces (Woo et al. 2017).

4 AGE RELATED MACULAR DEGENERATION

4.1 Disease Statistics

According to the CDC and the WHO, age related macular degeneration (AMD) is the leading cause of vision loss in older Americans and the third leading cause of blindness around the world (CDC 2018; WHO 2018). In the United States, it is estimated that approximately 9.2% of Americans who are age 50 and older suffer from some degree of AMD (Mehta 2015). This represents nearly 11 million cases of AMD, and that number is expected to increase to more than 22 million cases by 2050 (Rein et al. 2009). Globally, studies suggest roughly 9% of all incidences of blindness can be attributed to AMD, and estimates believe this is only going to increase (WHO 2018). By the year 2020, over 196 million people are projected to be affected by AMD, and this number is expected to surpass 288 million within two decades (Wong et al. 2014).

As the number of cases of AMD increase, so too does its significant economic burden on healthcare systems. Estimates place direct health care costs associated with AMD in the United States, Canada, and Cuba at approximately $106 billion. It is also estimated that the global cost of visual impairment related to AMD is $343 billion with $255 billion in direct healthcare costs (Gordois et al. 2010). AMD is a budding problem that affects millions of people and costs billions of dollars around the world. It is therefore important to continue researching AMD and pursue better treatment options that can address this growing epidemic.

4.2 Types of Age-Related Macular Degeneration

AMD is known to cause substantial loss of visual acuity due to a slow deterioration of the macula, the central part of the retina within the eye that is responsible for light sensitivity. As the macula deteriorates, the patient's central vision becomes hazier and/or blurrier, which decreases the ability to see fine details. As AMD continues into middle and later stages, the patient's hazy or blurry spot(s) will expand, causing complete loss of central vision. Eventually AMD enters the late and/or final stages in which the haziness and/or blurriness completely fills the patient's field of vision, leading to irreversible blindness.

There are two main forms of AMD: a "dry" form and a "wet" form. The dry form of AMD is the most common, accounting for about eighty percent of all AMD cases. This form of AMD is characterized by a slow accumulation of protein debris called "drusen" between the choroid and the retina. As time passes, these yellowish drusen deposits continue to grow in both size and in number, which contributes to gradually worsening vision as atrophic areas form within the retina. In advanced stages of dry AMD, geographic atrophy occurs which can lead to blind spots, retinal detachment, and complete loss of central vision. Figures 4-1 and 4-2 depict an example of drusen deposits and geographical atrophy within an eye, respectively (Kolb et al. 2018; Soque et al. 2013). There is currently no cure for the dry form of AMD, but in some cases (~10% to 15%) the dry form of AMD leads to the wet form, which is more severe, but can be slowed down with treatment.

The wet form of AMD is more serious than the dry form since vision impairment occurs more rapidly. Wet AMD occurs due to vascular endothelial growth factors (VEGF) which cause choroidal neovascularization. These VEGF cause abnormal blood vessel growth underneath the retina which leads to blood vessel leakage and/or bursting within the macula. Figure 4-3 depicts an example of the wet form of AMD with choroidal neovascularization (Afshari et al. 2012). When this occurs, the excess fluid distorts the patient's vision by making straight lines look wavy and creating blind spots. As wet AMD progresses, the excess fluids within the eye cause the formation of scar tissue (called a disciform scar) and eventually lead to irreversible loss of central vision.

As previously mentioned, there is currently no treatment for the dry form of AMD, and although the wet form of AMD is more severe, several treatment options have been developed and are available that can help to slow, and in some cases reverse, its progression. Typical treatment options for wet AMD include submacular surgery in which invasive surgery is used to remove abnormal blood vessels and fluid from the eyes; laser therapy in which a high-powered laser is used to destroy actively growing abnormal blood vessels; low vision aids in which special lenses and electronic systems create enlarged images of nearby objects; and anti-angiogenesis injections which not only block the growth of new blood vessels beneath the retina by inhibiting VEGF, but also minimize leakage from abnormal blood vessels already present within the eye.

Figure 4-1. Color fundus photograph from an individual with dry AMD. Numerous large drusen deposits are present with the peri- and parafoveal regions. Image taken from Webvision (Kolb et al. 2018).

Figure 4-2. Color fundus photograph from a 92-year old patient with AMD, geographic atrophy located near the center of the eye, and peripheral retinal degeneration. This image was originally published in the Retina Image Bank® website. James B. Soque, CRA OCT-C COA. Pamela A. Weber, MD. ARMD With Geographic Atrophy, Peripheral Degeneration. Retina Image Bank. 2013; Image Number 12356. © the American Society of Retina Specialists (Soque et al. 2013).

Figure 4-3. Color fundus photograph of an individual with wet AMD. Choroidal neovascularization and blood vessel leakage are present. Image taken from Age Related Macular Degeneration - The Recent Advances in Basic Research and Clinical Care (Afshari et al. 2012).

4.3. Intravitreal Injections

The development and implementation of anti-VEGF drug injections has significantly improved treatment of wet AMD and become the standard of care for treating patients suffering from this debilitating condition. Patients have reported full inhibition of AMD progression, and in some cases, recovery of vision that was previously lost due to wet AMD. However, anti-VEGF drugs require intravitreal injections to deliver drugs to the vitreous (i.e. interior of the eye) for posterior segment targeting. Detailed steps for intravitreal injections of anti-VEGF drugs can be found in literature (Wilson et al. 2013; Yorston 2014), but the fundamental steps are outlined here for a basic understanding: The patient lays down, and anesthetic drops are applied to both eyes in order to prepare them for antibiotic povidone iodine eye drops which are known to be very irritating. After the povidone eye drops are administered, a drape is placed over the patient's face and a sterile speculum is used to hold open the patient's eye. A swab containing more anesthetic is inserted into the eye to further numb the injection site and then a measuring device, such as calipers, are used to measure a safe distance behind the limbus for injection. Once the proper distance has been measured, the syringe needle is inserted, and the anti-VEGF drug is injected. After the needle has been removed from the eye, topical antibiotic eye drops are administered, and must be re-administered daily for the following four days.

Despite this relatively well-documented procedure, there are serious risks involved with each intravitreal injection that continue to challenge the safety and efficacy of anti-angiogenesis drug treatments. This is exacerbated by the fact that intravitreal

injection treatment of wet AMD requires multiple injections during monthly follow-up visits. A seven-year study involving a systematic search of intravitreal anti-VEGF injection reports found complications including endophthalmitis, intraocular inflammation, rhegmatogenous retinal detachment, intraocular pressure elevation, and ocular hemorrhaging. Moreover, the study suggests that some anti-VEGF drugs may contribute to systemic effects such as thromboembolic events, myocardial infarction, stroke, hypertension, gastrointestinal perforations, and kidney disease. Finally, rare events have been reported following AMD intravitreal injections including retinal pigment epithelium tears, and several side effects including anterior ischemic optic neuropathy, retinal venous occlusions, retinal artery occlusions, hemorrhagic macular infarctions, development and/or exacerbation of ocular ischemic syndrome, sixth nerve palsy, visual hallucinations, erectile dysfunction, and acute decreases in kidney function have been reported but not investigated or proven to be related (Shima et al. 2008; van Wijngaarden et al. 2005; Falavarjani et al. 2013).

5 HIGH-PRESSURE TORSION-PROCESSED TITANIUM MICRONEEDLES

5.1 Introduction

The majority of issues associated with wet AMD drug delivery appear to be side-effects of the anti-VEGF drugs. The remaining issues including endophthalmitis, intraocular inflammation, retinal detachment, intraocular pressure elevation, and ocular hemorrhaging appear to be linked to infection and/or trauma stemming from the intravitreal injection procedure. Herein, we report our recent efforts to enhance titanium-based fenestrated microneedles for the realization of an ocular drug delivery method that is both safer and more effective than current intravitreal injection techniques. In doing so, we explore high-pressure torsion (HPT) processing and showcase its potential for improving our Ti-based MEMS platform.

5.1.1 Microneedles

Due to their small-scale, microneedles (MNs) offer a promising, minimally-invasive means for ocular drug delivery. MNs allow for proper penetration into, but not through the sclera and/or cornea (Kim, Edelhauser, et al. 2014; Patel et al. 2012; Kim, Grossniklaus, et al. 2014). This allows anti-VEGF drugs that are deposited into these tissues to effectively reach the AMD sites through diffusion while also significantly minimizing tissue trauma and risk of retinal detachment. These advantages are corroborated by documented studies in literature, including one in which solid steel MNs (100 µm in width) were used to penetrate the cornea of a New Zealand white rabbit *in-vivo*. The article reported that the MN penetration caused no inflammatory response, and that the injection site had healed within 3 hours of MN insertion (Jiang et al. 2007).

There are generally two different types of MN designs which are dependent upon their delivery method. MNs with an active delivery method have been realized by pulling glass or steel needles (Jiang et al. 2009; S. R. Patel et al. 2011; S. R. Patel et al. 2012). However, MNs with a passive delivery method may be more advantageous for clinical and commercial use considering their lower complexity, cost, and the disposable nature of MN applications. Much of the research involving passive drug delivery has utilized solid MNs which are typically simpler to fabricate and offer higher structural integrity for penetration. However, solid MNs inherently have low drug-loading capacities, namely whatever stays on as a coating, and much of the drug can be lost during the penetration stage, which further decreases drug availability. Design changes such as fenestrations can be incorporated into solid MN designs to help address these drug loading and drug availability issues.

The Ti-based fenestrated microneedle design used in this study was inspired by work done by Khandan et al. Figure 5-1 depicts the fenestrated MN design. Based upon experimental calculations and other literature sources, it is estimated that these fenestrations can increase the MN drug-loading capacity between two- to ten-fold compared to their solid MN equivalents (Khandan et al. 2016). As a result, fewer needles and/or doses would be required, which has the potential to make Ti-based fenestrated MN ocular injections an intravitreal drug delivery method that is simpler, safer, and more effective.

Despite these benefits, one significant lingering issue remains. As previously mentioned, commercially pure Ti has much lower stiffness and yield strength than other

common biomaterials such as 316L stainless steel. This raises concerns regarding the structural integrity of the Ti-based fenestrated MN during the penetration stage of wet AMD treatment. One potential solution is the utilization of HPT processing.

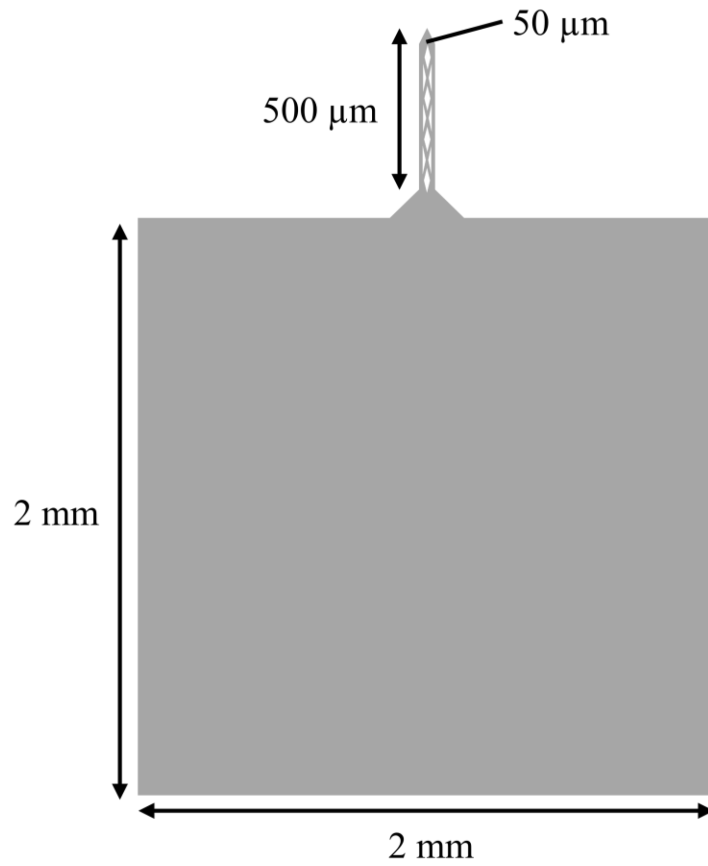

Figure 5-1. Diagram of the fenestrated microneedle design which consists of a 50 μm wide, 500 μm long needle shank with a 2 by 2 mm handle. Design is based upon those reported in Sensors and Actuators, B: Chemical (Khandan et al. 2016).

5.1.2 High-pressure torsion processing

HPT processing refines the grain size of bulk material, which typically leads to significant increases in material strength but a detriment in its ductility. It has conventionally been thought that this tradeoff was unfavorable for applications considering the sample size limitations associated with HPT processing, but the continuing drive for additional device miniaturization circumvents the size limitations, and some biomedical microdevice applications, such as Ti-based microneedles, cardiovascular stents, and intracranial electrodes, may be able to take advantage of the additional material strength and stiffness tradeoff (McCarthy et al. 2011; Khandan et al. 2016; Gott et al. 2015).

We decided to investigate HPT processing of commercially pure Ti and its compatibility with Ti DRIE as a potential means of addressing some of the lingering mechanical property issues associated with devices made from our Ti MEMS platform. Our reasoning for this was twofold. First, HPT processing is one of the most well-known severe plastic deformation techniques, and it is generally accepted that HPT processing consistently results in better grain refinement and more high-angle grain misorientations than other methods such as equal channel angular pressing (Shirooyeh et al. 2014). Secondly, HPT processing is relatively easy to perform, has high repeatability, and its strengthening mechanism does not change the composition of the processed material, unlike other techniques such as solid solution strengthening. This means that HPT processing has a successful track record for effective, reliable results, and Ti processed

with HPT has an increased likelihood of being compatible with our Ti DRIE process in terms of manufacturability.

5.2 Materials and Methods

This section is devoted to providing a general overview of the main HPT, fabrication, and characterization processes associated with our Ti MN study. Included in each sub-section is a brief explanation that describes its function and importance within the overall study. Detailed steps for these fabrication and characterization processes can be found in Appendix D.

5.2.1 Material preparation

A 316L stainless steel plate was purchased from Online Metals and cut into 1”x1” samples on a bandsaw to represent a benchmark material. Meanwhile, commercially pure grade 1 and grade 2 titanium plates were purchased from Fine Metals Corp., and discs with a diameter of 1 cm were obtained through wire electrical discharge machining (wire EDM) on a SODICK SL400Q tool. Brass discharge from the wire EDM process was removed by polishing the samples on a PACE Technologies NANO 1000T tool for ~20 seconds using 400 grit silicon carbide rotating at 120 rpm. Once the brass discharge was removed from the Ti samples, several discs were set aside to serve as Ti controls while the rest were processed with HPT.

5.2.2 High-pressure torsion processing of titanium

HPT processing was performed on a custom-built HPT tool from UFA State Aviation Technical University. Graphite powder was used as a lubricant for the quasi-constrained, tungsten carbide anvils, and the Ti samples were processed with HPT parameters consisting of quasi-constrained conditions at ambient temperature with 1 or 2 GPa of pressure and 2 or 4 rotations at 1 rpm. These parameters were selected in hopes of obtaining a material strength that is comparable to 316L stainless steel, the current benchmark material for many biomedical devices, while avoiding an undesirable alpha to omega phase change which has been reported by others (Sikka et al. 1982; Edalati, et al. 2010). Figure 5-2 depicts a general diagram of the HPT process used in this study and the transformation of a Ti disc.

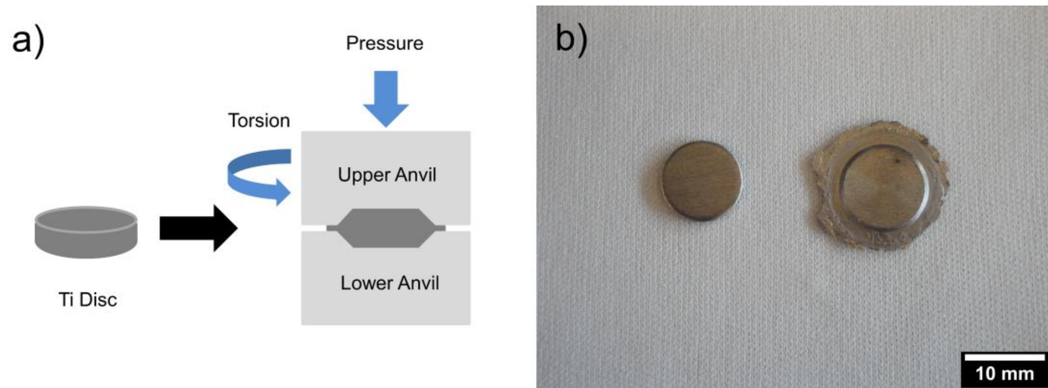

Figure 5-2. Images depicting a) a general diagram of the HPT process; and b) a Ti disc before and after HPT processing. The flanges present on the second disc are caused by material outflow during HPT processing.

5.2.3 Grinding and polishing

The Ti samples that were processed with HPT had a thickness of ~1.2 mm and rough surfaces. In order to accurately characterize the results of the HPT processing, grinding and polishing were utilized to thin the samples and create a fine surface polish. First, the Ti discs were cast in QuickCure acrylic resin (Allied High Tech) and typically allowed to set overnight. Once the encapsulated Ti discs were ready, the samples were polished on an autopolishing tool (PACE Technologies NANO 1000T with FEMTO 1100 Polishing Head) using incrementally finer steps consisting of 400 grit silicon carbide, 6 μm diamond slurry, and 1 μm diamond slurry (see Table 5-1 for the polishing details). Sample surfaces were periodically checked, and polishing was continued until similar sample finishes were obtained. Once complete, the samples were released from the acrylic resin through sonication in acetone, and any remaining acrylic residue was removed with a standard solvent clean consisting of sonication in acetone and isopropyl alcohol followed by thorough rinsing with deionized water.

Step	Description	Grit	Pressure	RPM (h+b)	Pad	Time Increments
1	Planarity Polish	400 SiC	45 psi	200 Complementary	SiC	1- to 2-minutes
2	Preparation	Rinse off samples and prepare for next step				
3	Rough Polish	6 µm diamond	50 psi	60+120 Contra	Texpan	3- to 5-minutes
4	Preparation	Rinse off samples and prepare for next step				
5	Fine Polish	1 µm diamond	50 psi	60+120 Contra	Gold	3- to 5-minutes
6	If doing Step 7	Rinse off samples and prepare for next step				
7	Final Polish (Optional)	200 nm colloidal Silica	45 psi	200 Complementary	Texpan	5- minutes
8	Finishing up	Rinse off samples and clean up				

Table 5-1. Different steps and associated setting parameters for polishing Ti discs on the autopolisher tool.

5.2.4 X-ray diffraction

Phase identification was conducted through peak analysis of X-ray diffraction (XRD) patterns. Samples were cleaned with isopropyl alcohol, dried with nitrogen, and carefully mounted into the sample holder using modeling clay (Sargent Art) and glass slides to minimize sample alignment variations. Next, XRD patterns were obtained using a 30° to 90° scan range encompassing most of the major Ti peaks (PANalytical Empyrean Series 2) with a 70 count/step time. After scanning, the XRD files were converted and exported for phase analysis with Highscore Plus software. Once imported into Highscore Plus, parameters were implemented to identify and reduce background noise, and the software automatically detected the peaks. Alpha Ti (ICSD: 03-065-6231), Beta Ti (ICSD: 03-065-5970), and Omega Ti (ICSD: 00-051-0631) references were used to identify which phases were present.

5.2.5 Indentation testing

Indentation testing (NANOVEA PB1000) was used to obtain Vickers hardness data across the sample surfaces and to test the hardness of the control materials. First, a custom fixture was used to identify and mark the center of each Ti disc. Next, a diamond tipped Vickers hardness indenter was installed into the NANOVEA PB1000 tool, and an indentation program was created. A load of 500 grams and a loading rate of 10 N/min were used to create precise indents in the samples for subsequent analysis. The program created indentations at the center and repeated radially every 1.5 mm from the center towards the edge. A 1.5 mm spacing was used to avoid potential issues caused by

localized cold working, and each indentation set was repeated in triplicate on different substrates to ensure reliability. Indents were evaluated using scanning electron microscopy (see section 5.2.11), and the following relation was used for calculating the Vickers hardness values:

$$H_v = \frac{1.854 * F}{d^2}$$

Where F denotes the indentation load (kgf) and d is equal to the average length of the indent diagonals (mm).

Vickers hardness values in GPa were calculated by multiplying the kgf/mm values by the acceleration due to gravity constant (~9.807 m/s^2) and then dividing by 1000 to convert from MPa to GPa.

5.2.6 Kroll's etching

Kroll's Reagent, a mixture of hydrofluoric acid and nitric acid, was purchased from etchantstore.com to aid in analyzing the microstructure of the unprocessed Ti controls. Since hydrofluoric acid is incompatible with standard beakers, a high-density polyethylene (HDPE) dish and an ethylene tetrafluorothylene (ETFE) dipping basket were used for the wet etching process. Unprocessed grade 1 and grade 2 Ti samples were submerged in Kroll's Reagent for 25 seconds with slow, but constant agitation. Once the 25 seconds elapsed, the samples were immediately removed and thoroughly rinsed in deionized water to stop the etching process. Finally, the samples were dried with a nitrogen gun and carefully stored for subsequent image analysis.

5.2.7 Focused ion beam milling

FIB milling was used to prepare the HPT-processed Ti samples for grain size characterization since Kroll's etching was found to be too aggressive. First, carbon paint was used to mount a Ti disc to a sample stub. The chamber of the FIB tool (Quanta 3D FIB/SEM) was then vented, the sample stub was inserted, and the chamber was pumped down. Once the proper vacuum was reached, the stage was raised to the proper working distance, and the accelerating voltage was increased. The brightness, contrast, wobble, stigmator, focus, and magnification were then adjusted to form an accurate image of the scanned area. Next, stage control was used to navigate the surface, and a suitable site was found near the edge of the sample.

Once an acceptable site was found, the stage was tilted, and the FIB source was inserted. A series of cuts were milled at incrementally increasing tilt angles to thin and prepare a sample for transmission electron microscopy (TEM). Once a sample was prepared and correctly undercut with a "J" shape, it was secured to a TEM manipulator needle and completely undercut. This manipulator needle was then used to transfer the sample to a TEM grid for further analysis.

5.2.8 Transmission electron microscopy

A TEM (FEI Titan 300) was used to collect images from the FIB-processed samples. The TEM grid containing the HPT-processed sample was removed from the SEM chamber, and an optical microscope and tweezers were used to manually load and align it within a TEM sample holder. This TEM sample holder was then installed into the

FEI Titan 300's goniometer, and the operating voltage was set to 300 kV. Next, the gun and filament were turned on, and focusing alignments were made by adjusting the sample height, apertures, spot size, stigmator, wobble, and magnification. Once the sample's microstructure could be clearly seen, the brightness and contrast settings were adjusted, and images were taken for grain size analysis.

5.2.9 ImageJ software analysis

ImageJ software (National Institutes of Health) was used to analyze the SEM and TEM images of the samples' microstructures to calculate the average size of the grains in the HPT-processed Ti samples. Common lineal intercept methodology was utilized for this purpose. First, five lines with random lengths and directions were drawn on each microstructure image. Then each line was followed from one end point to the other, and the number of grain boundary intercepts was counted and recorded. Finally, the average grain size was calculated using the following equation:

$$Average\ grain\ size = \frac{line\ length}{\#\ of\ grain\ boundary\ intercepts}$$

5.2.10 Ti-based fenestrated microneedle fabrication

After all of the preliminary testing was concluded, additional polishing was conducted to refinish the samples' surfaces and prepare them for fabrication. Commercially pure, grade 1 Ti discs (both unprocessed and HPT-processed with 1 GPa of pressure and 4 turns) with a thickness of ~50 µm were standard cleaned by sonicating

in acetone and isopropanol, rinsing with deionized water, and drying with nitrogen. Next, a ~3 μm thick hard mask layer of SiO_2 was deposited onto the surface using PECVD. Once the Ti discs cooled, they were secured to Si substrates using double-sided thermally conductive tape. Following this, a layer of hexamethyldisilazane (HMDS) was spun onto the SiO_2 layer, and a layer of AZ nLoF 2070 photoresist was subsequently spun onto the HMDS. Then the microneedle pattern was transferred into the photoresist using a soda lime mask and a Karl Suss mask aligner (MA-6). Finally, the excess photoresist was removed by developing with AZ 300 MIF developer, thoroughly rinsing with deionized water, and blowing dry with nitrogen.

The Ti disc/tape/Si stack was mounted to a 4-inch Si carrier wafer using 5P-Ultra pump oil and the microneedle pattern was transferred from the photoresist to the hard mask by through-etching the SiO_2 with fluorine-based plasma in an ICP plasma etcher (Oxford Plasmalab System 100). Once this step was complete, the residual oil and photoresist were removed through cleaning with solvents, and the Ti discs were dried with nitrogen. The Ti disc/tape/Si stack was then attached to a 6-inch Si carrier wafer using 5P-Ultra pump oil, and the MNs were realized by through etching the Ti substrate using a chlorine- and oxygen-based plasma (Oxford Plasmalab System 100). Next, the residual oil was removed from the backside by swabbing with acetone, and the MN devices were released from the tape by carefully submerging the Ti/tape/Si stack in acetone which allowed the individual MNs to be retrieved manually with tweezers. A basic diagram depicting the major steps in the fabrication procedure can be seen in Figure 5-3.

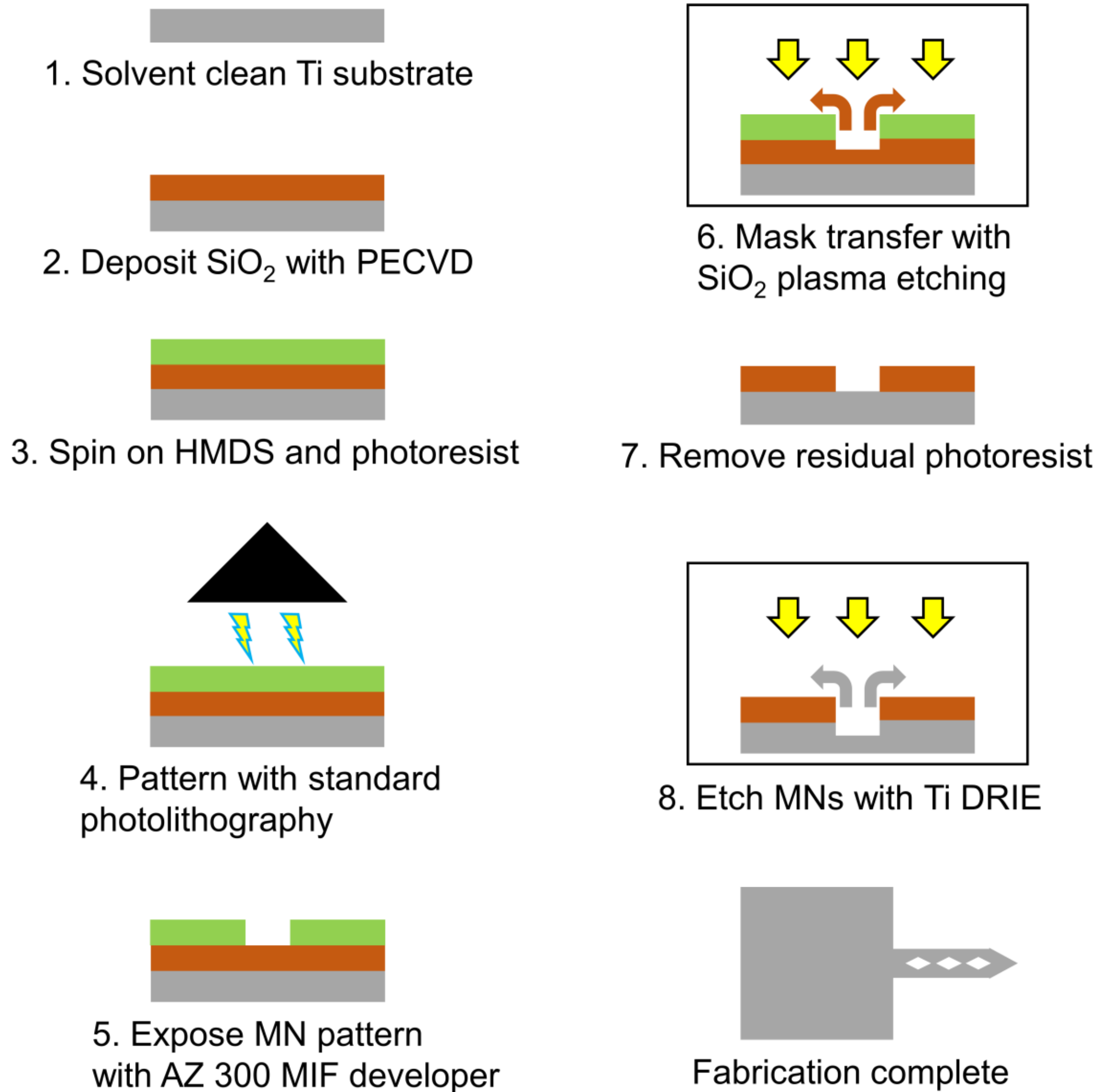

Figure 5-3. A diagram depicting the major steps involved with the Ti-based MN fabrication process. Gray represents the Ti substrate, burgundy represents the SiO_2 hard mask, and green represents Az nLoF 2070 photoresist mask.

5.2.11 Scanning electron microscopy

Scanning electron microscopy was used to gather micrographs for visual comparison and quantitative measurements using ImageJ. First a sample was secured to the sample stage using the built-in clips or carbon tape. Then the scanning electron microscope (LEO Supra 55 or FEI Nova Nano SEM450) chamber was vented, the sample stage was loaded into the chamber, and the chamber was pumped down. Once the proper vacuum level was reached, the stage was raised, the electron beam was initiated, and the accelerating voltage was increased. The brightness, contrast, wobble, stigmator, focus, and magnification were then adjusted to bring the sample into focus for further navigation. The final parameters for obtaining micrographs were dependent upon what was being imaged.

SEM images of the unprocessed, Kroll-etched Ti surfaces were obtained using a FEI Nova Nano SEM450. The SEM parameters for the surface microstructure included: 10 kV accelerating voltage, 5.0 mm working distance, 100x magnification, line integration scanning, Field-free lens mode, and a concentric backscatter detector. A low magnification was used to obtain the microstructure images since the grains were easily recognized at this magnification and a larger survey area was desired to better represent the sample surface.

The SEM micrograph of the MN was obtained using a LEO Supra 55. The MN was secured to the sample stage using carbon tape. The SEM parameters for the surface microstructure included: 5kV accelerating voltage, 8.0 to 12.5 mm working distance, 100x to 2000x magnification, line integration scanning, and SE2 detection mode.

5.3 Results

This section details the results from out HPT-processed MN study. To better organize this data, the gathered information has been split into four subsections, each dedicated to a specific material property that was characterized.

5.3.1 Phase identification

Figure 5-4a depicts the normalized x-ray diffraction patterns obtained from scanning the unprocessed grade 1 and grade 2 Ti control samples and the grade 1 and grade 2 Ti samples processed with HPT using 4 turns and 1 GPa of pressure. Although multiple HPT processing parameter sets were studied, the results included herein exclude all but the ones processed with 4 turns and 1 GPa of pressure since these exhibited the highest hardness values and should thus represent the largest grain refinement. The XRD plots were analyzed, and the diffraction peaks were carefully compared to ICSD standards for alpha, beta, and omega phase Ti using Highscore Plus software. No significant match was found with the omega phase Ti standard, although peak widening was observed which corresponds to texturing and the refined grain size. These results suggest that the HPT processing parameters were sufficient to cause grain refinement within the bulk Ti substrates without triggering an omega phase change.

The absence of omega phase Ti can be visually corroborated by noting the 2Θ peak angles in the XRD plots and comparing them to the stick diagrams in Figure 5-4b, which represent the peak intensities and angles from the alpha, beta, and omega phase standards. In doing so, one can see that the peaks from the XRD plots largely align with

the peaks noted on the ICSD standards for alpha and beta Ti, but do not match with the peaks in the omega Ti standard. Collectively, this data suggests that the Ti substrates should have enhanced material strength characteristics from HPT processing while also maintaining an acceptable level of ductility associated with the alpha and beta Ti phases.

a)

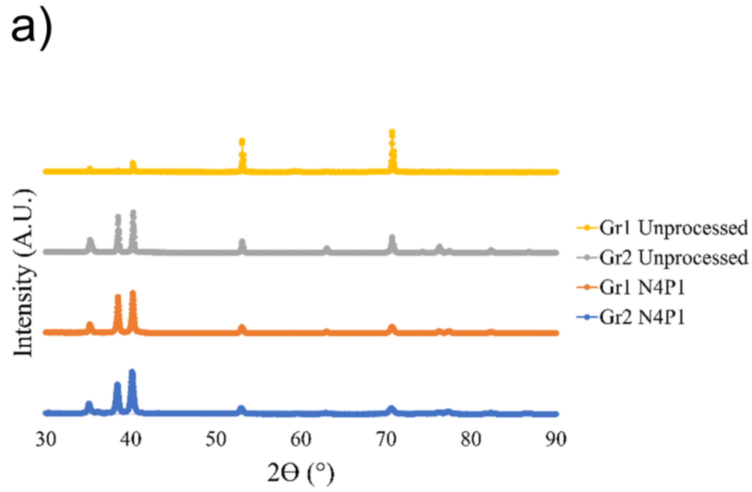

b)

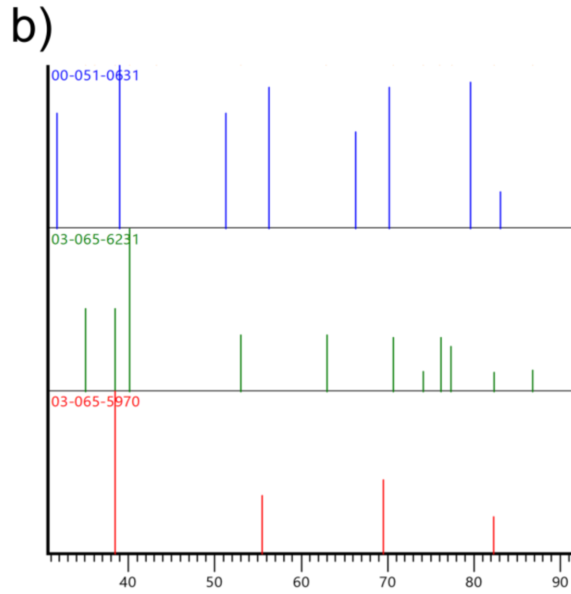

Figure 5-4. Results from x-ray diffraction and Highscore Plus analysis depicting a) normalized x-ray diffraction plots of unprocessed, commercially pure, grade 1 and grade 2 Ti and commercially pure, grade 1 and grade 2 Ti that was processed with HPT at 4 turns and a pressure of 1 GPa; and b) stick diagram standards for the omega, alpha, and beta phases of Ti, respectively.

5.3.2 Vickers hardness

The average values of the Vickers hardness values (H_v) were plotted as a function of the distance from the center of each disc. Figure 5-5 depicts the results from this indentation testing with 0 distance representing the center and 5 representing the edge of each disc. The H_v of the unprocessed grade 1 Ti controls, grade 2 Ti controls and 316L SS benchmark were largely consistent across the samples as expected. The average H_v values were measured to be 918 ± 35, 1929 ± 72, and 1687 ± 45 MPa, respectively. Meanwhile, the average H_v values for the grade 1 and grade 2 Ti samples processed with HPT using 4 turns and 1 GPa of pressure were significantly higher with measured values of 2212 ± 52 MPa and 2953 ± 134 MPa which represents H_v increases of 141% and 53%, respectively.

It is widely-accepted that the shear strain experienced during the HPT process is dependent upon the distance from the center of rotation and is given by the relationship:

$$\gamma = \frac{2\pi N R_d}{h}$$

where N is the number of rotations used during processing, R_d is the distance from the center of the disc, and h is the thickness of the sample (Wang et al. 2014). As a result, inhomogeneities are expected in the average H_v values of HPT-processed samples. Figure 5-5 depicts slight increases in H_v as the distance from the center increases, but there is a relatively large amount of homogeneity in the HPT-processed samples overall.

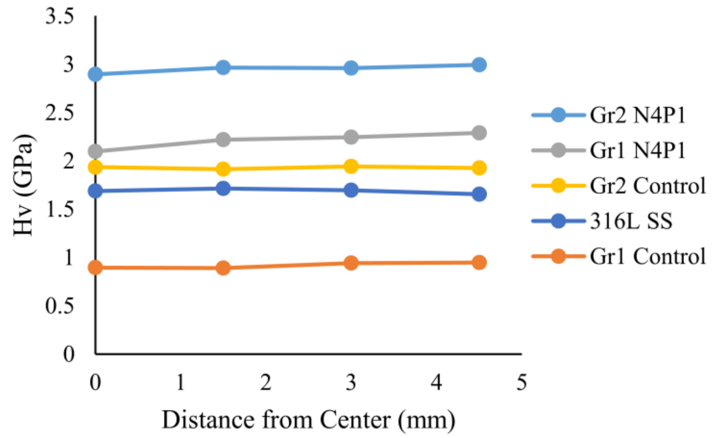

Figure 5-5. Plot depicting average Vickers hardness measurements from indenter testing on grade 1 and grade 2 unprocessed Ti samples and grade 1 and grade 2 Ti samples processed with HPT using 4 turns and 1 GPa of pressure. Indentation testing was performed in triplicate across different substrates for each set of parameters.

5.3.3 Grain size refinement

The microstructures of the Ti samples are depicted in Figure 5-6 with unprocessed Ti samples on the left and the corresponding samples processed with HPT using 4 turns and 1 GPa of pressure on the right. These microstructure samples were obtained near the edge of the Ti discs, roughly 4.5 mm from the center, and should therefore depict the largest changes in grain size. The microstructures of both HPT-processed samples depict texturing and sporadic dense accumulations of dislocations both within grains and along grain boundaries. Moreover, the definition of the grain boundaries in the HPT-processed samples are significantly less clear than the unprocessed samples, which is consistent with what others have reported in literature (Islamgaliev et al. 2008; Wang et al. 2014).

Using these micrograph images, grain sizes were estimated using the basic lineal intercept method. The average grain sizes of the unprocessed grade 1 and grade 2 Ti control samples were estimated to be 121 ± 20 µm and 16 ± 1 µm, respectively. The corresponding average grain sizes after HPT processing with 4 turns and 1 GPa of pressure were estimated to be 310 ± 60 nm and 180 ± 29 nm, respectively, which represents a significant reduction in grain size.

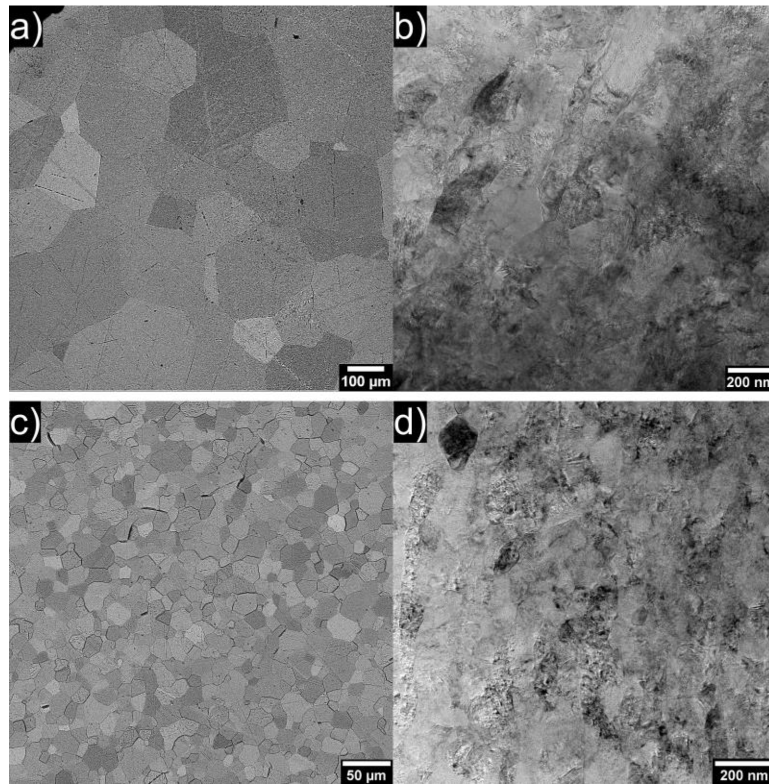

Figure 5-6. SEM and TEM micrographs depicting the microstructure of a) unprocessed grade 1 Ti, b) grade 1 Ti processed with HPT using 4 turns and 1 GPa of pressure, c) unprocessed grade 2 Ti, and d) grade 2 Ti processed with HPT using 4 turns and 1 GPa of pressure.

5.3.4 Feasibility testing

Figure 5-7 depicts early Ti DRIE process development for a fenestrated MN made out of commercially pure, grade 1 Ti that was processed with HPT using 4 turns and 1 GPa of pressure. Severe undercutting was observed during post-etch characterization which highlighted the need for etch parameter adjustments. Based upon the results of the optimization study of Ti DRIE parameters in Chapter 3, oxygen flowrate was significantly increased to promote sidewall passivation in subsequent process development iterations. Figure 5-8 depicts the results of one of these later Ti DRIE process development attempts where increased oxygen flowrate led to the formation of additional protective sidewall passivation on the fenestrated MN pattern.

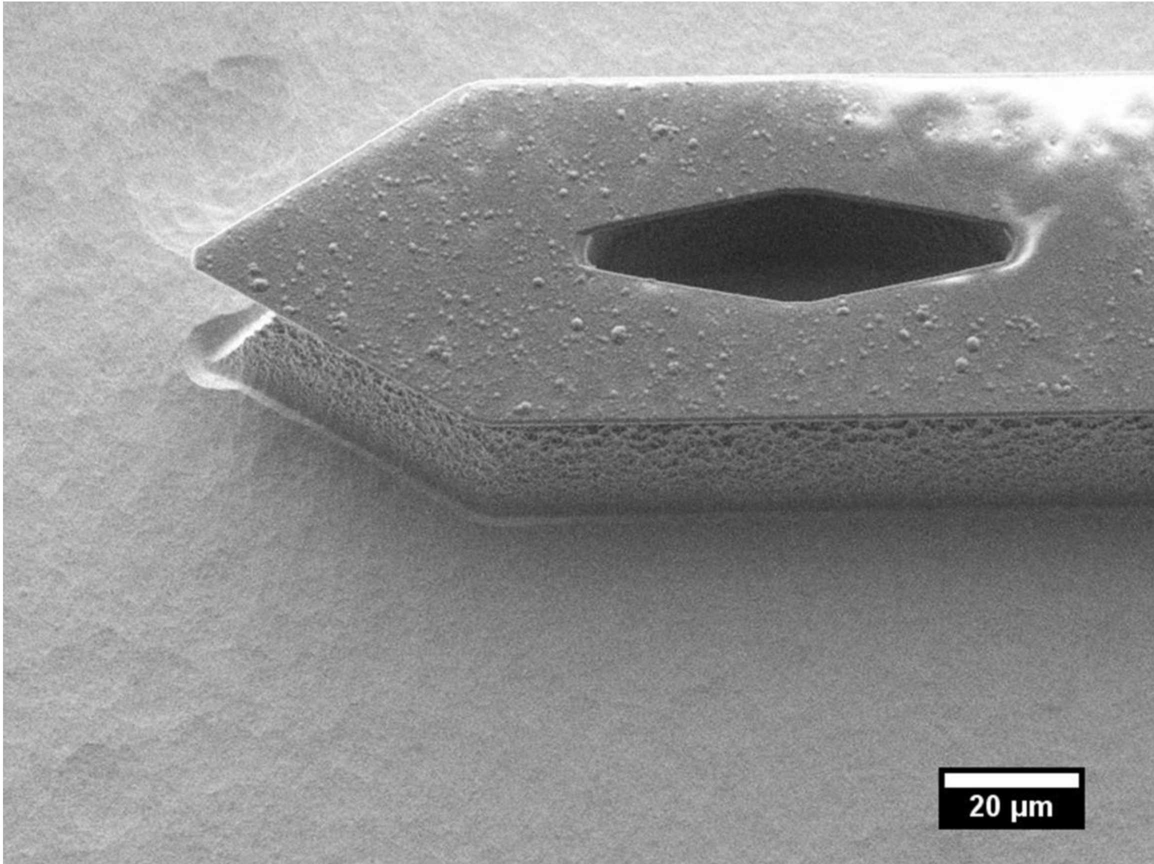

Figure 5-7. SEM micrograph depicting the needle shank of a fenestrated MN that is etched in a commercially pure, grade 1 Ti substrate that was processed with HPT using 4 turns and 1 GPa of pressure. Processing conditions consist of 20 mTorr chamber pressure, 2500 W source power, 125 W substrate power, 250 sccm chlorine flowrate, and an oxygen flowrate that ramps from 0.5 to 1.5 sccm. Etch time was 10 minutes. Significant undercutting is present.

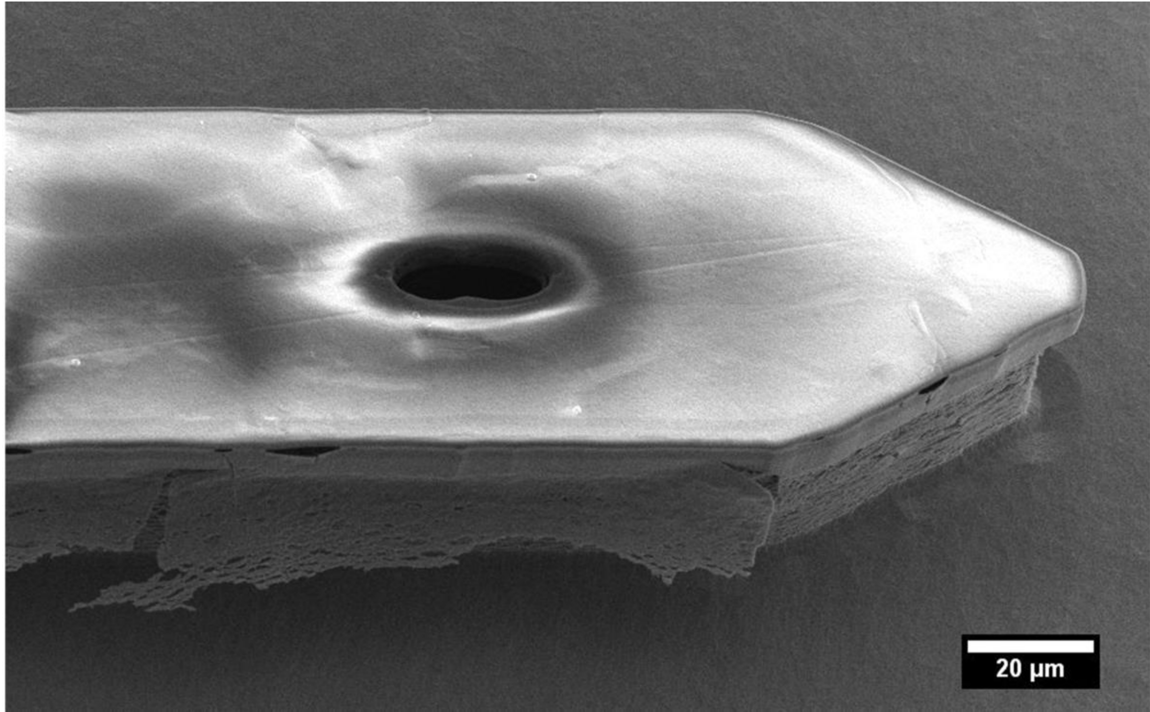

Figure 5-8. SEM micrograph depicting Ti DRIE process development for fabrication of a fenestrated, HPT-processed Ti MN using increased oxygen flowrate to promote sidewall passivation. Processing conditions consist of 20 mTorr chamber pressure, 2500 W source power, 125 W substrate power, 250 sccm chlorine flowrate, and an oxygen flowrate that ramps from 8 to 11 sccm. Etch time was 14 minutes. Significant sidewall passivation is present on the needle length while a smooth, near-vertical sidewall is revealed underneath near the needle tip.

5.4 Discussion

This section is devoted to discussing the results from the fenestrated HPT-processed titanium MN study. It has been split into three subsections which are focused on discussing the underlying mechanisms of HPT processing, further analyzing the results of this study and comparing them to other HPT processes reported in literature, and exploring Ti DRIE parameter adjustments for HPT-processed Ti.

5.4.1 Underlying mechanisms of high-pressure torsion processing

Modern HPT processing involving a rotational anvil is a relatively well-known severe plastic deformation technique that was initiated in 1935 by Percy Bridgman (Edalati et al. 2016). Over the years, HPT processing technology has advanced, but the methodology largely remains the same. A disc-shaped sample is squeezed between two anvils under a very high pressure, and a concurrent shear strain is applied to the disc by rotating one anvil with respect to the other. By modulating the pressure and rotational parameters, a large shear strain can be applied to create significant grain refinement while the hydrostatic pressure from the anvils prevents fracture and crack propagation.

HPT processing has been used on a wide range of materials to manipulate different material characteristics such as lattice defects; solid-state reactions; thermal, corrosion, irradiation, and fatigue resistance; electrical and thermal conductivity; hydrogen storage; plasticity; strength; ductility; and hardness (Harish et al. 2014; Kawasaki et al. 2014; Edalati et al. 2013; Edalati et al. 2016; Nie et al. 2010). Despite its extensive history and use, the underlying grain refinement mechanism is still not

understood. Many theories have been proposed, and the generally accepted prevailing theory is that the large shear strain activates dislocation sources within the material. As more dislocations are created, they start to move and pile up in orientations that are energetically favorable. As the dislocation density increases, plastic deformation occurs which leads to grain misorientations or the formation of subgrain boundaries. These subgrain boundaries then transition into refined grains as additional stress is applied and dislocations increase the grain boundary misorientations (Estrin et al. 2013).

5.4.2 Comparison to other high-pressure torsion processes

Reports in literature suggest that the alpha Ti to omega Ti phase change occurs when an applied pressure of 4 GPa or higher is used during the severe plastic deformation process (Edalati et al. 2010). This is relevant to our study since processing pressures consisting of 1 or 2 GPa were used during the HPT processing of our Ti discs, and the XRD diffraction patterns suggest that no omega phase change occurred. A couple unidentified peaks were noted in the phase characterization process, but further investigation led us to believe that these were probably attributed to carbon contamination, possibly from the polishing process, or to the modeling clay that was used for mounting the sample(s) for XRD scanning.

The indentation testing results revealed that the Vickers hardness values of the HPT-processed Ti samples were far superior to the unprocessed Ti controls and the 316L SS benchmark. The Vickers hardness values of the HPT-processed Ti samples, ~2.2 and ~3.0 GPa, respectively represent increases of 141% and 53% compared to the

unprocessed controls. Furthermore, these values also fall within the expected range of 2 to 4 GPa reported by others in literature for similar materials (Shirooyeh et al. 2014). In addition, Figure 5.5 reveals relatively consistent Vickers hardness values across each of the samples' surfaces which suggests that the HPT processing parameter of 4 turns was sufficient for acceptable hardness homogeneity. This is supported by other publications which identify complete sample surface homogeneity after 5 or 10 turns of processing (Shirooyeh et al. 2014; Nie et al. 2014; Wang et al. 2013; Zhilyaev et al. 2008).

5.4.3 Ti DRIE adjustments for high-pressure torsion-processed titanium

Figure 5-7 depicts early Ti DRIE process development for a fenestrated, HPT-processed Ti MN that was etched for 10 minutes using a ramping oxygen flowrate that increased from 0.5 sccm to 1.5 sccm. Significant undercutting was observed which we believe can be attributed to the large increase in volume fraction of grain boundaries associated with the HPT-processed material. Previous studies have suggested that grain size plays an important role in determining the plasma etch rate since reactive ions adsorb more slowly through bulk grains than grain boundaries (Liu et al. 2008). Based upon this information, we believe that the increased etch rate may have inhibited sidewall passivation and led to undercutting by removing material faster than the passivation layer could form. Surface profilometry seems to support this conjecture. We calculated the Ti etch rates for the HPT-processed material and the unprocessed material to be ~3.3 μm/min and ~2.8 μm /min, respectively, which represents a considerable difference.

To address the isotropy of the etch, we determined that additional sidewall passivation was needed. We previously identified chamber pressure and oxygen flowrate as the critical factors for sidewall passivation and decided to increase the oxygen flowrate values. Figure 5-8 depicts one of these later Ti DRIE parameter adjustments where the fenestrated, HPT-processed Ti MN pattern was etched for 14 minutes using a ramping oxygen flowrate that increased from 8 sccm to 11 sccm. The formation of a protective sidewall passivation layer is clearly evident, and the needle tip, where passivation has been removed, reveals a smooth, near-vertical sidewall. Furthermore, the surrounding area is smooth, with no apparent micromasking effects which suggests that microdevices could be successfully fabricated from the HPT-processed Ti material using Ti DRIE. Although further optimization could result in better feature definition, these results satisfactorily prove that HPT processing and Ti DRIE are compatible.

6 CONCLUSIONS

6.1 Conclusions

This section is devoted to concluding remarks for the research studies discussed in this work. It has been split into two subsections with one devoted to each of the major studies, optimization of small-scale feature fabrication in titanium and high-pressure torsion-processed titanium microneedles.

6.1.1Optimization of small-scale feature fabrication in titanium

We reported the development of a new Ti DRIE process that seeks to enable titanium feature fabrication deep into the submicrometer realm for the first time. We explored the chamber pressure, chlorine flowrate, and oxygen flowrate parameters and have shown that chamber pressure and oxygen flowrate are the critical variables for ensuring clearly defined high-aspect ratio features with smooth, vertical sidewalls in this length-scale regime. This is presumably attributed to their respective contributions to maintaining sidewall passivation. Based upon this understanding, we have developed an ultrahigh resolution Ti DRIE process that now enables definition of high-aspect ratio structures in bulk Ti substrates with minimum feature sizes as small as 150 nm. This represents a five-fold improvement relative to the earlier Ti DRIE process and a 29-fold or greater improvement compared with more recent processes reported by others. As a result, this represents a considerable extension of the state-of-the-art in Ti DRIE, and opens significant new opportunities, including further miniaturization of Ti MEMS and the potential for enhancing the performance of implantable medical devices through rational design of submicrometer surface patterning.

6.1.2 High-pressure torsion-processed titanium microneedles

We have reported the successful integration of HPT processing and Ti DRIE in a fabrication process that seeks to enable Ti-based MEMS devices with enhanced mechanical properties. We investigated HPT processing parameters for grade 1 and grade 2 Ti to improve their material properties through grain refinement while avoiding an omega phase change. We also determined that the standard Ti DRIE parameters must be altered in order to account for the significant increase in grain boundaries which were likely causing issues with undercutting. Based upon this understanding, we have created a process that demonstrates the compatibility and viability of combining HPT processing for grain refinement with Ti DRIE for microdevice fabrication. Using these techniques, we report, for the first time, the realization of a fine-grained Ti-based fenestrated MN with significant mechanical property enhancements. As a result, this not only represents a considerable extension of the state-of-the-art in Ti MEMS technology, but also opens significant new opportunities, including the ability to create commercially pure, grade 1 Ti with properties that are non-inferior or superior to other common biomaterials and the realization of Ti-based microdevices with mechanical properties that are tailored to their specific applications.

6.2 Recommendations for Future Work

This section is devoted to offering insight into possible directions for future research regarding studies discussed in this work. It has been split into two distinct subsections to better differentiate between projects.

6.2.1 Optimization of small-scale feature fabrication in titanium

The work described herein has promising potential for device miniaturization and the realization of deep submicrometer scale features in bulk Ti substrates. However, it is important to acknowledge potential limitations and improvements of this study. First, this study was performed in a linear method, and parameter results were studied largely independent from one another. However, it is conceivable that a combination of variable adjustments could lead to superior results, especially considering that our results suggest multiple parameters can influence the same component.

Research could be performed to shed light onto the interrelationships between the processing parameters and help to improve understanding of the influence each parameter has upon feature definition. A specialized design of experiments method such as Taguchi or ANOVA could then potentially be used to hone in on a set of parameter adjustments for even better etch conditions.

Secondly, it should be clear that this parameter study was optimized for grating features with the intent of improving rational design of surface patterning. However, experience with Ti DRIE has taught us that one should expect deviations from the norm when different features and/or scale are used. For instance, the optimized parameters listed herein may not be suitable for circular features or gratings with different pitch.

Research could be performed to investigate these optimized parameters using different pattern types and gain additional insight into the robustness of the processing variables. Furthermore, experimentation regarding sidewall passivation could offer

significant potential for better understanding the underlying Ti DRIE mechanisms and provide methodology for even greater etch optimization and device miniaturization.

Thirdly, the cell studies cited in this work were performed *in-vitro*, using the same grating pattern. It is possible that other rationally-designed surface patterning types may prove to be even more advantageous for modulating cellular behavior. Furthermore, *in-vivo* studies may reveal variations in cell response or provide additional insight regarding rationally-designed surface patterning types and sizes.

Research could be performed to study different cellular responses to different rationally-designed surface patterning types and begin creating an index of the optimal patterning shape and size for different implants. Moreover, *in-vivo* studies could be performed which would add significant credibility to the implications and conclusions drawn from the *in-vitro* studies performed thus far.

6.2.2 High-pressure torsion-processed titanium microneedles

The high-pressure torsion-processed titanium microneedle study was performed with the intent of testing the feasibility of combining HPT processing and Ti DRIE for the realization of MEMS devices with enhanced material properties. It should therefore be easy to recognize that there is significant room for additional development and improvement regarding the integration of these two techniques. First, limitations were imposed upon the HPT processing parameters to avoid an omega phase change since reports in literature associate omega Ti with significant increases in hardness and

brittleness. However, the specific parameters that trigger this phase change are unknown, which means there is potential for HPT parameter optimization.

Studies could be conducted to analyze HPT processing parameters and gain a better understanding of the omega phase change transition point. Once the processing parameters for omega Ti have been determined, the HPT processing parameters can be optimized to obtain specific material characteristics depending on the Ti-based MEMS application. For instance, Ti-based cardiovascular stents require increased strength and ductility, whereas Ti-based fenestrated MNs require increased strength and stiffness.

Secondly, the MN design used in this study was based upon ones previously used by Khandan et al. Their study used a variety of fenestrated MN designs that were scaled based upon the MN width and length. However, finite element analysis simulations reveal that this design experiences localized failure which cascades into device buckling. As a result, there is room for both material and design improvement with these devices.

Additional research could be performed to improve the fenestrated MN device design. Material properties from characterizing optimized HPT-processed Ti could be used to produce more accurate simulation results and aid in further design iterations. It is important to balance the MN's ability to safely and effectively penetrate scleral and corneal tissue with its drug loading capability. This will increase the safety and effectiveness of the MN injection capability while also minimizing how many MNs are necessary in the array for proper dosage.

BIBLIOGRAPHY

Abhyankar, Atul D., and Ashok S. Thakkar. 2012. "In Vivo Assessment of Stent Recoil of Biodegradable Polymer-Coated Cobalt-Chromium Sirolimus-Eluting Coronary Stent System." *Indian Heart Journal* 64 (6): 541–46. https://doi.org/10.1016/j.ihj.2012.07.005.

Afshari, Fardad, Chris Jacobs, James Fawcett, and Keith Marti. 2012. "Wet Age Related Macular Degeneration." *Age Related Macular Degeneration - The Recent Advances in Basic Research and Clinical Care*, no. January: 1–24. https://doi.org/10.5772/32393.

Aimi, Marco F., Masa P. Rao, Noel C. MacDonald, Abu Samah Zuruzi, and David P. Bothman. 2004. "High-Aspect-Ratio Bulk Micromachining of Titanium." *Nature Materials* 3 (2): 103–5. https://doi.org/10.1038/nmat1058.

American Heart Association. 2017. "Cardiovascular Disease: A Costly Burden for America." *American Heart Association CVD Burden Report*, 1–14.

Anderson, James M, Analiz Rodriguez, and David T Chang. 2008. "Foreign Body Reaction to Biomaterials." *Seminars in Immunology* 20: 86–100. https://doi.org/10.1016/j.smim.2007.11.004.

Ang, Hui Ying, Heerajnarain Bulluck, Philip Wong, Subbu S Venkatraman, Yingying Huang, and Nicolas Foin. 2017. "Bioresorbable Stents : Current and Upcoming Bioresorbable Technologies." *International Journal of Cardiology* 228: 931–39. https://doi.org/10.1016/j.ijcard.2016.11.258.

Ang, Hui Ying, Ying Ying Huang, Soo Teik Lim, Philip Wong, Michael Joner, and Nicolas Foin. 2017. "Mechanical Behavior of Polymer-Based vs . Metallic-Based Bioresorbable Stents." *Journal of Thoracic Disease* 9 (Suppl 9): S923–34. https://doi.org/10.21037/jtd.2017.06.30.

Benjamin, Emelia J., Salim S. Virani, Clifton W. Callaway, Alanna M. Chamberlain, Alexander R. Chang, Susan Cheng, Stephanie E. Chiuve, et al. 2018. *Heart Disease and Stroke Statistics - 2018 Update: A Report from the American Heart Association*. *Circulation*. Vol. 137. https://doi.org/10.1161/CIR.0000000000000558.

Bettinger, By Christopher J, Zhitong Zhang, Sharon Gerecht, Jeffrey T Borenstein, and Robert Langer. 2008. "Enhancement of In Vitro Capillary Tube Formation by Substrate Nanotopography **." *Advanced Materials* 20: 99–103. https://doi.org/10.1002/adma.200702487.

Biela, Sarah A, Yi Su, Joachim P Spatz, and Ralf Kemkemer. 2009. “Different Sensitivity of Human Endothelial Cells , Smooth Muscle Cells and Fibroblasts to Topography in the Nano – Micro Range.” *Acta Biomaterialia* 5 (7): 2460–66. https://doi.org/10.1016/j.actbio.2009.04.003.

Bustillo, James M., Roger T. Howe, and Richard S. Muller. 1998. “Surface Micromachining For Microelectromechanical Systems.” *Proceedings of the IEEE* 86 (8): 1552–74.

Buttiglieri, S, D Pasqui, M Migliori, H Johnstone, S Affrossman, and L Sereni. 2003. “Endothelization and Adherence of Leucocytes to Nanostructured Surfaces.” *Biomaterials* 24: 2731–38. https://doi.org/10.1016/S0142-9612(03)00088-7.

Byrne, Robert A., Michael Joner, and Adnan Kastrati. 2015. “Stent Thrombosis and Restenosis: What Have We Learned and Where Are We Going? The Andreas Gruntzig Lecture ESC 2014.” *European Heart Journal* 36: 3320–31. https://doi.org/10.1093/eurheartj/ehv511.

CDC. 2017. “Deaths from Coronary Heart Disease.” Interactive Atlas of Heart Disease and Stroke. 2017. http://nccd.cdc.gov/DHDSPAtlas.

CDC. 2018. “Learn About Age-Related Macular Degeneration.” Centers for Disease Control and Prevention. 2018. https://www.cdc.gov/features/healthyvisionmonth/index.html.

CDC and NCHS. 2016. “Heart Disease Fact Sheet.” Centers for Disease Control and Prevention. 2016. https://www.cdc.gov/dhdsp/data_statistics/fact_sheets/fs_heart_disease.htm.

Chen, Yongjun, Zhigang Xu, Christopher Smith, and Jag Sankar. 2014. “Recent Advances on the Development of Magnesium Alloys for Biodegradable Implants.” *Acta Biomaterialia* 10 (11): 4561–73. https://doi.org/10.1016/j.actbio.2014.07.005.

Choudhary, Saba, Mikal Berhe, Karen M. Haberstroh, and Thomas J. Webster. 2006. “Increased Endothelial and Vascular Smooth Muscle Cell Adhesion on Nanostructured Titanium and CoCrMo.” *International Journal of Nanomedicine* 1 (1): 41–49.

Collet, Carlos, Yohei Sotomi, Rafael Cavalcante, Pannipa Suwannasom, Erhan Tenekecioglu, Yoshinobu Onuma, and Patrick W. Serruys. 2016. “Coronary Stent Thrombosis: What Have We Learned?” *Journal of Thoracic Disease* 8 (7): 1398–1405. https://doi.org/10.21037/jtd.2016.05.69.

D'Agostino, R, F Fracassi, and C Pacifico. 1992. "Dry Etching of Ti in Chlorine Containing Feeds." *Journal of Applied Physics* 72 (462): 4351–57. https://doi.org/10.1063/1.352199.

Domanski, M., R. Luttge, E. Lamers, X. F. Walboomers, L. Winnubst, J. A. Jansen, and J. G.E. Gardeniers. 2012. "Submicron-Patterning of Bulk Titanium by Nanoimprint Lithography and Reactive Ion Etching." *Nanotechnology* 23 (6). https://doi.org/10.1088/0957-4484/23/6/065306.

Edalati, Kaveh, and Zenji Horita. 2016. "A Review Article A Review on High-Pressure Torsion (HPT) from 1935 to 1988." *Materials Science & Engineering A* 652: 325–52. https://doi.org/10.1016/j.msea.2015.11.074.

Edalati, Kaveh, Zenji Horita, Masaki Tanaka, and Kenji Higashida. 2010. "High Pressure Torsion of Pure Ti: Effect of Pressure and Strain on Allotropy." *Advanced Materials Research* 89–91: 171–76. https://doi.org/10.4028/www.scientific.net/AMR.89-91.171.

Edalati, Kaveh, Junko Matsuda, Hideaki Iwaoka, Shoichi Toh, Etsuo Akiba, and Zenji Horita. 2013. "High-Pressure Torsion of TiFe Intermetallics for Activation of Hydrogen Storage at Room Temperature with Heterogeneous Nanostructure." *International Journal of Hydrogen Energy* 38 (11): 4622–27. https://doi.org/10.1016/j.ijhydene.2013.01.185.

Engler, Adam J, Shamik Sen, H Lee Sweeney, and Dennis E Discher. 2006. "Matrix Elasticity Directs Stem Cell Lineage Specification." *Cell* 126: 677–89. https://doi.org/10.1016/j.cell.2006.06.044.

Estrin, Y., and A. Vinogradov. 2013. "Extreme Grain Refinement by Severe Plastic Deformation: A Wealth of Challenging Science." *Acta Materialia* 61 (3): 782–817. https://doi.org/10.1016/j.actamat.2012.10.038.

Falavarjani, K. Ghasemi, and Q. D. Nguyen. 2013. "Adverse Events and Complications Associated with Intravitreal Injection of Anti-VEGF Agents: A Review of Literature." *Eye* 27 (7): 787–94. https://doi.org/10.1038/eye.2013.107.

Garg, Koyal, Nicholas A Pullen, Carole A Oskeritzian, John J Ryan, and Gary L Bowlin. 2013. "Biomaterials Macrophage Functional Polarization (M1 / M2) in Response to Varying Fi Ber and Pore Dimensions of Electrospun Scaffolds." *Biomaterials* 34 (18): 4439–51. https://doi.org/10.1016/j.biomaterials.2013.02.065.

Gillespie, Cathleen D., Charles Wiginton, and Yuling Hong. 2013. "Coronary Heart Disease and Stroke Deaths." *CDC Health Disparities and Inequalities Report—United States, 2013* 62 (3): 81–84. https://doi.org/PMID: 24264501.

Gordois, Adam, Lynne Pezzullo, and Henry Cutler. 2010. "The Global Economic Cost of Visual Impairment." *Access Economics Pty Limited*. http://www.icoph.org/dynamic/attachments/resources/globalcostofvi_finalreport.pdf.

Gotman, Irena. 1997. "Characteristics of Metals Used in Implants." *Journal of Endourology* 11 (6): 383–89.

Gott, Shannon C., Benjamin A. Jabola, and Masaru P. Rao. 2015. "Vascular Stents with Submicrometer-Scale Surface Patterning Realized via Titanium Deep Reactive Ion Etching." *Journal of Micromechanics and Microengineering* 25 (8): 1–11. https://doi.org/10.1088/0960-1317/25/8/085016.

Gupta, Vishal, Bhooma R Aravamuthan, Susan Baskerville, Susan K Smith, Vijaya Gupta, Michael A Lauer, and Tim A Fischell. 2004. "Reduction of Subacute Stent Thrombosis (SAT) Using Heparin-Coated Stents in a Large-Scale, Real World Registry." *The Journal of Invasive Cardiology* 16 (6): 304–10. http://www.ncbi.nlm.nih.gov/pubmed/15155999.

Harish, Sivasankaran, Mitsuru Tabara, Yoshifumi Ikoma, Zenji Horita, Yasuyuki Takata, David G. Cahill, and Masamichi Kohno. 2014. "Thermal Conductivity Reduction of Crystalline Silicon by High-Pressure Torsion." *Nanoscale Research Letters* 9 (326): 1–5. https://doi.org/10.1186/1556-276X-9-326.

Holmes, David R., Dean J. Kereiakes, Warren K. Laskey, Antonio Colombo, Stephen G. Ellis, Timothy D. Henry, Jeffrey J. Popma, et al. 2007. "Thrombosis and Drug-Eluting Stents: An Objective Appraisal." *Journal of the American College of Cardiology* 50 (2): 109–18. https://doi.org/10.1016/j.jacc.2007.04.032.

Huang, Yingying, Yee Shan Wong, Herr Cheun, Anthony Ng, and Freddy Y. C. Boey. 2017. "Translation in Cardiovascular Stents and Occluders : From Biostable to Fully Degradable." *Bioengineering & Translational Medicine* 2: 156–69. https://doi.org/10.1002/btm2.10066.

Islamgaliev, R. K., V. U. Kazyhanov, L. O. Shestakova, A. V. Sharafutdinov, and R. Z. Valiev. 2008. "Microstructure and Mechanical Properties of Titanium (Grade 4) Processed by High-Pressure Torsion." *Materials Science and Engineering A* 493: 190–94. https://doi.org/10.1016/j.msea.2007.08.084.

Jaffe, Ronen, and Bradley H. Strauss. 2007. "Late and Very Late Thrombosis of Drug-Eluting Stents. Evolving Concepts and Perspectives." *Journal of the American College of Cardiology* 50 (2): 119–27. https://doi.org/10.1016/j.jacc.2007.04.031.

Jansen, H V, M J de Boer, S Unnikrishnan, M C Louwerse, and M C Elwenspoek. 2009. “Black Silicon Method X : A Review on High Speed and Selective Plasma Etching of Silicon with Profile Control : An in-Depth Comparison between Bosch and Cryostat DRIE Processes as a R ...” *Journal of Microelectromechs and Microengineering* 19. https://doi.org/10.1088/0960-1317/19/3/033001.

Jiang, Jason, Harvinder S. Gill, Deepta Ghate, Bernard E. McCarey, Samir R. Patel, Henry F. Edelhauser, and Mark R. Prausnitz. 2007. “Coated Microneedles for Drug Delivery to the Eye.” *Investigative Ophthalmology and Visual Science* 48 (9): 4038–43. https://doi.org/10.1167/iovs.07-0066.

Jiang, Jason, Jason S. Moore, Henry F. Edelhauser, and Mark R. Prausnitz. 2009. “Intrascleral Drug Delivery to the Eye Using Hollow Microneedles.” *Pharmaceutical Research* 26 (2): 395–403. https://doi.org/10.1007/s11095-008-9756-3.

Joner, Michael, Aloke V. Finn, Andrew Farb, Erik K. Mont, Frank D. Kolodgie, Elena Ladich, Robert Kutys, Kristi Skorija, Herman K. Gold, and Renu Virmani. 2006. “Pathology of Drug-Eluting Stents in Humans Delayed Healing and Late Thrombotic Risk.” *Journal of the American College of Cardiology* 48 (1): 193–202. https://doi.org/10.1016/j.jacc.2006.03.042.

Jorge, Claudia, and Christophe Dubois. 2015. “Clinical Utility of Platinum Chromium Bare-Metal Stents in Coronary Heart Disease.” *Medical Devices: Evidence and Research*, 359–67.

Kawasaki, Megumi, Han Joo Lee, Byungmin Ahn, Alexander P. Zhilyaev, and Terence G. Langdon. 2014. “Evolution of Hardness in Ultrafine-Grained Metals Processed by High-Pressure Torsion.” *Journal of Materials Research and Technology* 3 (4): 311–18. https://doi.org/10.1016/j.jmrt.2014.06.002.

Khandan, Omid, Malik Y. Kahook, and Masaru P. Rao. 2016. “Fenestrated Microneedles for Ocular Drug Delivery.” *Sensors and Actuators, B: Chemical* 223: 15–23. https://doi.org/10.1016/j.snb.2015.09.071.

Kim, Yoo C., Henry F. Edelhauser, and Mark R. Prausnitz. 2014. “Targeted Delivery of Antiglaucoma Drugs to the Supraciliary Space Using Microneedles.” *Investigative Ophthalmology & Visual Science* 55 (11): 7387–97. https://doi.org/10.1167/iovs.14-14651.

Kim, Yoo C., Hans E. Grossniklaus, Henry F. Edelhauser, and Mark R. Prausnitz. 2014. “Intrastromal Delivery of Bevacizumab Using Microneedles to Treat Corneal Neovascularization.” *Investigative Ophthalmology & Visual Science* 55 (11): 7376–86. https://doi.org/10.1167/iovs.14-15257.

Kolb, Helga, Eduardo Fernandez, and Ralph Nelson. 2018. *Webvision The Organization of the Retina and Visual System*. http://webvision.med.utah.edu/.

Lee, Junmin, Amr A Abdeen, Douglas Zhang, and Kristopher A Kilian. 2013. "Biomaterials Directing Stem Cell Fate on Hydrogel Substrates by Controlling Cell Geometry , Matrix Mechanics and Adhesion Ligand Composition." *Biomaterials* 34 (33): 8140–48. https://doi.org/10.1016/j.biomaterials.2013.07.074.

Levine, Glenn N. 2017. "Balancing Ischemic and Bleeding Risks of Prolonged Dual Antiplatelet Therapy." *Journal of the American Medical Association* 318 (2): 194–95. https://doi.org/10.1001/jamacardio.2017.0063.

Lin, Che-Hsin. 2008. "Bulk Micromachining." In *Encyclopedia of Microfluidics and Nanofluidics*, 164–73.

Liu, Guojun, Tanjim Tanaka-Ahmed, Yue Kuo, Denis N. Buckley, and Shafaat Ahmed. 2008. "Grain-Size Effect on a Plasma-Based Copper Etch Process." *Journal of The Electrochemical Society* 155 (6): H432. https://doi.org/10.1149/1.2904937.

Lu, Jing, Masaru P Rao, Noel C Macdonald, Dongwoo Khang, and Thomas J Webster. 2008. "Improved Endothelial Cell Adhesion and Proliferation on Patterned Titanium Surfaces with Rationally Designed , Micrometer to Nanometer Features." *Acta Biomaterialia* 4: 192–201. https://doi.org/10.1016/j.actbio.2007.07.008.

Lüscher, Thomas F., Jan Steffel, Franz R. Eberli, Michael Joner, Gaku Nakazawa, Felix C. Tanner, and Renu Virmani. 2007. "Drug-Eluting Stent and Coronary Thrombosis: Biological Mechanisms and Clinical Implications." *Circulation* 115 (8): 1051–58. https://doi.org/10.1161/CIRCULATIONAHA.106.675934.

Luu, Thuy U., Shannon C. Gott, Bryan W.K. Woo, Masaru P. Rao, and Wendy F. Liu. 2015. "Micro- and Nanopatterned Topographical Cues for Regulating Macrophage Cell Shape and Phenotype." *ACS Applied Materials and Interfaces* 7 (51): 28665–72. https://doi.org/10.1021/acsami.5b10589.

Ma, Qian-li, Ling-zhou Zhao, Rong-rong Liu, Bo-quan Jin, Wen Song, Ying Wang, Yu-si Zhang, Li-hua Chen, and Yu-mei Zhang. 2014. "Biomaterials Improved Implant Osseointegration of a Nanostructured Titanium Surface via Mediation of Macrophage Polarization." *Biomaterials* 35 (37): 9853–67. https://doi.org/10.1016/j.biomaterials.2014.08.025.

Mackay, Judith, and George A. Mensah. 2004. *The Atlas of Heart Disease and Stroke*. World Health Organization.

Madou, Marc J. 2002. *Fundamentals of Microfabrication : The Science of Miniaturization*. CRC Press. https://books.google.com/books?id=90ZZDwAAQBAJ.

Mao, Lin, Jiahui Chen, Xiaobo Zhang, Minsuk Kwak, Yu Wu, Rong Fan, Lei Zhang, et al. 2017. "A Promising Biodegradable Magnesium Alloy Suitable for Clinical Vascular Stent Application." *Scientific Reports*, 1–12. https://doi.org/10.1038/srep46343.

Martinez, Adam W., and Elliot L. Chaikof. 2011. "Microfabrication and Nanotechnology in Stent Design." *Wiley Interdisciplinary Reviews: Nanomedicine and Nanobiotechnology* 3 (3): 256–68. https://doi.org/10.1002/wnan.123.

Martinez, Fernando O, and Siamon Gordon. 2014. "The M1 and M2 Paradigm of Macrophage Activation : Time for Reassessment." *Prime Reports* 6 (13): 1–13. https://doi.org/10.12703/P6-13.

McCarthy, Patrick T., Kevin J. Otto, and Masaru P. Rao. 2011. "Robust Penetrating Microelectrodes for Neural Interfaces Realized by Titanium Micromachining." *Biomedical Microdevices* 13 (3): 503–15. https://doi.org/10.1007/s10544-011-9519-5.

Mcgrath, D J, B O'Brien, M Bruzzi, and P E Mchugh. 2014. "Nitinol Stent Design – Understanding Axial Buckling." *Journal of the Mechanical Behavior of Biomedical Materials* 40: 252–63. https://doi.org/10.1016/j.jmbbm.2014.08.029.

Mcwhorter, Frances Y, Tingting Wang, Phoebe Nguyen, Thanh Chung, and Wendy F Liu. 2013. "Modulation of Macrophage Phenotype by Cell Shape." *Proceedings of the National Academy of Sciences of the United States of America* 110 (43): 17253–58. https://doi.org/10.1073/pnas.1308887110.

Mehta, Sonia. 2015. "Age-Related Macular Degeneration." *Primary Care: Clinics in Office Practice* 42: 377–91. https://doi.org/10.1016/j.pop.2015.05.009.

Mohan, Shilpi, and Anil Dhall. 2010. "A Comparative Study of Restenosis Rates in Bare Metal and Drug-Eluting Stents." *International Journal of Angiology* 19 (2): 66–72. https://doi.org/10.1055/s-0031-1278368.

Mori, Hiroyoshi, Michael Joner, Aloke V Finn, and Renu Virmani. 2016. "Malapposition : Is It a Major Cause of Stent Thrombosis ?" *European Heart Journal* 37: 1217–19. https://doi.org/10.1093/eurheartj/ehw006.

Moura, Camilla Christian Gomes, Darceny Zanetta-barbosa, Paula Dechichi, Valessa Florindo Carvalho, and Priscilla Barbosa Ferreira Soares. 2014. “Effects of Titanium Surfaces on the Developmental Profile of Monocytes / Macrophages.” *Brazilian Dental Journal* 25 (2): 96–103.

Nagaraja, Srinidhi, Stacey J L Sullivan, Philip R Stafford, Anne D Lucas, and Elon Malkin. 2018. “Impact of Nitinol Stent Surface Processing on In-Vivo Nickel Release and Biological Response.” *Acta Biomaterialia* 72: 424–33. https://doi.org/10.1016/j.actbio.2018.03.036.

Nakazawa, Gaku, Aloke V. Finn, Michael Joner, Elena Ladich, Robert Kutys, Erik K. Mont, Herman K. Gold, Allen P. Burke, Frank D. Kolodgie, and Renu Virmani. 2008. “Delayed Arterial Healing and Increased Late Stent Thrombosis at Culprit Sites After Drug-Eluting Stent Placement for Acute Myocardial Infarction Patients: An Autopsy Study.” *Circulation* 118 (11): 1138–45. https://doi.org/10.1161/CIRCULATIONAHA.107.762047.

NHLBI. 2019. “Atherosclerosis.” NIH; U.S. Department of Health and Human Services. 2019. https://www.nhlbi.nih.gov/health-topics/atherosclerosis.

Nie, F. L., Y. F. Zheng, Y. Cheng, S. C. Wei, and R. Z. Valiev. 2010. “In Vitro Corrosion and Cytotoxicity on Microcrystalline, Nanocrystalline and Amorphous NiTi Alloy Fabricated by High Pressure Torsion.” *Materials Letters* 64 (8): 983–86. https://doi.org/10.1016/j.matlet.2010.01.081.

Nie, Mengyan, Chuan Ting Wang, Minghong Qu, Nong Gao, Julian A. Wharton, and Terence G. Langdon. 2014. “The Corrosion Behaviour of Commercial Purity Titanium Processed by High-Pressure Torsion.” *Journal of Materials Science* 49 (7): 2824–31. https://doi.org/10.1007/s10853-013-7988-z.

O’Brien, Barry, and William Carroll. 2009. “The Evolution of Cardiovascular Stent Materials and Surfaces in Response to Clinical Drivers: A Review.” *Acta Biomaterialia* 5 (4): 945–58. https://doi.org/10.1016/j.actbio.2008.11.012.

Oldani, Carlos, and Alejandro Dominguez. 2012. “Titanium as a Biomaterial for Implants.” In *Recent Advances in Arthroplasty*, edited by Samo Fokter, 149–62. Intech.

Omar, Alfazir, Lakshmana K. Pendyala, John A. Ormiston, and Ron Waksman. 2016. “Review: Stent Fracture in the Drug-Eluting Stent Era.” *Cardiovascular Revascularization Medicine* 17 (6): 404–11. https://doi.org/10.1016/j.carrev.2016.06.002.

Oppeel, Arnout. 2015. “Experimental Characterisation and Finite Element Modeling of Biodegradable Magnesium Stents Arnout Oppeel.” Gent.

Ota, Tomoyuki, Hideki Ishii, Takuya Sumi, Takuya Okada, Hisashi Murakami, Susumu Suzuki, Kenji Kada, Naoya Tsuboi, and Toyoaki Murohara. 2014. "Impact of Coronary Stent Designs on Acute Stent Recoil." *Journal of Cardiology* 64 (5): 347–52. https://doi.org/10.1016/j.jjcc.2014.02.013.

Pache, Jürgen, Adnan Kastrati, Julinda Mehilli, Helmut Schühlen, Franz Dotzer, Jörg Hausleiter, Martin Fleckenstein, et al. 2003. "Intracoronary Stenting and Angiographic Results: Strut Thickness Effect on Restenosis Outcome (ISAR-STEREO-2) Trial." *Journal of the American College of Cardiology* 41 (8): 1283–88. https://doi.org/10.1016/j.solmat.2014.03.046.

Padmanabhan, Jagannath, Emily R Kinser, Mark A Stalter, Christopher Duncan-lewis, Jenna L Balestrini, Andrew J Sawyer, Jan Schroers, and Themis R Kyriakides. 2014. "Engineering Cellular REsponse Using Nanopatterned Bulk Metallic Glass." *ACS Nano* 8 (5): 4366–75. https://doi.org/10.1021/nn501874q.

Palmaz, Julio C, Amy Benson, and Eugene A Sprague. 1999. "Influence of Surface Topography on Endothelialization of Intravascular Metallic Ate Rial '." *Journal of Vascular and Interventional Radiology* 10: 439–44.

Papautsky, Ian, and Erik T K Peterson. 2014. "Micromolding." In *Encyclopedia of Microfluidics and Nanofluidics*, 1–17. https://doi.org/10.1007/978-3-642-27758-0.

Parker, E. R., B. J. Thibeault, M. F. Aimi, M. P. Rao, and N. C. MacDonald. 2005. "Inductively Coupled Plasma Etching of Bulk Titanium for MEMS Applications." *Journal of The Electrochemical Society* 152 (10): C675–83. https://doi.org/10.1149/1.2006647.

Patel, S R, A S P Lin, H F Edelhauser, and M R Prausnitz. 2011. "Suprachoroidal Drug Delivery to the Back of the Eye Using Hollow Microneedles." *Pharmaceutical Research* 28 (1): 166–76. https://doi.org/10.1007/s11095-010-0271-y.Suprachoroidal.

Patel, Samirkumar R., Damian E. Berezovsky, Bernard E. McCarey, Vladimir Zarnitsyn, Henry F. Edelhauser, and Mark R. Prausnitz. 2012. "Targeted Administration into the Suprachoroidal Space Using a Microneedle for Drug Delivery to the Posterior Segment of the Eye." *Investigative Ophthalmology and Visual Science* 53 (8): 4433–41. https://doi.org/10.1167/iovs.12-9872.

Poncin, P., and J. Proft. 2003. "Stent Tubing : Understanding the Desired Attributes." *Medical Device Materials*, no. September: 253–59.

Puranik, Amey S., Eileen R. Dawson, and Nicholas A. Peppas. 2013. "Recent Advances in Drug Eluting Stents." *International Journal of Pharmaceutics* 441 (2): 665–79. https://doi.org/10.1016/j.ijpham.2012.10.029.

Rao, M P, M F Aimi, E R Parker, and N C Macdonald. 2004. “Single-Mask, High Aspect Ratio, 3-D Micromachining of Bulk Titanium,” 2–5.

Rein, David B., John S Wittenborn, Xinzhi Zhang, Amanda A Honeycutt, Sarah B Lesesne, and Jinan Saaddine. 2009. “Forecasting Age-Related Macular Degeneration Through the Year 2050.” *Archives of Ophthalmology* 127 (4): 533–40. https://doi.org/10.1001/archophthalmol.2009.58.

Russell, Mason W., Daniel M. Huse, Shelley Drowns, Elizabeth C. Hamel, and Stuart C. Hartz. 1998. “Direct Medical Costs of Coronary Artery Disease in the United States.” *American Journal of Cardiology* 81: 1110–15. https://doi.org/10.1016/S0002-9149(98)00136-2.

Saino, Enrica, Maria Letizia Focarete, Chiara Gualandi, Enzo Emanuele, Antonia I Cornaglia, Marcello Imbriani, and Livia Visai. 2011. “Effect of Electrospun Fiber Diameter and Alignment on Macrophage Activation and Secretion of Proinflammatory Cytokines and Chemokines.” *Biomacromolecules* 12: 1900–1911. https://doi.org/10.1021/bm200248h.

Saliterman, Steven S. 2005. “Education , BioMEMS and the Medical Microdevice Revolution.” *Expert Rev. Med. Devices* 2 (5): 515–19.

Shima, Chiharu, Hirokazu Sakaguchi, Fumi Gomi, Motohiro Kamei, Yasushi Ikuno, Yusuke Oshima, Miki Sawa, Motokazu Tsujikawa, Shunji Kusaka, and Yasuo Tano. 2008. “Complications in Patients after Intravitreal Injection of Bevacizumab.” *Acta Ophthalmologica* 86 (4): 372–76. https://doi.org/10.1111/j.1600-0420.2007.01067.x.

Shirooyeh, Mahmood, Jie Xu, and Terence G. Langdon. 2014. “Microhardness Evolution and Mechanical Characteristics of Commercial Purity Titanium Processed by High-Pressure Torsion.” *Materials Science and Engineering A* 614: 223–31. https://doi.org/10.1016/j.msea.2014.07.030.

Sidambe, Alfred T. 2014. “Biocompatibility of Advanced Manufactured Titanium Implants-A Review.” *Materials* 7 (12): 8168–88. https://doi.org/10.3390/ma7128168.

Sikka, S. K., Y. K. Vohra, and R. Chidambaram. 1982. *Omega Phase in Materials. Progress in Materials Science*. Vol. 27. https://doi.org/10.1016/0079-6425(82)90002-0.

Soque, James B, and Pamela A Weber. 2013. “ARMD With Geographic Atrophy, Peripheral Degeneration.” Retina Image Bank. 2013. https://imagebank.asrs.org/file/12356/armd-with-geographic-atrophy-peripheral-degeneration.

Sridharan, Rukmani, Andrew R Cameron, and Daniel J Kelly. 2015. "Biomaterial Based Modulation of Macrophage Polarization : A Review and Suggested Design Principles — Use Licence —." *Materials Today* 6: 313–25.

Stoeckel, Dieter, Alan Pelton, and Tom Duerig. 2003. "Self-Expanding Nitinol Stents - Material and Design Considerations."

Sun, Daming, Yiming Zheng, Tieying Yin, Chaojun Tang, Qingsong Yu, and Guixue Wang. 2014. "Coronary Drug-Eluting Stents: From Design Optimization to Newer Strategies." *Journal of Biomedical Materials Research - Part A* 102 (5): 1625–40. https://doi.org/10.1002/jbm.a.34806.

Tan, Kai Soo, Li Qian, Roy Rosado, Patrick M Flood, and Lyndon F Cooper. 2006. "The Role of Titanium Surface Topography on J774A . 1 Macrophage Inflammatory Cytokines and Nitric Oxide Production." *Biomaterials* 27: 5170–77. https://doi.org/10.1016/j.biomaterials.2006.05.002.

Tillocher, T., P. Lefaucheux, B. Boutaud, and R. Dussart. 2014. "Alternated Process for the Deep Etching of Titanium." *Journal of Micromechanics and Microengineering* 24 (7): 1–10. https://doi.org/10.1088/0960-1317/24/7/075021.

Vandrangi, Prashanthi, Shannon C. Gott, Ryan Kozaka, Victor G.J. Rodgers, and Masaru P. Rao. 2014. "Comparative Endothelial Cell Response on Topographically Patterned Titanium and Silicon Substrates with Micrometer to Sub-Micrometer Feature Sizes." *PLoS ONE* 9 (10): 1–13. https://doi.org/10.1371/journal.pone.0111465.

Vandrangi, Prashanthi, Shannon Gott, Ryan Kozaka, Masaru P Rao, and Victor G J Rodgers. 2013. "Endothelial Behavior and Signaling on Micro and Submicro-Patterned Titanium." *Circulation*, no. January 2013: 128:A18077. http://circ.ahajournals.org/cgi/content/meeting_abstract/128/22_MeetingAbstracts/A18077.

Verschuren, Jeffrey J. W. 2013. *Genetic and Pharmacogenetic Determinants of Cardiovascular Disease*.

Wang, Chuan Ting, Alan G. Fox, and Terence G. Langdon. 2014. "Microstructural Evolution in Ultrafine-Grained Titanium Processed by High-Pressure Torsion under Different Pressures." *Journal of Materials Science* 49 (19): 6558–64. https://doi.org/10.1007/s10853-014-8248-6.

Wang, Chuan Ting, Nong Gao, Mark G. Gee, Robert J.K. Wood, and Terence G. Langdon. 2013. “Processing of an Ultrafine-Grained Titanium by High-Pressure Torsion: An Evaluation of the Wear Properties with and without a TiN Coating.” *Journal of the Mechanical Behavior of Biomedical Materials* 17: 166–75. https://doi.org/10.1016/j.jmbbm.2012.08.018.

WHO. 2018. “Priority Eye Diseases.” World Health Organization. World Health Organization. 2018. https://www.who.int/blindness/causes/priority/en/index7.html.

Wijngaarden, Peter van, Douglas J Coster, and Keryn A Williams. 2005. “Inhibitors of Ocular Neovascularization: Promises and Potential Problems.” *Journal of the Americal Medical Association* 293 (12): 1509–13. https://doi.org/10.1001/jama.293.12.1509.

Wilson, ME, and AW Scott. 2013. “How to Give Intravitreal Injections.” *EyeNet*, 45–47.

Witte, Frank. 2015. “Reprint of : The History of Biodegradable Magnesium Implants : A Review Q.” *Acta Biomaterialia* 23: S28–40. https://doi.org/10.1016/j.actbio.2015.07.017.

Wong, Wan Ling, Xinyi Su, Xiang Li, Chui Ming G. Cheung, Ronald Klein, Ching Yu Cheng, and Tien Yin Wong. 2014. “Global Prevalence of Age-Related Macular Degeneration and Disease Burden Projection for 2020 and 2040: A Systematic Review and Meta-Analysis.” *The Lancet Global Health* 2: e106–16. https://doi.org/10.1016/S2214-109X(13)70145-1.

Woo, Bryan W.K., Shannon C. Gott, Ryan A. Peck, Dong Yan, Mathias W. Rommelfanger, and Masaru P. Rao. 2017. “Ultrahigh Resolution Titanium Deep Reactive Ion Etching.” *ACS Applied Materials and Interfaces* 9: 20161–68. https://doi.org/10.1021/acsami.6b16518.

Wynn, Thomas A, Ajay Chawla, and Jeffrey W Pollard. 2013. “Macrophage Biology in Development , Homeostasis and Disease.” *Nature* 496 (7446): 445–55. https://doi.org/10.1038/nature12034.

Yang, J.H., K. Byeon, H.-C. Gwon, J.E. Park, and Y.B. Song. 2012. “Identification of Vulnerable Plaque in a Stented Coronary Segment 17 Years after Implantation Using Optical Coherence Tomography.” *Yonsei Medical Journal* 53 (2): 450–53. http://www.eymj.org/Synapse/Data/PDFData/0069YMJ/ymj-53-450.pdf%5Cnhttp://ovidsp.ovid.com/ovidweb.cgi?T=JS&PAGE=reference&D=emed10&NEWS=N&AN=2012096300.

Yim, Evelyn K F, Eric M Darling, Karina Kulangara, Farshid Guilak, and Kam W Leong. 2010. “Biomaterials Nanotopography-Induced Changes in Focal Adhesions , Cytoskeletal Organization , and Mechanical Properties of Human Mesenchymal Stem Cells.” *Biomaterials* 31 (6): 1299–1306. https://doi.org/10.1016/j.biomaterials.2009.10.037.

Yorston, David. 2014. “Intravitreal Injection Technique.” *Community Eye Health Journal* 27 (87): 47.

Zhao, Gang, Qiong Shu, Yao Tian, Yiming Zhang, and Jing Chen. 2009. “Wafer Level Bulk Titanium ICP Etching Using SU8 as an Etching Mask.” *Journal of Micromechanics and Microengineering* 19 (9). https://doi.org/10.1088/0960-1317/19/9/095006.

Zhilyaev, Alexander P., and Terence G. Langdon. 2008. “Using High-Pressure Torsion for Metal Processing: Fundamentals and Applications.” *Progress in Materials Science* 53 (6): 893–979. https://doi.org/10.1016/j.pmatsci.2008.03.002.

APPENDIX

Appendix A. Si Imprint Master Fabrication

(Performed at UCSB)

1. Use carbon tipped tweezers to remove a SSP Si wafer from its cassette, and place it polished side up, into an appropriately sized crystallizing dish.
2. Sonicate the wafer for 3 minutes in acetone and then another 3 minutes in isopropyl alcohol on the highest frequency and intensity settings.
   a. Ensure there is enough solvents to prevent evaporation and do not let the sample surface dry out at any point.
3. Thoroughly rinse the wafer in deionized water to remove any remaining solvents, then place the wafer onto a non-shedding wipe, and blow dry with a nitrogen gun.
4. Transport the wafer in a clean wafer carrier to the asher tool (Technics/PE-IIA) and run a 1-minute O_2 plasma clean with 100 W substrate power and 300 mT chamber pressure.
   a. Alternatively, you can clean the wafer using a 2-minute O_2 plasma clean at 350 °C in the Gasonics/Aura 2000-LL Downstream Asher tool.
5. Transport the wafer in a clean wafer carrier to the acid benches and don proper personal protective equipment to work with hydrofluoric acid.
   a. This usually consists of appropriate acid gloves, apron, and face shield in addition to standard personal protective equipment.
6. Pour enough hydrofluoric acid into a plastic dish to cover a wafer.

a. Remember not to use a glass dish since hydrofluoric acid will react with glass.

7. Use plastic tweezers to place the wafer into the hydrofluoric acid and let it sit for 1 minute. This removes all remaining contaminants and has been shown to reduce surface roughness.
8. Use plastic tweezers to carefully remove the wafer from the hydrofluoric acid, then thoroughly rinse with deionized water, and dry with a nitrogen gun.
9. Transport the wafer in a clean wafer carrier to the spin bench and use solvents to clean an appropriately sized spinner chuck.
10. Use tweezers to place the wafer onto the spinner chuck, pull vacuum, and use a nitrogen gun to blow off any particles.
11. Use a filter and syringe to pipette AR2 resist onto the wafer and use a separate clean pipette to remove any bubbles.
12. Spin the AR2 resist at 3000 rpm for 30 seconds. This should create a resist layer that is ~680-715 angstroms thick.
13. Carefully pick up the wafer using tweezers, and while holding it, use a swab with acetone to remove any AR2 resist that may be on the backside.
    a. Adjust tweezer positions as necessary to ensure all AR2 resist is removed. This is very important due to the sensitivity of the stepper lithography.
14. Bake the wafer at 220 °C for 1 minute on a hotplate.
    a. Make sure the wafer is placed on the center of the hotplate for even heating and be prepared with tweezers to remove it after exactly 1 minute

since the DUV coatings are extremely heat sensitive and even a few seconds difference can lead to poorer results.

15. Place the wafer onto one non-shedding cleanroom wipe and let it cool for 3 minutes.
    a. Using more than one wipe will alter the cooling rate and negatively affect the lithography patterning.
16. Place the wafer back onto the vacuum chuck and use a nitrogen gun to remove any particles that may have settled on the surface.
17. Use a syringe and filter to pipette UV210-0.3 resist onto the wafer.
18. Immediately spin the UV210-0.3 resist at 5000 rpm for 30 seconds.
    a. Do not let it sit, or the layer thickness may be incorrect.
19. Bake the wafer on a hotplate at 130 °C for 1 minute.
20. Place the water onto one non-shedding cleanroom wipe and let it cool for 1 minute.
21. Carefully pick up the wafer using tweezers, and while holding it, use a swab with EBR 100 to remove any resist or particles on the backside.

Stepper Exposure and Development

22. Use the ASML PAS 5500/300 tool to expose the resist using 22 MJ/cm^2 with -0.1 offset. Use numerical aperture: 0.63, σ_{outer}: 0.8, and σ_{inner}: 0.5.
23. Perform a post-exposure bake on the wafer on a hotplate set at 130 °C for 90 seconds.

24. Place the water onto one non-shedding cleanroom wipe and let it cool for 1 minute.
25. Pour AZ 300 MIF developer into a crystallizing dish and submerge the wafer in it for 45 seconds. Do not agitate.
26. Remove the wafer from the developer and gently rinse with deionized water in such a way that the water stream does not flow directly onto the features.
27. Dry the wafer with a nitrogen gun at a pressure less than 20 psi.
28. Check feature definition under DUV microscope and add more development time if needed.

Si Imprint Master Etching

29. Carefully remove the outer resist between the patterns and the wafer edges with a swab and acetone to improve contact and filling between the imprint master and the substrate in thermal nanoimprint lithography.
    a. Note that acetone fumes can affect the nearby resist, so be careful not to swab too close to the features.
    b. Use a razor blade to remove any photoresist that is close to the patterned features.
30. Once the outer resist has been removed, transport the patterned Si wafer in a clean wafer holder to RIE #5 to remove the excess anti-reflective coating.
31. Load a clean Si wafer and run a 10-minute O_2 clean in the RIE #5 tool in manual mode.

32. Place the patterned Si wafer, resist side up, onto another Si carrier wafer. Align the flats and place the stack into the RIE #5 loadlock.
    a. No oil or other adhesives are necessary, but proper alignment is very important.
33. Etch off the residual anti-reflective coating with 20 sccm O_2, 10 mT pressure, and 100W of power for 30 seconds in manual mode.
34. Transport the patterned wafer in a clean wafer carrier to the Si ICP RIE tool (Plasmatherm 770 SLR) to transfer the pattern into the underlying Si substrate.
35. Load a clean Si wafer and run a 30-minute O_2 clean in the Si ICP RIE tool in manual mode.
36. Load a clean Si wafer and run a 1-minute Si etch season in the Si ICP RIE using recipe “cao_n_1” which consists of 19 mT chamber pressure, 825 ICP source power, 15 W substrate power, 54 sccm C_4F_8, 26 sccm SF_6, 20 sccm Ar, and 10 °C lower electrode temperature.
37. Load the patterned Si wafer and run a 2 minute and 55 second Si etch in the Si ICP RIE using the “cao_n_1” recipe as listed in the previous step to create features that are ~250 nm in height.
    a. The patterned wafer can be processed directly without needing a carrier wafer.

<u>FDTS Layer Deposition</u>

38. Transport the patterned wafer in a clean wafer carrier to the acid benches.

39. Mix a 3:1 solution of sulfuric acid to hydrogen peroxide (Piranha) in a glass dish on a hotplate that is set to 80 °C. The solution should bubble, so add more hydrogen peroxide and/or time as needed.
40. Use metal tweezers to place the patterned Si wafer into the Piranha and let it sit for 20 minutes.
    a. If floating occurs, use tweezers to encourage continuous submersion.
41. Use metal tweezers to remove the patterned wafer from the Piranha, thoroughly rinse with deionized water, and then blow dry both sides with a nitrogen gun.
42. Transport the wafer in a clean wafer carrier to the asher tool (Technics/PE-IIA) and run a 3-minute O_2 plasma clean with 100 W substrate power and 300 mT chamber pressure.
43. Repeat steps 39-41, cleaning a second time with Piranha and O_2 ashing.
44. While the second O_2 ashing step is running, prepare to run the FDTS coating process on the MVD tool with process conditions consisting of 23 °C chamber temperature and a 600 second reaction time of the H_2O and FDTS.
45. Remove the Si wafer from the O_2 ashing chamber, immediately place it within the MVD chamber, and pump it down.
    a. This step is extremely sensitive and should be performed as precisely and as quickly as possible.
46. Use the MVD tool to deposit the layer of FDTS according to the previously mentioned parameters.

47. Use tweezers to remove the Si wafer from the MVD chamber and bake it on a hotplate at 140 °C for 2 minutes.
48. Si Imprint Master Fabrication is complete.

Appendix B. Ti Surface Grating Fabrication

(Performed at UCSB)

1. Use sharp scissors to cut 200 µm Ti foil into 2 ¾” x 2 ¾” squares. Trim the corners so that the foils will easily fit onto a 100 mm Si wafer.
2. Use tweezers or a razor blade to carefully peel off the protective surface film, making sure not to damage the underlying Ti surface while doing so.
3. Place a foil into an appropriately sized crystalizing dish, polished-side up for cleaning.
   a. Only clean one foil in a dish at a time, as multiple foils will scratch each other.
4. Sonicate the foil for 3 minutes in acetone and then another 3 minutes in isopropyl alcohol on the highest frequency and intensity settings.
   a. Ensure there is enough solvents to prevent evaporation and do not let the sample surface dry out at any point.
5. Thoroughly rinse the foil in deionized water to remove any remaining solvents, then place the foil onto a non-shedding wipe, and blow dry with a nitrogen gun.
6. Transport the foil to the ICP PECVD (Unaxis VLR) and deposit 200 nm of SiO_2 onto the polished side of the Ti foil using the ICP PECVD.
   a. The following parameters used in this study: 15 mT chamber pressure, 400 W ICP source power, 5 W substrate power, 5.9 sccm of 100% SiH_4, 20 sccm Ar, 10 sccm O_2, and 100 °C lower electrode temperature.

7. Thoroughly clean a hotplate with a razor blade and EBR 100 and bake the foil on at 110-135 °C for 5 minutes to thoroughly dehydrate the surface.
8. Transport the foil to the asher tool (Technics/PE-IIA) and run a 1-minute O_2 plasma clean with 100 W substrate power and 300 mT chamber pressure.
9. Transport the foil in to the spin bench, and use solvents to clean an appropriately sized spinner chuck.
10. Use tweezers to place the foil onto the spinner chuck, pull vacuum, and use a nitrogen gun to blow off any particles.
11. Use a filter and syringe to pipette MRI 7020 resist onto the foil.
12. Use a separate clean pipette to remove any bubbles.
13. Spin the MRI 7020 resist on the foil at 2000 RPM for 30 seconds to create a layer that is ~250 nm thick.
14. Remove the foil from the spinner chuck and bake on a hotplate at 140 °C for 3 minutes.
    a. It is normal for thin Ti foil to not lay flat on the hotplate.

Si Imprint Master Preparation

15. Sonicate the desired Si imprint master for 3 minutes in acetone and then another 3 minutes in isopropyl alcohol on the highest frequency and intensity settings.
    a. Ensure there is enough solvents to prevent evaporation and do not let the sample surface dry out at any point.

16. Thoroughly rinse the Si imprint master in deionized water to remove any remaining solvents, then place the imprint master onto a non-shedding wipe, and dry with a nitrogen gun at a pressure less than 20 psi.
17. Bake the imprint master on a hotplate at 115 °C for 5 minutes to remove any residual water.
    a. NEVER use O_2 plasma to clean the imprint master because it removes the hydrophobic FDTS monolayer on the Si surface.

Thermal Nanoimprint Lithography

18. Make sure that there is sufficient gas within the gas tank(s) and the lines are open.
    a. If unsure, verify with the appropriate cleanroom technician(s).
19. Wipe the silicone bladders clean with isopropanol.
20. Mount silicone bladders into the thermal nanoimprint lithography tool (Nanonex) using the magnets.
    a. Make sure that the bladders are pulled tight and there are no wrinkles.
21. Use a nitrogen gun to remove any particles from the Si imprint master and Ti foil surfaces.
22. Immediately center and place the Ti foil, resist side down, over the Si imprint master pattern.
23. Center the Si imprint master/Ti stack (with Si imprint master on the bottom) on the lower silicone bladder in the Nanonex tool.
24. Make sure all the springs are in place or put in replacement springs.

25. Place the upper silicone bladder into place and gently slide the drawer closed, making sure not to jolt the drawer into the latch.
    a. Slightly lifting the handle near the end as you slide it may help.
26. Run the imprinting process with the following parameters:
    a. 2 min pump down
    b. 2 min 140°C
    c. 10 min 140°C/500 psi
    d. 1 min 120°C/500psi
    e. 1 min 100°C/500psi
    f. 1 min 80°C/500psi
    g. 1 min 60°C/500psi
    h. 1 min 55°C/500psi and vent
27. Immediately remove the samples and peel them in the direction of the grooved patterns, starting from the Si wafer flat.
    a. Be diligent to pull the Ti foil off the Si imprint master only in a direction that is normal to the Si wafer surface to prevent damaging the imprint master.
    b. IMPORTANT: After every 10-15 imprints, the Si imprint master needs a new coating of FDTS with the MVD tool.

Pattern Transfer

28. Apply double-sided thermally conductive tape to the middle of a 6” Si carrier wafer.
    a. Use a razor blade while advancing the tape to ensure no air pockets are produced.
    b. Place additional strips of tape as necessary to create an area slightly larger than 2 ¾” x 2 ¾” that has no gap or overlap.
29. Carefully remove the top-side protective film from the double-sided tape to expose the adhesive.
30. Center the Ti foil, pattern side up, over the tape and use tweezers to firmly press it down into the tape.
    a. Start from one edge and work to the far edge to help prevent air pockets.
31. Use a razor blade to trim off the excess tape around the Ti foil sample, and then use a wipe and nitrogen to remove any particles this may have left behind, being careful not to deposit any onto the patterned surface.
32. Carefully transport the Si carrier wafer mounted Ti foil to the ICP#1 tool (Panasonic E620-R&D).
33. Run a 10-minute O_2 clean on a clean 6” Si wafer on the ICP#1 tool.
    a. The parameters consist of: 37.5 mT chamber pressure, 900 W ICP source power, 100 W substrate power, and 40 sccm O_2.
34. While the O_2 clean is running, place a clean 4” Si wafer onto a spinner chuck, pull vacuum, and blow off any particles using a nitrogen gun.

35. Pipette MRI-7020 resist onto the clean 4” Si wafer and spin it at 2000 rpm for 30 seconds.
36. Mount the MRI-7020 resist coated 4” Si wafer onto the center of 6” Si carrier wafer using Santovac 5P-Ultra pump oil.
37. Load the 6” Si carrier wafer containing the 4” MRI-7020 coated wafer and run a 3 minute and 30 second residual resist etch season.
    a. The parameters consist of: 3.75 mT chamber pressure, 75 W ICP source power, 65 W substrate power, and 49 sccm O_2.
38. Load the 6” carrier wafer containing the mounted Ti foil and run a 1 minute and 55 second residual resist etch with parameters consistent with those previously mentioned.
    a. This removes the remaining resist in the bottom of the grating trenches.
39. Load a clean 6” Si wafer and run a 10-minute O_2 clean.
40. Load a clean 6” Si wafer and run a 1 minute and 55 second CHF_3/CF_4 SiO_2 etch season.
    a. The parameters consist of: 3.75 mT chamber pressure, 900 W ICP source power, 50 W substrate power, 20 sccm CHF_3, and 20 sccm CF_4.
41. Load the 6” Si carrier wafer containing the mounted Ti gratings and run a 1 minute and 55 second CHF_3/CF_4 SiO_2 etch to transfer the pattern into the SiO_2 hard mask using the aforementioned processing parameters.
42. Load a clean 6” Si wafer and run a 5-minute O_2 clean.

Dicing

43. Install a spinner chuck that is appropriately sized for a 6” Si wafer, mount the 6” Si carrier wafer containing the Ti grating foil, pull vacuum, and use a nitrogen gun to blow off any particles.
44. Pipette or pour SPR220-7.0 resist onto the Ti grating foil so that it is completely covered.
    a. The rest of the carrier wafer does not need to be covered.
45. Spin the SPR 220-7.0 resist on the Ti grating foil at 2000 rpm for 30 seconds.
    a. This layer is used to protect the substrate surfaces from oil and other damage during dicing.
46. Bake the entire 6” carrier wafer containing the Ti grating foil on a hotplate at 115°C for 1 minute.
47. Pack the now coated 6” Si carrier wafer containing the Ti grating foil and proper dicing materials/tools and go to the dicing saw (ADT 7100).
48. Mount the 6” Si carrier wafer containing the Ti grating foil onto the dicing saw chuck using the single-sided dicing saw tape and remove the excess tape.
49. Load the dicing saw chuck into the dicing saw.
50. Do a blade change and install a 2.050-8C-54RU blade with an appropriately sized hub.
    a. The hubs used are usually 48-52 mm.
51. Follow the directions posted on the wall to dice the Ti foil either manually or with the appropriate recipe.

a. Make sure to take the stack (Ti, tape, Si) thickness into account when inputting cutting depth.

52. Carefully remove the diced Ti grating sample(s) from the diced Si wafer, dispose of the excess Si wafer and tape in the sharps container, and return to the cleanroom.
53. Sonicate the Ti grating sample for 3 minutes in acetone on the highest frequency and intensity settings, and then use swabs to ensure complete removal of any residual protective SPR 220-7.0 that may be on the surface.
    a. Ensure there is enough solvents to prevent evaporation and do not let the sample surface dry out at any point.
    b. Do not press hard while swabbing or the gratings may be damaged.
54. Sonicate the Ti grating sample for another 3 minutes in isopropyl alcohol on the highest frequency and intensity settings.
55. Thoroughly rinse the Ti grating sample with deionized water to remove any remaining solvents, then place the Ti grating sample onto a non-shedding wipe, and dry with a nitrogen gun at a pressure less than 20 psi.
56. Bake the Ti grating sample on a hotplate at 110-135 °C for 5 minutes to dehydrate the surface and adhesive tape and return to the ICP #1 tool.

Ti Foil Etch Steps

57. Load a clean 6” Si wafer and run a 10-minute O_2 clean on the ICP #1 tool.

58. Mount a Ti grating sample onto a single 6” Si carrier using Santovac 5P-Ultra pump oil.
59. Load the 6” Si carrier wafer containing the Ti grating sample and run a 1-minute sub-micron Ti Etch with varying parameters for optimization.
    a. The baseline parameters consist of: 3.75 mT chamber pressure, 400 W ICP source power, 100 W substrate power, 40 sccm Cl_2, and 4 sccm O_2.
60. Load a clean 6” Si wafer and run a 5-minute CF_4/O_2 clean.
    a. The parameters consist of: 37.5 mT chamber pressure, 700 W ICP source power, 100 W substrate power, 50 sccm CF_4, and 40 sccm O_2.
61. Gently use the handle of a swab to push/slide the Ti grating sample off the 6” Si carrier wafer.
62. Carefully pick up the Ti grating sample and use a swab and acetone to remove any residual 5P-Ultra pump oil that is on the backside.
    a. Let them fully dry before storing as acetone will melt normal sample holders.
63. Sonicate the Ti grating sample for 3 minutes in acetone.
    a. Ensure there is enough solvents to prevent evaporation and do not let the sample surface dry out at any point.
64. Sonicate the Ti grating sample for another 3 minutes in isopropyl alcohol.
65. Thoroughly rinse the Ti grating sample with deionized water to remove any remaining solvents, then place the Ti grating sample onto a non-shedding wipe, and dry with a nitrogen gun at a pressure less than 20 psi.

66. Bake on a hotplate for 5 minutes at a set temperature of 105 °C to remove any residual water, and store in a sample holder using pieces of cleanroom wipes as padding to prevent damage during transportation.
67. Ti grating sample fabrication is complete.

Appendix C. Ti Gratings Characterization

(Performed at UCR)

A standard solvent clean should be performed prior to characterization of the Ti grating samples to remove any particulate or residual chemicals that may be on the surface as their presence can jeopardize the accuracy and precision of the subsequent results.

1. Sonicate a sample for 3 minutes in acetone on the highest frequency and intensity settings.
    a. Ensure there is enough solvents to prevent evaporation and do not let the sample surface dry out at any point.
2. Sonicate for another 3 minutes in isopropyl alcohol on the highest frequency and intensity settings.
3. Thoroughly rinse the sample in deionized water to remove any remaining solvents, then place the wafer onto a non-shedding wipe, and blow dry with a nitrogen gun.

Surface Profilometry (Veeco Dektak 8 located in CNSE)

1. Make sure that there are no particles or residue on the backside of the grating sample to be tested.
    a. If necessary, use a swab and acetone to clean the backside, taking care not to damage the gratings on the front.
2. Open the Dektak32 software by double-clicking on the icon.

3. Open the panel door and place the grating sample near the center stage, underneath the stylus.
4. Press the "Tower down to null position—stylus up" button.
    a. This brings the stylus down to the substrate surface without damaging the surface and allows for additional positioning.
5. Close the panel door and increase the brightness until you can clearly see the sample surface on the monitor.
6. Press the "Scan routines" button and create a scan routine.
    a. The surface profilometry scans in this project used the following parameters: scan length of 300 μm, scan duration of 10 seconds, 5 mg stylus force, 65 kA measurement range, standard scan type, and a Hills & Valleys Profile.
7. Press the "Sample positioning window" button and move to an open etched area that is adjacent to a grating area.
    a. Recall that the stylus is pulled from left to right on the monitor so the positioning should be adjusted as necessary to ensure the scan will not leave the etched area and record inaccurate results.
8. Initiate the programmed scan at this position using "Scan Here" under the scan menu.
9. Once complete, save and export the data for analysis.
10. Repeat steps #6-8, at various locations across the sample to ensure consistency and accuracy.

    a. In this study, scans were repeated for a total of 13 scans per sample.

11. Press the "Tower up" button to move the tower and stylus back to its original raised position.
12. Open the panel door and retrieve the sample.
13. Decrease the lighting back to off and close the software.
14. Close the panel door.

Focused Ion Beam Milling (Quanta 3D FIB/SEM located in CFAMM)

1. Use carbon paint to attach a grating sample to a sample stub.
2. Initialize the system, vent the chamber (making sure to open and close the nitrogen valve), load the sample, and pump it down.
3. Rotate the sample as necessary so that the gratings are aligned vertically on the screen.
4. Focus the tool and ensure the wobble and stagnation are minimized as much as possible.
5. Find a desired grating site, and begin the stage tilting process for milling.
6. Focus again if needed, but adjustments should be minimal if the tool is working properly.
7. Insert a carbon source, let it heat up to proper temperature, and deposit a layer of protective carbon that is ~5 x 1 x 1 (L x W x H) µm in dimension such that it is perpendicular across the grating surface.
8. Withdraw the carbon source and insert the FIB milling source.

9. Begin milling a "window" into the 200 nm grating surface.
    a. Three passes that were ~ 5 x 5 x 1.25 (L x W x H) μm in dimension were used in this study. Care was taken to reduce the voltage and cut into the carbon more with each pass to prevent re-deposition and create a nicer finish.
10. Once FIB milling is complete, retract the FIB needle and return the stage to its home position.
11. Vent the chamber (making sure to open and close the nitrogen valve), remove the sample, and then pump it down before exiting the UI software.
12. Perform a solvent clean on the Ti grating sample prior to characterization to remove any remaining carbon paint.
    a. Sonicate a sample for 3 minutes in acetone and then another 3 minutes in isopropyl alcohol on the highest frequency and intensity settings. Ensure there is enough solvents to prevent evaporation and do not let the sample surface dry out at any point.
    b. Thoroughly rinse the sample in deionized water to remove any remaining solvents, then place the wafer onto a non-shedding wipe, and blow dry with a nitrogen gun.

<u>Scanning Electron Microscopy (LEO Supra 55 located in CNSE)</u>

1. Take the grating samples to the LEO Supra 55 SEM and use the clips to attach a Ti grating sample to the sample holder.

2. Initialize the system, vent the chamber, load the sample, and pump it down.
3. For surface roughness images, navigate to an etched area next to the gratings and obtain a high-resolution micrograph.
    a. The following parameters were used in this study: 5 kV accelerating voltage, 12.0 mm working distance, 3750 x magnification, and SE2 detection mode.
4. Repeat this several times at different locations on the sample to make sure it is representative of the sample surface and export the micrographs for analysis.
5. For cross-sectional images, navigate to the FIB milled "window" (cross-sectional area), tilt the stage to get a good perspective, and obtain a high-resolution micrograph.
    a. The following parameters were used in this study: 5 kV accelerating voltage, 12.6 mm working distance, 60000 x magnification, and inlens detection mode.
6. Repeat this for each FIB milled "window" and export the micrographs for analysis.

Software Analysis

1. The surface roughness data was imported and analyzed using Excel (Microsoft).
    a. The root mean square (RMS) values were calculated for each individual scan on a sample and then all thirteen RMS values were averaged to determine the surface roughness.

2. The semi-quantitative analysis of the cross-sectional area micrographs was performed using ImageJ.
    a. One micrograph was imported at a time and the scale, pixels/unit length, was set based upon the image's included scale bar annotations.
    b. Once the scale was set, lines were drawn to measure the desired features and measurements were calculated.

Appendix D. Microneedle Fabrication

(Performed at NCSU and UCR)

High-Pressure Torsion Processing

1. Purchase a commercially pure, grade 1 Ti plate that is ~1.2-1.5 mm thick (Fine Metals Corporation).
    a. The specified thickness is necessary for High-Pressure Torsion processing since the 1 mm internal anvil spacing should be exceeded for proper grip and hydrostatic pressure.
2. Use wire electrical discharge machining to cut out circular samples that are 10 mm in diameter.
3. Remove re-deposited brass using rough sand paper.
    a. 400 grit silicon carbide (SiC) sand paper was used in this study.
4. Send the samples to North Carolina State University for HPT processing.
    a. Processing parameters vary, but the main parameters used in this work were 1 GPa of pressure, 4 turns at a speed of 1 rpm, quasi-constrained anvils, and ambient temperature.

Grinding and Polishing

5. When the samples have been processed and returned, use wire cutters to remove excessive flange which may negatively affect planarity during casting.

6. Use 1” diameter casting cups to cast the sample(s) in acrylic resin using a 2:1 mixture of QuickCure acrylic powder to methyl methacrylate liquid (Allied High Tech).
    a. Use a popsicle stick to position the sample in the middle and prevent it from moving and/or lifting as resin is poured in.
7. Allow the acrylic resin to set and completely harden.
8. Release the now acrylic-embedded samples from the casting cups.
    a. Sometimes a screwdriver can be helpful for this step.
9. Thoroughly wash hands with soap and water to prepare for sample handling.
10. Polish up to 6 acrylic-embedded samples simultaneously using the autopolisher and polishing head (PACE Technologies NANO 1000T with FEMTO 1100 polishing head). If less than 6 samples are being polished at once, include blank acrylic samples to balance the polishing head. The polishing steps are as follows:

Step	Description	Grit	Pressure	RPM (h+b)	Pad	Time Increments
1	Planarity Polish	400 SiC	45 psi	200 Complementary	SiC	1- to 2- minutes
2	Preparation	Rinse off samples and prepare for next step				
3	Rough Polish	6 µm diamond	50 psi	60+120 Contra	Texpan	3- to 5- minutes
4	Preparation	Rinse off samples and prepare for next step				
5	Fine Polish	1 µm diamond	50 psi	60+120 Contra	Gold	3- to 5- minutes
6	If doing Step 7	Rinse off samples and prepare for next step				
7	Final Polish (Optional)	200 nm colloidal Silica	45 psi	60+120 Contra	Texpan	5- minutes
8	Finishing up	Rinse off samples and clean up				

a. Water flow should be continuous when using silicon carbide in step 1 and turned off when using slurry/colloidal silica (steps 3, 5, and 7).
b. Polishing with diamond slurry and/or colloidal silica requires refreshing every 1- to 1.5- minutes (steps 3, 5, and 7).
c. Final sample thickness should be ~50 µm after grinding and polishing.

11. Release the Ti samples from the acrylic resin by sonicating in acetone.
    a. Use a capped jar and check periodically to ensure that there is enough acetone to prevent the acrylic from drying out. Remove acrylic resin chunks and add acetone as needed.

Substrate preparation and patterning

12. Once the Ti sample(s) have been recovered, take them down to the cleanroom.
13. Sonicate the Ti sample(s) for 3 minutes in acetone and then another 3 minutes in isopropyl alcohol.
    a. Ensure there is enough solvents to prevent evaporation and do not let the sample surface dry out at any point.
14. Thoroughly rinse the Ti sample(s) in deionized water to remove any remaining solvents, then place the sample(s) onto a non-shedding wipe and blow dry with nitrogen.
15. Bake the Ti sample(s) on a hotplate at 110-135 °C for 5 minutes to evaporate any remaining water.
16. Run a 10-minute pre-clean process on the Unaxis 790 tool.

    a. The recipe name is "cleanbww.prc," and the parameters consist of 900 mTorr of pressure, 400 W power, 45 °C heat exchanger, 250 °C cathode heat, 90 sccm of SF_6, and 40 sccm N_2O.

17. Vent the chamber, load the Ti sample(s) into the center of the chamber, and pull vacuum once more.
18. Use recipe "ox25-bww.prc" to deposit 3.2 µm of SiO_2 using the Unaxis 790 tool operating with 900 mTorr of pressure, 25 W power, 45 °C heat exchanger, 250 °C cathode heat, 400 sccm SiH_4, and 900 sccm N_2O.
    a. The recipe, "ox25-bww.prc," deposits at a rate of ~40 nm/minute.
    b. The standard rule of thumb is that no deposition step should be run for more than 60 minutes at a time. As a result, alternating deposition and clean steps will be needed.
19. Remove the Ti sample(s) and let them cool on a cleanroom wipe.
20. Run a final clean on the Unaxis 790 tool using the aforementioned, "cleanbww.prc" recipe and close the software when finished.
21. Sonicate the Ti sample(s) for 3 minutes in acetone and then another 3 minutes in isopropyl alcohol.
    a. Ensure there is enough solvents to prevent evaporation and do not let the sample surface dry out at any point.
22. Thoroughly rinse the Ti sample(s) in deionized water to remove any remaining solvents, then place the sample(s) onto a non-shedding wipe and blow dry with nitrogen.

23. Bake the Ti sample(s) on a hotplate at 110-135 °C for 5 minutes and set them aside in a covered sample holder.
24. Use a diamond scribe to scribe Si wafers and create ~0.5” x 0.5” Si chips for mounting.
25. Blow any Si particles off the Si chips with a nitrogen gun.
26. Use scissors and a razor blade to attach double-sided, thermally conductive tape to each Si chip. Use the razor blade to advance the tape from one end to the other and prevent air pockets from forming.
27. Carefully remove the top-side layer of the protective film, and mount one Ti sample per Si chip, pressing down firmly with the tweezer edge.
    a. Use a razor blade to remove any excess tape.
    b. Henceforth, “Ti sample(s)” refers to this Ti/tape/Si chip stack.
28. Use solvents to clean an appropriately sized spinner chuck.
29. Place a mounted sample onto the spinner chuck, pull vacuum, and blow off any particles that may be on the surface with a nitrogen gun.
30. Use a clean pipette to place a layer of hexamethyldisilazane (HMDS) onto the Ti sample surface and let sit for 30 seconds.
31. Spin the HMDS at 3000 RPM for 30 seconds.
32. Wait 1 minute to allow the HMDS vapors to dissipate.
33. Use a clean pipette to place a layer of AZ nLoF 2070 photoresist onto the Ti sample surface and use another clean pipette to remove any bubbles that are present.

34. Spin the AZ nLoF 2070 resist at 2500 rpm for 30 seconds. This should create a layer that is ~7.5 μm thick.
35. Let the resist settle for 5 minutes.
36. Carefully transfer the Ti sample(s) to a hotplate and soft bake at 100 °C for 8 minutes.
37. Use tweezers to pick up the Ti sample(s) and check the backside of the substrate for particles or resist residue. If any is present, use a swab and acetone to carefully remove it.
38. Transport the Ti sample(s) to the Suss MA-6 photolithography tool.
39. Align a Ti sample with the desired mask pattern so that it will be exposed near the center of the MA-6 chuck.
    a. Failure to properly position the sample can lead to variations in sample exposure and uneven patterning.
40. Expose the Ti sample using hard exposure, contact WEC type, 0.4 vacuum seal, 0.4 WEC pressure, 60 μm allowable gap, and 4 second HC wait time.
    a. The standard AZ nLoF 2070 photospeed is 180 mJ/cm^2, so adjust time as necessary depending on the lamp power, intensity, and photoresist age.
41. Remove the Ti sample(s) from the MA-6 tool and let it sit for 5 minutes to allow resist reactions to finish occurring.
42. Place the Ti sample(s) onto a hotplate and post-exposure bake at 110 °C for 1 minute.

43. Pour AZ 300 MIF developer into a large beaker and fill another large beaker with deionized water.
44. Place the Ti sample(s) into a developer basket and submerge in the AZ 300 MIF developer for ~1 minute. Continuously agitate to ensure proper development.
45. Remove the Ti sample from the AZ 300 MIF developer, immediately submerge it in the deionized water, and transport it to the sink area.
46. Rinse thoroughly with deionized water and dry with a nitrogen gun that is set below 20 psi.
47. Check the Ti sample(s) under optical microscope for feature definition and add additional development time as necessary.
48. Place the Ti sample(s) onto a hotplate and hard bake at 115 °C for 2 minutes.
49. Place the Ti sample(s) into a covered sample holder, gather necessary etching supplies, and go to the cleanroom in the Materials Science and Engineering Building.

<u>Pattern transfer</u>

50. Make sure the Si etching tool (Oxford Plasmalab 100) is in cryogenic mode, verify that there is enough liquid nitrogen in the tank, and open the blue valve on the liquid nitrogen.
51. Load a clean 4” Si wafer and run a 10-minute clean on the Si etcher using recipe “OPT-Chamber Clean-20 Deg” with processing parameters consisting of 20

mTorr chamber pressure, 2500 W ICP power, 50 sccm O_2, and a lower electrode temperature of -20 °C.

52. Wait while the lower electrode cools to temperature (-20 °C).
    a. The amount of time it takes to cool to temperature varies with the initial tool temperature, but it typically cools at a rate of ~1 °C/minute.
53. Load a clean 4” Si wafer and run a 10-minute SiO_2 etch season on the Si etcher using recipe “OPT-SiO2 Etch” with processing parameters consisting of 1 mTorr chamber pressure, 2000 W ICP power, 10 sccm of C4F8, and a lower electrode temperature of -20 °C.
54. Attach a Ti sample onto a clean 4” Si wafer using Santovac 5P-Ultra pump oil.
    a. Micromasking and feature definition limit this number.
55. Load the carrier-mounted Ti sample and run a ~30-minute SiO_2 etch using the aforementioned recipe and parameters.
56. Visually inspect the surface of the Ti sample by eye or with optical microscopy to make sure that the SiO_2 floor of the sample(s) was etched through.
    a. Etch for additional time as necessary.
57. Load a clean 4” Si wafer and run a clean process using the recipe “OPT-Chamber Clean” with processing parameters consisting of 20 mTorr chamber pressure, 2500 ICP power, 50 sccm O_2, and a lower electrode temperature of 20 °C.
    a. The duration of the clean process should equal the time spent running the etching process(es), including the seasoning process.
58. Close the valve on the liquid nitrogen tank.

59. Use the handle of a swab to remove the Ti sample from the 4” Si carrier wafer.
60. Use a swab and solvents to remove any solvents that are on the backside of the Si chips, then place them into a covered sample holder and return to the cleanroom in Bourns Hall B.
61. Sonicate the Ti sample(s) for 3 minutes in acetone and gently use a swab to remove any residual resist.
    a. Ensure there is enough solvents to prevent evaporation and do not let the sample surface dry out at any point.
    b. Do not press too hard while swabbing or you may damage the features.
62. Sonicate the Ti sample(s) for 3 minutes in isopropyl alcohol.
63. Thoroughly rinse the Ti sample(s) in deionized water to remove any remaining solvents, then place the sample(s) onto a non-shedding wipe and blow dry with nitrogen.
64. Bake the Ti sample(s) on a hotplate at 110-135 °C for 5 minutes, place them in a covered sample holder, and return to the cleanroom in the Materials Science and Engineering Building.
65. Load a clean 6” Si wafer into the metal etcher tool (Oxford Plasmalab 100).
66. Run a 10-minute pre-clean process using recipe “Plasma Clean @20 Deg C” with processing parameters consisting of 20 mTorr chamber pressure, 2500 W ICP power, 100 sccm of O_2 and a lower electrode temperature of 20 °C.
67. Run a 10-minute Ti etch season using recipe “BWoo Ti deep etch.”

   a. Adjust the oxygen flowrates depending on what type of Ti sample is being etched (i.e. HPT-processed or unprocessed)

68. Attach a Ti sample onto a clean 6” Si wafer using Santovac 5P-Ultra pump oil.
   a. Micromasking and feature definition limit this number.
69. Load the carrier-mounted Ti sample and run a ~20-minute Ti etch using the aforementioned recipe, “BWoo Ti deep etch,” and adjusted parameters.
   a. This etch step should completely through etch the Ti substrate, leaving the microneedle devices.
70. Load a clean 6” Si wafer and run a clean process using the recipe “Plasma Clean @ 20 Deg C” with processing parameters consisting of 20 mTorr chamber pressure, 2500 ICP power, 100 W forward power, 100 sccm O_2, and a lower electrode temperature of 20 °C.
   a. The duration of the clean process should equal the time spent running the etching process(es), including the seasoning process.
71. Use the handle of a swab to remove the Ti sample from the 6” Si carrier wafer.
72. Use a swab and solvents to remove any solvents that are on the backside of the Si chips, then place them into a covered sample holder and return to the laboratory.

<u>Recovering microneedle devices</u>

73. Fill a beaker with acetone and another with deionized water.
74. Gently place a Ti sample into the acetone and let it sit while the acetone soaks into the tape, thus releasing the microneedle devices.

75. Use tweezers to carefully pick up and transfer the microneedles from the acetone beaker into the beaker with deionized water.
76. Thoroughly rinse each microneedle device with deionized water and then blow dry.
77. Microneedle Fabrication is complete.

Appendix E. Supplemental Data

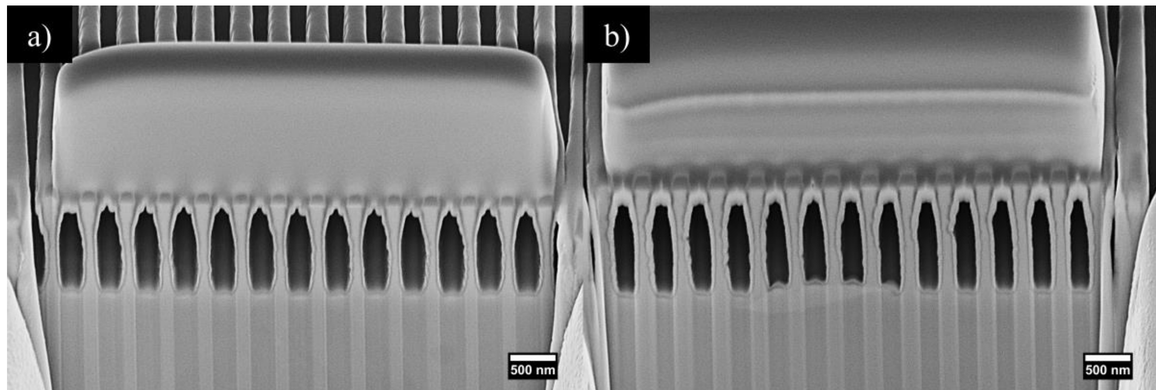

Figure E-1. SEM micrographs of 200 nm linewidth grating cross-sections depicting the effects of chamber pressure at a) 0.75; and b) 1.25 Pa.

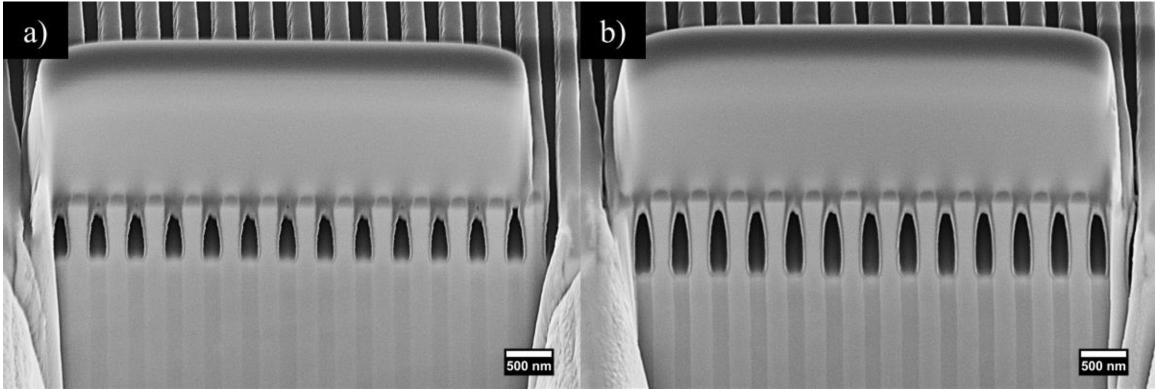

Figure E-2. SEM micrographs of 200 nm linewidth grating cross-sections depicting the effects of chlorine flowrate at a) 30; and b) 50 sccm.

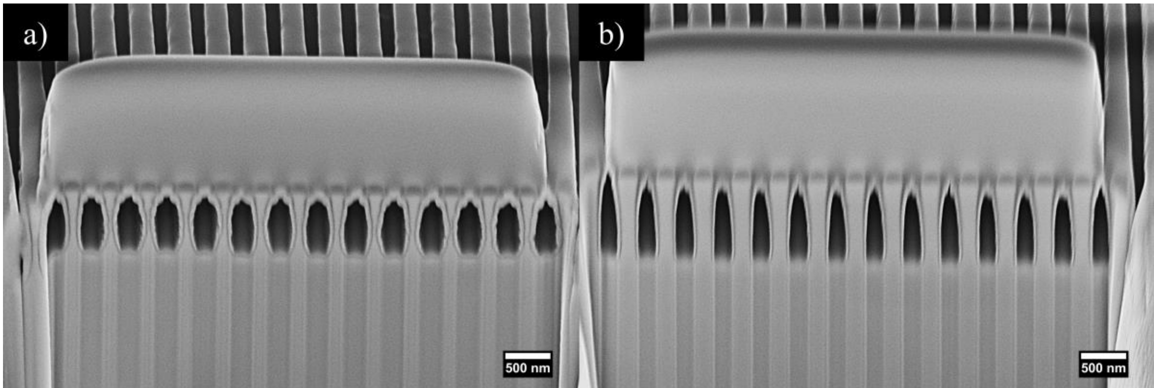

Figure E-3. SEM micrographs of 200 nm linewidth grating cross-sections depicting the effects of oxygen flowrate at a) 3; and b) 5 sccm.

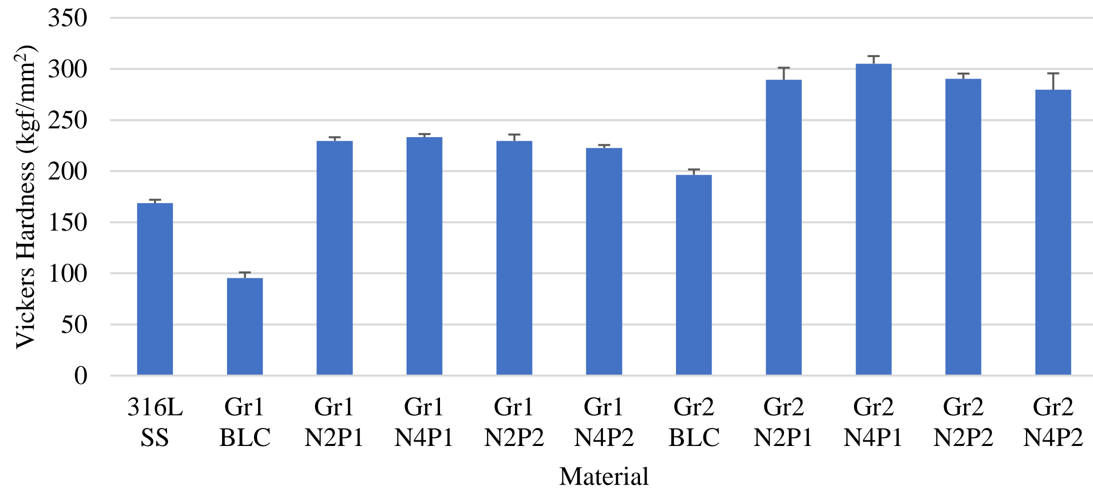

Figure E-4. Plot depicting the Vickers hardness values of all the studied materials. Values are averages of the indentations located at a distance of 4.5 mm from their respective centers. ($n \geq 3$).